Internal Report
DESY F35D-95-02
May 1995

Jet Production at HERA with the ZEUS Detector: Resolved and Direct Processes in Photoproduction and the Gluon Content of the Proton and the Photon

by

C. Glasman

Jet Production at HERA with the ZEUS Detector: Resolved and Direct Processes in Photoproduction and the Gluon Content of the Proton and the Photon

Thesis for the Degree of
Doctor of Philosophy

by

Claudia Glasman

Weizmann Institute of Science, Rehovot, Israel

April 1995

This work was carried out under the supervision of

Prof. U. Karshon and Dr. A. Montag

Weizmann Institute of Science, Rehovot, Israel.

Abstract

The HERA collider is the first electron-proton accelerator. During 1992 and 1993, it provided collisions between 26.7 GeV electrons and 820 GeV protons, with a centre-of-mass energy of 296 GeV. The ZEUS experiment collected about 600 nb^{-1} of integrated luminosity during these running periods.

Separation of hadrons and electrons is crucial for experiments at HERA. Identification of isolated electrons is relatively straightforward by taking advantage of the differences in the longitudinal development of electron and hadron showers in a calorimeter. However, electrons near or within hadronic jets pose a special problem. Electron-hadron separation becomes more involved as the energy of the particles decreases. Several techniques for electron identification with low hadron contamination have been developed by using the uranium-scintillator calorimeter and the hadron-electron separator of the ZEUS detector. The results obtained from the analysis performed on beam test data with beam energies between 3 and 9 GeV are presented.

The study of high-p_T jets provides a test of QCD. At HERA, the main source of jets comes from collisions between protons and quasi-real photons emitted by the electron beam. The photon contributes to the hard scattering cross section through the direct coupling (direct processes) and through the coupling of its partonic constituents (resolved processes) to the partons in the proton.

The large centre-of-mass energies available at HERA, allow for the first time the observation of jet production in quasi-real photoproduction processes. The analysis that led to this observation is presented. The main mechanisms responsible for jet production, resolved and direct, are identified. The characteristics of the inclusive jet sample are shown to be consistent with the dominance of resolved processes. A fraction of the events shows back-to-back two-jet production at the rate and with the features expected. A subsample of these events have energy in the electron direction consistent with that expected from the photon remnant in resolved photon processes. The method for isolating direct processes is explained and the results show a clear direct-photon signal in the dijet sample. After separating both contributions, dijet cross sections for the resolved and direct processes are given in a restricted kinematic range.

The two-jet cross section at small values of the fraction of the proton momentum carried by the interacting parton (x) is dominated by gluon initiated processes. An estimation of the gluon content of the proton ($xG(x)$) by using an isolated sample enriched in direct processes is presented. The $xG(x)$ obtained favours a more singular behaviour at small values of x than the extrapolations of QCD fits based on pre-HERA data.

Inclusive jet differential cross sections in quasi-real photoproduction interactions have been measured. These cross sections are given in the kinematic region $0.2 < y < 0.85$ and for jet pseudorapidities in the ep-laboratory range $-1 < \eta^{jet} < 2$. These measurements probe a new kinematic regime of the parton content of the photon at typical scales up to ~ 300 GeV^2. They are shown to be sensitive to the gluon content of the photon. Leading logarithm parton shower Monte Carlo calculations including resolved plus direct processes and using the predictions of current parametrizations of the photon parton distributions describe the shape and magnitude of the measured η^{jet} and E_T^{jet} distributions except for the very forward, low-E_T^{jet} region. These measurements are consistent with QCD in this new kinematic regime of the structure of the photon.

Esta tesis está dedicada a mi madre,
por su amor,comprensión y apoyo.

Acknowledgements

I am greatly indebted to my advisors, Prof. U. Karshon and Dr. A. Montag, for very precious guidance and advise during the time of this thesis. I am very grateful to Prof. U. Karshon for a careful reading of the manuscript.

I would like to express my gratitude to Prof. Y. Eisenberg for giving me the opportunity to join the ZEUS Collaboration and a long stay at DESY, where much of this work has been carried out, and to Prof. E. Duchovni and Y. Tserruya for useful comments.

Special thanks are due to T. Gilead, H. Katz and N. Stern for invaluable technical help.

I am very grateful to Prof. A. Levy and H. Abramowicz for their support and advise that kept me going through difficult moments.

I would like to thank Prof. G. Wolf and R. Klanner for helpful comments and suggestions.

I wish to thank Dr. J. Terrón for many useful discussions and a very fruitful collaboration during my stay at DESY.

I would also like to acknowledge the encouragement received from the coordinators of the ZEUS working groups in which I have participated, Prof. F. Barreiro, R. Nania, K. Tokushuku, and J. Whitmore. I have also profitted from discussions with G. D'Agostini and K. Desch.

Finally, I am grateful to the Weizmann Institute of Science for the financial support received during the completion of my thesis, and to the Deutscher Akademischer Austauschdienst during my stay at DESY.

Contents

Chapter 1

Hard scattering at low Q^2

1.1 Introduction

The study of high-p_T jets provides a test of perturbative Quantum Chromo Dynamics (QCD). At HERA, which provides collisions between electrons and protons, the main source of jets comes from collisions between protons and quasi-real photons emitted by the electron beam. The photon contributes to the hard scattering cross section with two terms: a direct coupling and through the coupling of its partonic constituents to the partons in the proton. The direct coupling allows the study of the gluon content of the proton, since at the small values of the fraction of the proton momentum carried by the interacting parton available at HERA energies, the two-jet cross section is dominated by gluon initiated processes. On the other hand, the coupling through the constituents of the photon is the main source of information on the poorly determined photon structure function. In particular, the inclusive jet cross sections are sensitive to the gluon content of the photon.

QCD-based models of quasi-real photoproduction processes, including parton distributions in the photon and proton compatible with experimental data, predict that the processes in which the photon has a hadron-like behaviour should dominate the inclusive jet cross section for a wide range of jet transverse energy [1, 2]. Evidence for hard photon scattering, in quantitative agreement with QCD calculations, has been observed in two-photon physics at e^+e^- colliders [3], as well as in fixed target experiments [4], but the restricted phase space available at the energies of these experiments has not allowed the observation of jet production. HERA energies provide a wider phase space which enables the observation of jet production in quasi-real photoproduction processes.

The H1 and ZEUS experiments at the electron-proton (ep) HERA accelerator started taking data in June 1992. During 1992 and 1993, electrons of 26.7 GeV collided against protons of 820 GeV, with a centre-of-mass energy of 296 GeV. This centre-of-mass energy is by one order of magnitude larger than in previous fixed target experiments and it allows to measure the proton structure function and to study the photoproduction regime in new kinematic domains. During the first year of HERA running, the ZEUS experiment collected about 30 nb^{-1} of integrated luminosity. From the analysis of these data, many results have been obtained in the field of deep inelastic scattering (DIS), photoproduction and new particle searches [5]-[15]. During 1993, the luminosity delivered by HERA has increased by a factor of 20. This allowed the ZEUS

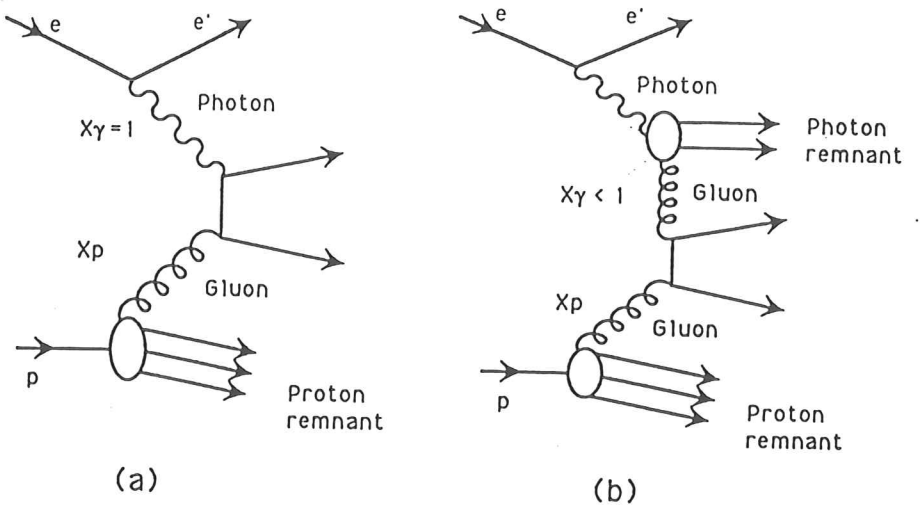

Figure 1.1: Schematic diagrams showing examples of (a) a direct process and (b) a resolved process.

experiment to collect about 0.5 pb^{-1} of integrated luminosity during this running period. New results have already been obtained [16]-[18].

This thesis is devoted to the study of high-p_T jet production in phoroproduction with the ZEUS detector. The main mechanisms for jet production at HERA are explained in the next section. Chapter 2 is devoted to the description of HERA and the ZEUS detector, whereas chapter 3 presents a study of electron identification obtained from beam test data. The analysis leading to the observation of jet production in γp interactions is presented in chapter 4 and the identification of the mechanisms responsible for high-p_T jet production is provided in chapter 5. The results obtained from the analysis performed to estimate the gluon content of the proton via two-jet production are presented in chapter 6. Chapter 7 is devoted to the measurement of inclusive jet differential cross sections and comparison to leading order (LO) QCD calculations. Finally, chapter 8 gives the summary and conclusions.

1.2 Hard scattering: the resolved and direct processes

In the Standard Model, ep scattering is mediated by the exchange of a gauge boson (γ, Z^0, $W^{\pm}$) which interacts with the constituents of the proton. For very low four momentum transfers, the reaction is dominated by the exchange of almost real photons. The ep cross section mediated by photon exchange can be expressed in terms of the virtual $\gamma^* p$ cross sections as

$$\frac{d^2\sigma_{ep}(s)}{dydQ^2} = A\sigma^T_{\gamma^* p}(W^2, Q^2) + B\sigma^L_{\gamma^* p}(W^2, Q^2)$$

where $\sigma^T_{\gamma^* p}(\sigma^L_{\gamma^* p})$ is the cross section for transversely (longitudinally) polarized photons, Q^2 is the virtuality of the photon, W measures the centre-of-mass energy of the γp interaction[1],

[1]This expression for W holds when the mass of the proton and electron are neglected.

Process	$\sum \lvert M \rvert^2$	$\sigma(p_{Tmin} = 5)$ **nb**	$\sigma(p_{Tmin} = 8)$ **nb**
		LAC1/GRV-HO	
$qq' \to qq'$	$\frac{4}{9}\frac{s^2+u^2}{t^2}$	29./25.	4.6/4.4
$qq \to qq$	$\frac{4}{9}(\frac{s^2+u^2}{t^2} + \frac{s^2+t^2}{u^2}) - \frac{8}{27}\frac{s^2}{ut}$		
$q\bar{q} \to q'\bar{q}'$	$\frac{4}{9}\frac{t^2+u^2}{s^2}$	0.54/0.52	0.13/0.11
$q\bar{q} \to q\bar{q}$	$\frac{4}{9}(\frac{s^2+u^2}{t^2} + \frac{t^2+u^2}{s^2}) - \frac{8}{27}\frac{u^2}{st}$		
$q\bar{q} \to gg$	$\frac{32}{27}\frac{t^2+u^2}{tu} - \frac{8}{3}\frac{t^2+u^2}{s^2}$	0.53/0.51	0.10/0.10
$gg \to q\bar{q}$	$\frac{1}{6}\frac{t^2+u^2}{tu} - \frac{3}{8}\frac{t^2+u^2}{s^2}$	4.4/1.8	0.32/0.20
$gq \to gq$	$-\frac{4}{9}\frac{s^2+u^2}{su} + \frac{u^2+s^2}{t^2}$	128./78.	14./11.
$gg \to gg$	$\frac{9}{2}(3 - \frac{tu}{s^2} - \frac{su}{t^2} - \frac{st}{u^2})$	104./46.	6.8/4.9
$\gamma g \to q\bar{q}$	$\frac{t^2+u^2}{tu}$	11.	2.5
$\gamma q \to gq$	$-\frac{8}{3}\frac{s^2+u^2}{su}$	26.	4.9

Table 1.1: Lowest order invariant matrix elements squared and total cross section (last two rows) for $p_{Tmin} = 5$ GeV/c and $p_{Tmin} = 8$ GeV/c for two choices of parton densities in the photon (LAC1 and GRV-HO) and MRSD− for the parton densities in the proton for resolved and direct processes.

$W^2 = ys - Q^2$ ($\sim ys$ for $Q^2 \ll 1$ GeV^2), y is the fraction of energy transfer in the proton rest frame, and A and B are known functions of y and Q^2. A simple and convenient method to calculate the ep cross section is the Weizsäcker-Williams approximation (WWA). In this method, the σ_{ep} is approximated by the product of the equivalent number of photons in the electron times the real γp cross section,

$$\left.\frac{d^2\sigma_{ep}(s)}{dydQ^2}\right|_{WWA} = \frac{\alpha}{2\pi}\frac{1}{Q^2}\frac{1+(1-y)^2}{y}\sigma^{tot}_{\gamma p}(W^2)$$

where α is the electromagnetic coupling constant. The WWA has been estimated to be good to $\sim 10\%$ at HERA energies [19].

Most of the photoproduction cross section is due to soft processes. However, at the large centre-of-mass energies available at HERA, a fraction of the γp interactions is expected to contain high-p_T processes. In LO QCD, these hard processes are of two main types [1, 20]. In the *direct* processes, the photon participates as a point-like particle, interacting with a parton from the proton. In the *resolved* processes, the photon behaves as a source of partons which can scatter off those in the proton. Therefore, one-photon exchange hard scattering cross sections at HERA contain in general two contributions, the direct contribution and the resolved photon one.

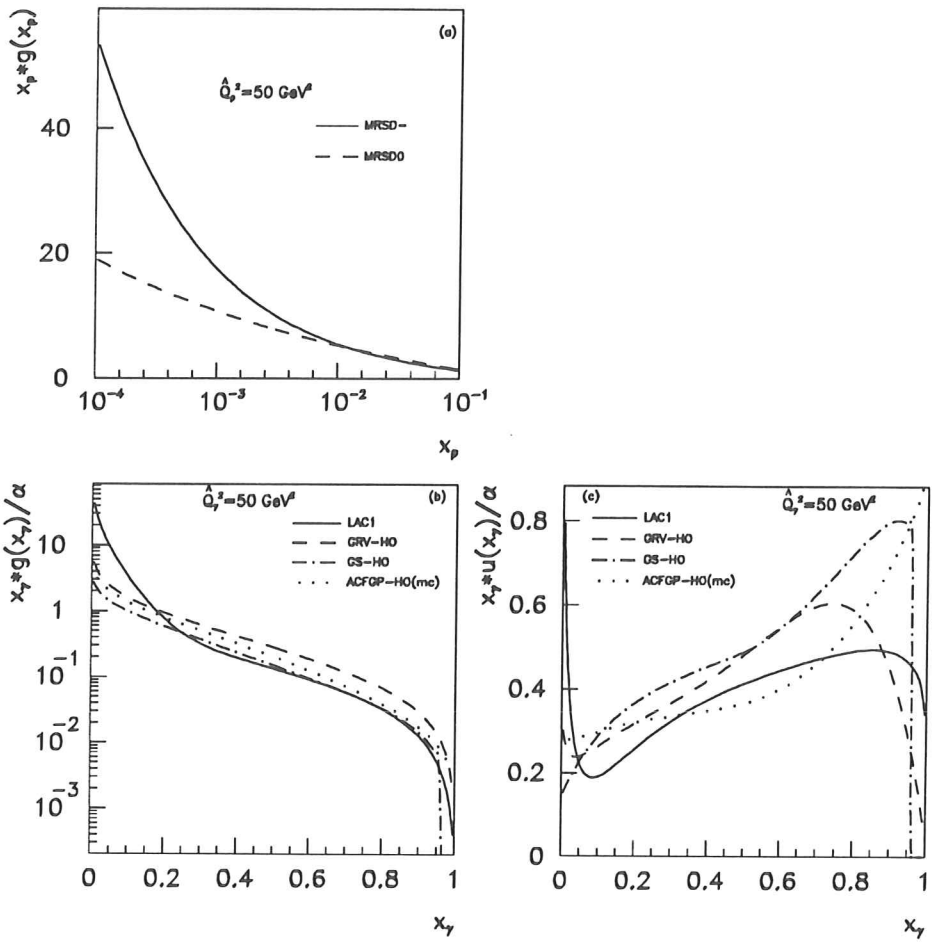

Figure 1.2: (a) Gluon distribution for different parametrizations of the proton structure function; (b) gluon and (c) up-quark distributions for various parametrizations of the photon structure function.

Both type of processes produce two or more partons in the final state giving rise to multi-jet structures with features similar to those observed in hadron-hadron collisions [21]. The general expression for the electroproduction cross section for two high-p_T jets at low Q^2 ($Q^2 \ll 1$ GeV^2) in the WWA is [1]

$$\frac{d\sigma(ep \to jet + jet + X)}{d\hat{p}_T^2} = \int dy\ f_{\gamma/e}(y) \int\int dx_p\ dx_\gamma\ f_p(x_p)\ f_\gamma(x_\gamma)\ \frac{d\hat{\sigma}}{d\hat{p}_T^2} \qquad (1.1)$$

where the function $f_p(f_\gamma)$ is the parton density inside the proton (photon), with $f_\gamma(x_\gamma) = \delta(1 - x_\gamma)$ for the direct contributions, $\hat{\sigma}$ is the parton-parton scattering cross section, x_p (x_γ) is the fraction of the proton (photon) momentum carried by the interacting parton, the function $f_{\gamma/e}$ describes the photon flux that originates from the electron beam, and $\hat{p}_T$ is the parton transverse momentum in the hard parton-parton scattering process.

The direct contribution is described by two subprocesses in which the initial parton in the proton is either a gluon ($\gamma g \to q\bar{q}$, Boson Gluon Fusion $\equiv$ BGF) [22] or a quark ($\gamma q \to gq$, QCD Compton scattering $\equiv$ QCDC) [23]. For resolved processes, many combinations are possible

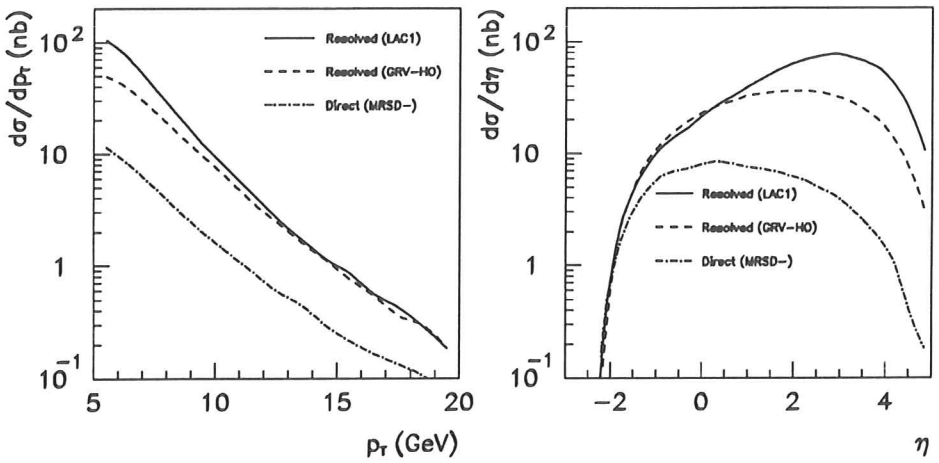

Figure 1.3: $d\sigma/dp_T$ and $d\sigma/d\eta$ LO QCD calculations for resolved processes, using LAC1 (solid line) and GRV-HO (dash line) for the photon parton distributions, and for direct processes (dash-dotted line). In both cases, the MRSD− set was used for the proton parton parametrizations.

since the initial parton in the proton or the photon can be a quark or a gluon [1] (see figure 1.1). For all these processes, the final state consists of two partons, carrying large transverse momenta and balancing each other, with the proton remnant and the scattered electron both carrying little transverse momenta. In resolved processes, a hadronic system from the fragmentation of the spectator parton(s) in the photon is also expected.

The matrix elements squared for each subprocess [24] are shown in table 1.1, where s, t and u are the Mandelstam variables. The dominant subprocesses are those which contain a $1/t^2$ or $1/u^2$ term in the LO order matrix element squared. This is a consequence of the presence of Feynman diagrams which proceed by gluon exchange in the t- or u-channel. Characteristic behaviour for such channels with spin-1 particle (the gluon of QCD) exchange is the rapid rise of the cross section with increasing $\cos\theta^*$, where θ^* is the scattering polar angle in the centre-of-mass system of the two colliding partons. Next in dominance are those terms with a $1/ts$, $1/us$ or $1/tu$ singularity, which proceed by spin-1/2 particle (quark or antiquark) exchange. Finally, the subprocesses with a $1/s^2$ term are suppressed with respect to the ones mentioned above.

Therefore, the dominant processes should be $qq' \to qq'$, $qq \to qq$, $q\bar{q} \to q\bar{q}$, $gq \to gq$ and $gg \to gg$. However, to obtain the cross section, the matrix elements must be convoluted with the partonic density in the proton and in the photon (eq. 1.1) and this changes the hierarchy of processes. This hierarchy is also p_T-dependent. The transverse momentum of each massless parton in the final state is given by $p_T^2 = \frac{1}{4}\hat{s}(1-\cos^2\theta^*)$, where $\hat{s} = x_\gamma x_p y s$ is the centre-of-mass energy of the parton-parton system. For low p_T, the low x region of the parton densities is probed, in which case the gluon density in the proton and in the photon dominates; hence those processes which contain a gluon in the initial state have the highest contribution to the cross section. As p_T increases, higher values of x are probed and the quark initiated processes become more significant. This can be seen in the last two columns of table 1.1, where the expected LO

QCD cross section for each subprocess calculated using the PYTHIA Monte Carlo is shown for two different p_{Tmin} values and for two different parametrizations of the parton densities in the photon (LAC1 [25] and GRV-HO [26]) and the MRSD− [27] set for the parton parametrizations in the proton. As can be seen in this table, the most important processes at $p_{Tmin} = 5$ GeV/c are $gq \rightarrow gq$ and $gg \rightarrow gg$. At $p_{Tmin} = 8$ GeV/c, the processes $qq' \rightarrow qq'$, $\gamma g \rightarrow q\bar{q}$ and $\gamma q \rightarrow gq$ become of the same order as the processes mentioned previously.

The cross sections for jet production are large enough to be observable and the different features of jet production for both type of processes, resolved and direct, should enable their identification. Moreover, the direct processes depend only on the proton parton distributions. Therefore, this type of processes allow to probe the gluon content of the proton due to the dominance of the BGF process at low x_p values. Measurements of jet production for direct processes allow to discern among current parametrizations. Figure 1.2a shows the gluon distribution evaluated at a typical scale of $\hat{Q}_p^2 = 50$ GeV^2 for two parametrizations (MRSD− and MRSD0 [27]), which are extrapolations of QCD fits based on pre-HERA data. At low x_p values, the MRSD0 set contains a flat gluon distribution, $x_p \cdot g(x_p)$ ~constant, whereas MRSD− has a singular gluon content, $x_p \cdot g(x_p) \sim x_p^{-1/2}$.

Differential jet cross sections as a function of transverse energy ($d\sigma/dE_T^{jet}$) and pseudorapidity[2] ($d\sigma/d\eta^{jet}$) are sensitive to the partonic content of the proton and the photon [1, 2]. The dependence on the parton content of the photon can be isolated by studying jet production at sufficiently high E_T^{jet}, which corresponds to a kinematic region where the proton structure function is well measured. The hadronic structure of the photon has been experimentally investigated mainly in inclusive $e\gamma$ scattering [28]. Leading order (LAC1 [25] and DG [29]) and next-to-leading order (NLO) (GRV-HO [26], GS-HO [30] and ACFGP-HO(mc) [31]) fits to these data allowed the extraction of the quark densities in the photon, leaving the gluon density essentially unconstrained. The gluon and quark distributions in these parametrizations of the partonic content of the photon are shown in figures 1.2b and 1.2c. As an example, the gluon distribution ($x_\gamma \cdot g(x_\gamma)$) and the up-quark distribution ($x_\gamma \cdot u(x_\gamma)$) have been evaluated at a typical scale $\hat{Q}_\gamma^2 = 50$ GeV^2. As is commonly represented in the literature, the photon parton distributions have been divided by α. The main difference between the various parametrizations is in the gluon content at low values of x_γ, $x_\gamma < 0.1$.

Leading logarithm QCD calculations, using the predictions of LAC1 or GRV-HO for the parametrizations of the photon parton distributions and MRSD− for the proton parton distributions, are shown in figure 1.3, for resolved and direct processes, with $p_{Tmin} = 5$ GeV/c. LO QCD predicts a very different behaviour of the p_T and η distributions for resolved and direct processes. The resolved processes dominate over the direct for a wide range of p_T, but the direct processes finally dominate the distribution at large p_T values. A different behaviour is expected as well in the pseudorapidity distribution for the two contributions since for resolved processes the two parton center-of-mass system is boosted in the proton direction. The different gluon content of the photon parametrizations by LAC1 and GRV-HO (see figure 1.2b), can be seen in figure 1.3 in the forward region. For direct processes the boost is smaller and hence, the partons are distributed in the central region. The measurement of the differential jet cross sections should test the predictions of the current parametrizations at higher $\hat{Q}_\gamma^2$ scales in the photon ($\hat{Q}_\gamma \sim E_T^{jet}$) and give information concerning its gluon density.

[2] $\eta = -\ln(\tan\frac{\theta}{2})$

Chapter 2

HERA and the ZEUS experiment

2.1 The HERA machine

The Hadron Electron Ring Accelerator (HERA) [32] is an electron-proton collider built at the DESY site (Hamburg - Germany). The tunnel has a circumference of about 6.3 km and is situated 10 - 25 m underground. It contains two separate rings, one that stores and accelerates protons and the other electrons. The proton ring lies above the electron one, except at the interaction points. The main HERA parameters are summarized in table 2.1 (design parameters and, in parentheses - if different, the values for the Fall '92 run). The layout of the HERA accelerator is shown in figure 2.1.

During the 1992 data taking period, bunches of electrons with energy $E_e = 26.7$ GeV and bunches of protons of energy $E_p = 820$ GeV were colliding at HERA. The accelerator is designed to run with 220 bunches in each of the electron and proton rings, with a time between bunch crossings of 96 ns. For the data taking periods of 1992 only ten consecutive bunches (0-9) were filled for each beam. In addition, electron bunch number 19 was filled for measuring electron induced background, and the electron bunch number 9 (BCN = 9) was left empty, in order to study proton beam backgrounds. These umpaired bunches pass through the detector without encountering any other bunch in the opposite direction and hence, they are useful to estimate backgrounds coming from interactions of the beam with the gas inside the beam pipe (beam gas) or with the elements of the accelerator. The electron and proton beam currents were typically 1-3 mA and the length of the interaction region, determined by the proton bunch length, was about 25 cm for the Fall '92 running period.

During the 1993 runs of HERA, 84 bunches were filled with electrons and protons. In addition, 10 electron and 6 proton bunches were left unpaired to study beam induced backgrounds. The currents were typically 10 mA for the electron and proton beams. The length of the interaction region, determined by the proton bunch length, was about 11 cm.

2.2 The ZEUS detector

Construction of a good detector for HERA is a challenge since particles and jets with energies up to $\sim$ 800 GeV have to be measured with high precision. The most important component of such a detector is a high resolution calorimeter. The large momentum imbalance between incident protons and electrons sends most particles into a narrow cone around the proton direction. Thus the calorimeter has to achieve simultaneously high hermiticity, good energy resolution and fine segmentation. The detector has also to cope with high particle densities and with a

HERA Parameters	electron	proton
Nominal Energy (GeV)	30 (26.7)	820
Luminosity ($cm^{-2}s^{-1}$)	1.5 10^{31} (0.2-1.6 10^{29})	
Circumference (m)	6336	
Magnetic Field (T)	0.165	4.65
Energy Range (GeV)	10-33	300-820
Injection Energy (GeV)	14	40
Circulating Current (mA)	58 (0.5-3)	163 (0.5-3)
Number of Colliding Bunches	220 (9)	
Time Between Crossings (ns)	96	
Horizontal Beam Size σ_x (mm)	0.26 (0.3)	0.29 (0.4)
Vertical Beam Size σ_y (mm)	0.07 (0.07)	0.07 (0.1)
Longitudinal Beam Size σ_z (cm)	0.8	11 (25-55)
z-Vertex width, $\sigma_{z-Vertex}$ (cm)	6 (12-28)	
Filling Time (hours)	0.25 ($\sim$ 1)	0.3 ($\sim$ 5)

Table 2.1: HERA parameters

time interval between bunch crossings of only 96 ns.

A complete description of the detector can be found in ref. [33]. A general view of the detector is presented in figure 2.2. The essential elements of the detector are:

(The following elements are situated within a thin magnetic solenoid (COIL))

– Vertex Detector (VXD)

– Central Tracking Detector (CTD)

– Transition Radiation Detector (TRD)

– Planar Chambers (FDET, RTD) (partially inside the COIL)

(The following elements are outside the COIL)

– Electromagnetic and Hadron Calorimeter (CAL) surrounding the COIL over the full solid angle

– Backing Calorimeter (BAC)

– Muon Detector (MUON)

– Leading Proton Spectrometer (LPS)

– Luminosity Monitor (LUMI)

– Vetowall

– C5 counter

The detector is structurally subdivided into the inner components supported by the bottom yoke, and the clam shells carrying most of the backing calorimeter and the muon detectors. The clam shells can be retracted sideways by as much as 4.9 m. In this way, fast and simple access is provided to all components of the detector. In addition, planar arrays of silicon diodes are imbedded within the CAL to improve electron identification. This subcomponent is the Hadron-Electron Separator (HES).

In this thesis, only the components used in the analysis that follows are described in some detail. These are the high resolution uranium-scintillator calorimeter, the central tracking detector and the luminosity monitor. The vetowall and C5 counter were used for rejecting beam induced backgrounds. The HES has been used to study the identification of low energy electrons.

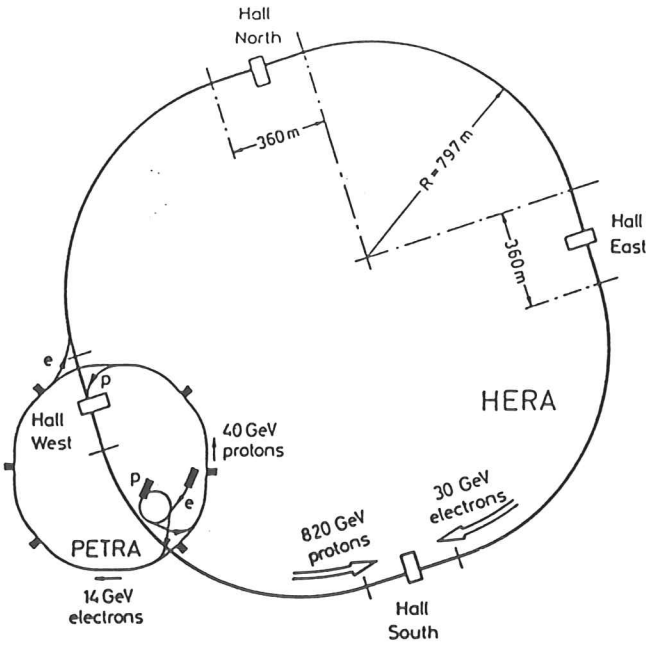

Figure 2.1: Layout of HERA.

2.2.1 The uranium calorimeter

The uranium calorimeter (CAL) (see figure 2.3) covers the polar angle range between $2.6° < \theta < 176.1°$, where in the standard ZEUS right-handed coordinate system, $x = y = z = 0$ is the nominal ZEUS interaction point (IP), the positive z-axis points in the direction of flight of the beam of protons and y points upwards. It is constructed with alternating layers of depleted uranium and scintillator with one sampling every radiation length. The relative thicknesses of uranium and scintillator in the layer were chosen to give equal calorimeter response to electrons (or photons) and hadrons. Scintillator tiles form towers in depth that are read out on two sides through wavelength shifter bars, light guides and photomultipliers (PMTs). The CAL consists of three parts: rear calorimeter (RCAL) covering the backward pseudorapidity[1] range ($-3.4 < \eta < -0.75$), barrel calorimeter (BCAL) covering the central region ($-0.75 < \eta < 1.1$) and forward calorimeter (FCAL) covering the forward region ($1.1 < \eta < 3.8$). The CAL is segmented in depth into electromagnetic (EMC) and hadronic (HAC) sections. The EMC sections are divided into cells of transverse dimensions 5×20 cm^2 (10×20 cm^2 in RCAL) and the HAC sections consist of transverse dimension 20×20 cm^2. Figure 2.4 shows a diagram of an FCAL module. The energy resolution as measured under test beam conditions is $\sigma_E/E = 0.18/\sqrt{E} \oplus 1\%$ (E in GeV) for electrons and $\sigma_E/E = 0.35/\sqrt{E} \oplus 1\%$ for hadrons [34]. The timing resolution of the CAL cells, $\sigma(t) = 1.5/\sqrt{E} \oplus 0.5$ ns [34, 35], allows rejection of out of time beam gas interactions. In the analysis presented here, CAL cells with EMC (HAC) energy below 60 (110) MeV were excluded to minimize the effect of calorimeter noise. This noise is dominated by uranium activity due to the high quality of the readout system, and has an r.m.s. value below 19 (30) MeV for EMC (HAC) cells. The uranium activity also allows a periodic calibration of the CAL to within 1%.

[1] $\eta = -\ln\tan(\frac{\theta}{2})$

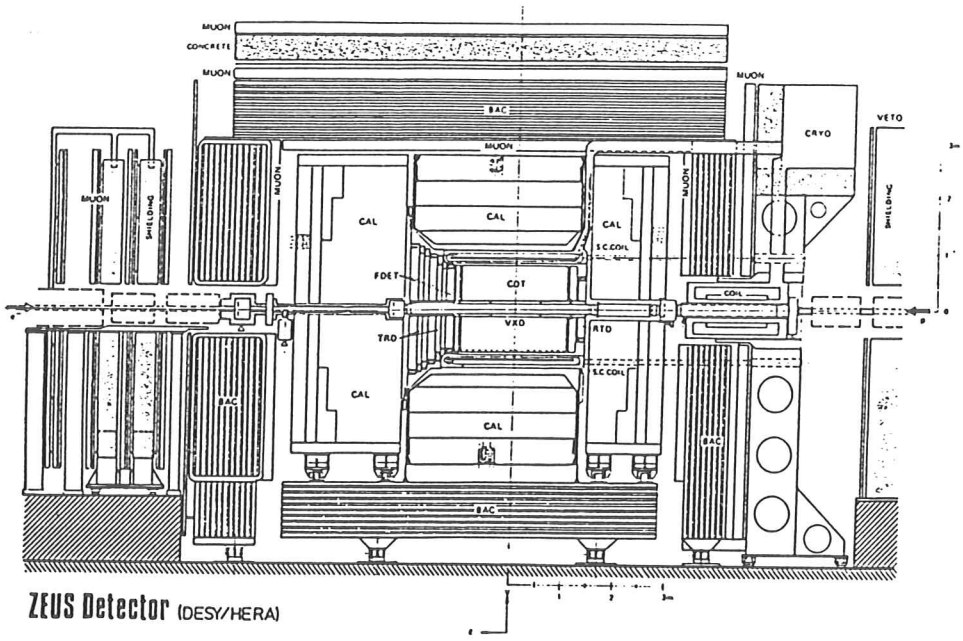

Figure 2.2: Schematic view of the ZEUS detector.

2.2.2 The central tracking detector

The central tracking detector (CTD) [36] measures charged particle trajectories. It consists of a jet-type drift-chamber which surrounds the beam pipe and is operated in a magnetic field of 1.43 T, provided by a thin superconducting coil. The chamber consists of 72 cylindrical drift-chamber layers, organized into 9 'superlayers'. The wires in the even-numbered superlayers have small stereo angles to allow a three dimensional reconstruction of tracks. In the other, axial, superlayers the wires are parallel to the z axis. For the '92 data taking periods, only the inner three axial superlayers were instrumented using a z-by-timing readout with single wire resolutions of $\sigma_z = 4$ cm and $\sigma_{r\phi} = 1$ mm. The tracking information was used to reconstruct the vertex position along the z direction. During the 1993 data taking period, the CTD was fully instrumented. Figure 2.5 shows a schematic diagram of the CTD.

2.2.3 The luminosity monitor and the luminosity measurement

To measure the luminosity as well as to tag the scattered electron from very small Q^2 processes, two lead-scintillator electromagnetic calorimeters are installed in the HERA tunnel [37] (see figure 2.6). The luminosity is determined by a measurement of the rate of hard bremsstrahlung photons produced in the Bethe-Heitler process $ep \rightarrow ep\gamma$. The experimental signature of this process is a coincidence of a photon and an electron at small angles to the electron beam direction, with energies adding up to the beam energy: $E_{e'} + E_\gamma = E_e$ (see figure 2.7) [5]. Photons emerging from the electron-proton IP at angles $\theta_\gamma \leq 0.5$ mrad with respect to the electron beam axis hit the photon calorimeter at 107 m from the IP. The background rate from electron beam bremsstrahlung on the residual gas in the beam pipe was substracted using the unpaired electron bunch. The final integrated luminosity was determined from the corrected photon rate, the detector acceptance and the known Bethe-Heitler cross section.

Electrons emitted from the IP at scattering angles $\theta'_e \leq 6$ mrad and with energies $0.2E_e <$

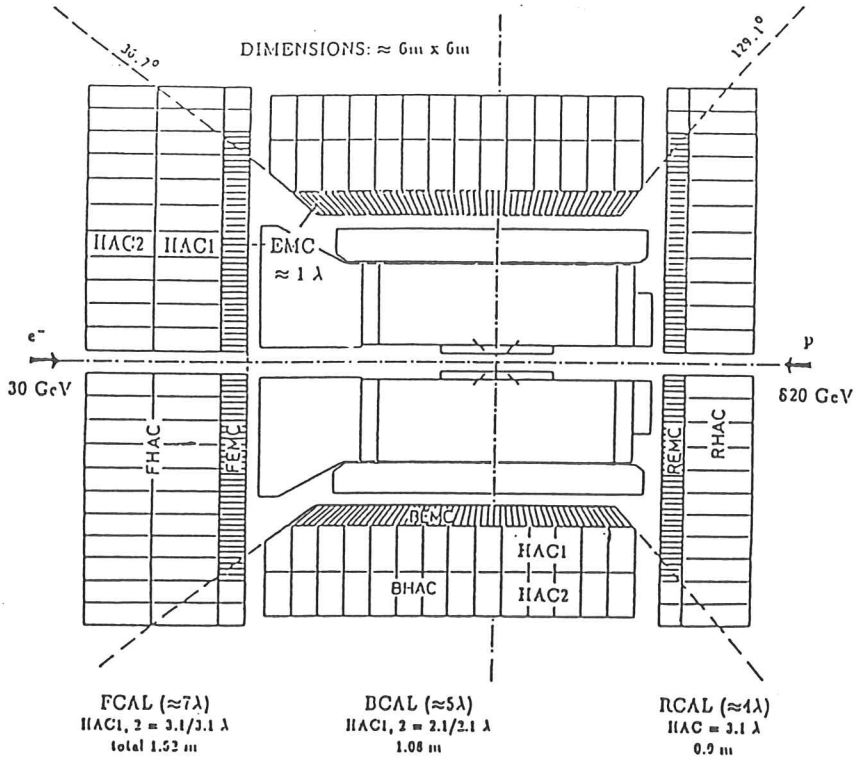

Figure 2.3: The uranium scintillator calorimeter.

$E'_e < 0.9E_e$ are deflected by beam magnets and hit the electron calorimeter placed 34.7 m from the IP. For photoproduction, the electron calorimeter tags events in the Q^2 range from 4 10^{-8} to 2 10^{-2} GeV^2. These events will be referred to as 'tagged events' throughout this thesis.

2.2.4 The C5 counter and the vetowall

In order to discriminate against the very high interaction rate produced upstream of the detector by interactions of the beam protons with residual gas in the vacuum pipe (beam gas), two small lead-scintillator sandwich counters (C5) partially surround the beam pipe just upstream of the RCAL ($z = -315$ cm). These counters are also used to measure the timing and longitudinal spread of both the proton and electron bunches at HERA. In addition, two layers of scintillator counters are installed at $z = -727$ cm on either side of an 87 cm thick iron wall (vetowall) to signal background particles.

2.2.5 The hadron electron separator

The main purpose of the HES is the identification of electrons near to or overlapping hadron jets. The HES is composed of planar arrays of silicon pad diodes mounted within the CAL. The silicon diodes size was chosen to be 3×3 cm^2. This assures that the HES can handle the particle density, and the buffered readout will take care of the high bunch crossing rate. The HES also has the potential to improve the spatial resolution of the EMC.

The complete HES will comprise two planes of diodes in the FCAL, behind the third and sixth uranium plates, respectively; one plane in the barrel after the fourth plate; and one plane in the rear behind the third plate. At these depths, where each layer corresponds approximately to a radiation length, an incident electron will have showered producing a large number of e^+e^- pairs and consequently a large signal in the depleted diode, while the typical hadron will simply leave a minimum ionization trail in the 400 μm thick pad.

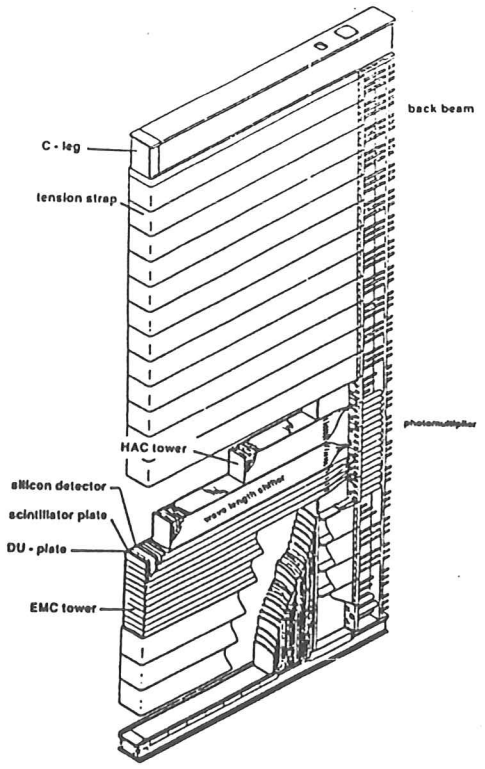

Figure 2.4: FCAL module.

In order to operate a silicon diode as a detector, a reverse bias voltage is applied so that the depletion region is maximal. When a particle crosses a diode, it creates electron-hole pairs in the depletion region. These charges drift in the space-charge electric field of the depletion region toward the electrodes. The generated charge is collected and amplified. A minimum ionizing particle traversing the silicon produces approximately 7500 electron-hole pairs per 100 μm.

The diode mechanical unit consists of two diodes with two preamplifiers mounted upon a ceramic card. They are mounted on long boards or "skis". The remainder of the analog readout electronics is located in the top frame of the CAL. The signal from each diode goes to the first element of the analog card, which has 48 channels, followed by 12 pipelines which store information from sequential beam crossings. The card contains, in addition, multiplexor buffers, control logic, and cable drivers.

The total number of pads required is 50,000 which will cover a total area of approximately 50 m^2. The HES is being implemented in stages. In the first stage of the experiment, only the Rear Hadron Electron Separator (RHES) covering the RCAL, consisting of 10,000 channels, has been implemented (2,000 channels were ready as a pilot project for the '92 runs of HERA and the rest was implemented for the '93 runs).

2.3 The trigger and data acquisition system

The ZEUS trigger is organized in three levels [33]. Its design was determined in order to deal with the short (96 ns) intervals between bunch crossings and the high rate of background. The first level trigger (FLT) selects events according to either energies measured in the central calorimeter or in coincidence with energy detected in the electron calorimeter of the luminosity monitor, and veto signals from the C5 counter. At the second (SLT) and third (TLT) level triggers, rejection of beam gas and non-beam related backgrounds is performed.

The FLT uses cells grouped into trigger towers (each tower is approximately 20 cm $\times$ 40 cm

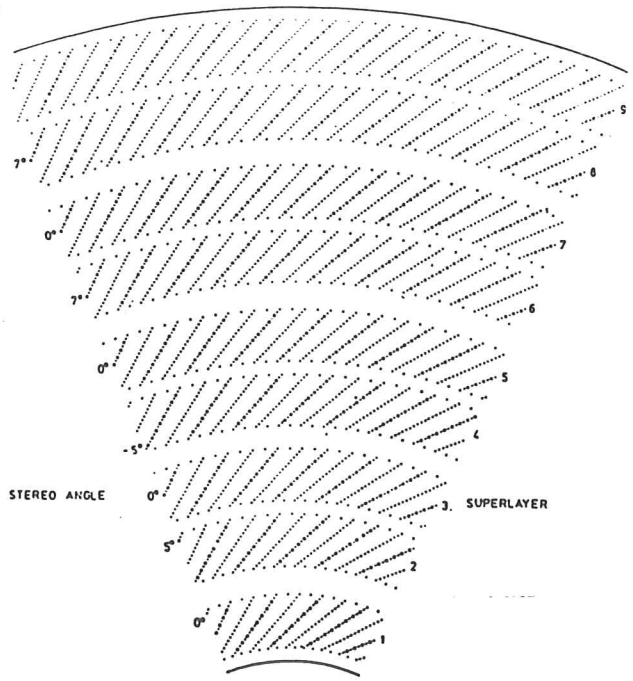

Figure 2.5: The central tracking chamber.

in cross-section). For the Fall '92 runs, a FLT was issued if the energy deposited in a trigger tower in any EMC section or in the HAC section of the FCAL exceeded a certain threshold. For the EMC, this threshold was set to 50 GeV for the innermost ring of trigger towers around the beam pipe, 20 GeV for the second ring, and 10 GeV elsewhere. For the FCAL HAC, the thresholds were 70, 25 and 10 GeV, respectively. For the RCAL EMC, the setting was 10 GeV for the innermost ring and 1 GeV elsewhere. The BCAL EMC threshold was 2.5 GeV for an integrated luminosity of $\sim$ 17 nb^{-1} and then lowered to 1 GeV, corresponding to an integrated luminosity of about 8.5 nb^{-1}.

The SLT and TLT levels were used for removing triggered events in which an electrical discharge in only a single PMT caused the trigger conditions to be satisfied. At these trigger levels cosmic ray contamination was also rejected.

A major source of background comes from the interactions of the beams with the residual gas (beam gas), the proton beam gas having a higher rate than the electron gas. This background can be subtantially reduced by using the timing information given by the CAL. Calorimeter signal times, t_{FCAL} and t_{RCAL}, were defined for groups of FCAL and RCAL cells with deposited energy above 1 GeV. The time offsets were adjusted so that t_{FCAL} and t_{RCAL} were approximately zero when particles emitted from the IP reach the CAL. Hence, particles generated upstream of the detector will reach the RCAL $\sim$ 12 ns earlier than those emitted from the IP. Figure 2.8 shows a plot of $t_{FCAL} - t_{RCAL}$ vs. t_{RCAL}, demonstrating a clear separation between the background events and the physics candidates. Events were rejected in the TLT if at least two photomultipier channels in FCAL (RCAL) each registered more than 1 GeV and if the signal times were consistent with an interaction upstream of RCAL, i.e. $t_{FCAL} \sim 0$ ns and $t_{RCAL} \sim -12$ ns.

During the Fall '92 runs, about four million events were collected by the trigger described above.

During the 1993 data taking period, the three-level trigger was largely modified with respect to the previous year in order to cope with the increase in luminosity. The FLT for the sample

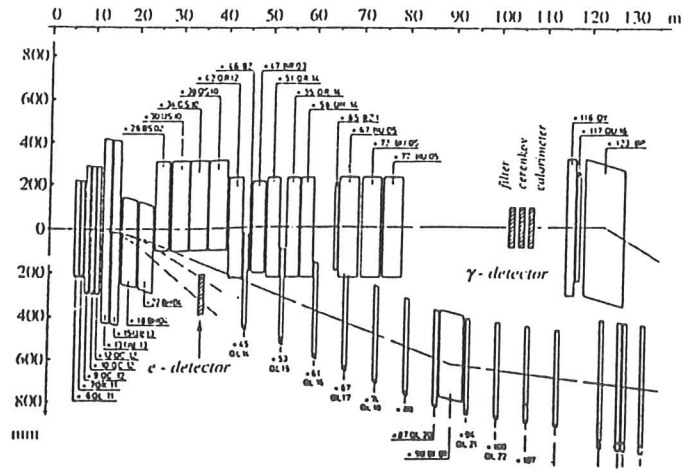

Figure 2.6: The luminosity monitor.

of events analyzed here required a logical OR of four conditions on sums of energy in the CAL cells: either the total transverse energy, excluding the towers immediately adjacent to the beam pipe in the forward direction, exceeded 11.6 GeV; or the total energy, excluding the towers immediately adjacent to the rear beam pipe and the first three (four) rings of EMC (HAC) towers around the forward beam pipe, exceeded 15 GeV; or the total EMC energy, excluding the same towers as in the previous case, exceeded 10 GeV; or the BCAL EMC energy exceeded 3.4 GeV.

The SLT rejected beam gas (and electronic noise) triggers according to the times measured in the CAL cells, using an algorithm that reduced the RCAL and BCAL FLT rates by approximately 90% and 50% respectively, but without any loss of physics events. The TLT then applied stricter cuts on the event time, and rejected beam halo and cosmic muons. The TLT for the 1993 running period also had available the full event information on which to apply physics-based filters. The TLT physics filter for photoproduction is explained in section 7.1.

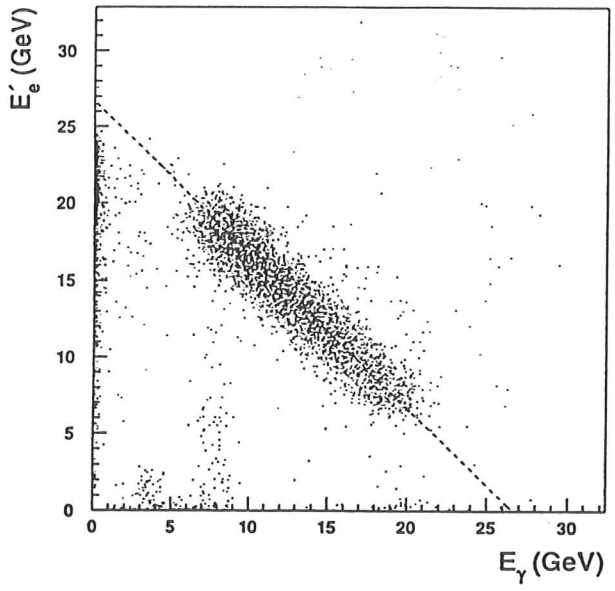

Figure 2.7: Distribution of the electron energy versus the photon energy measured in the ZEUS luminosity detector.

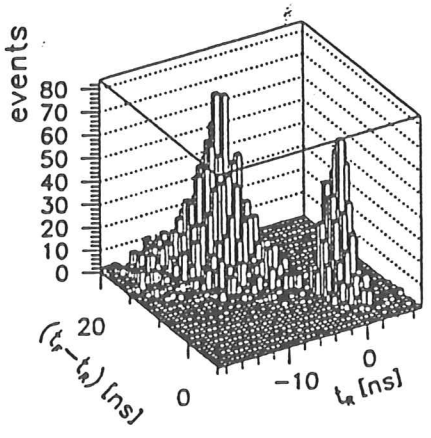

Figure 2.8: Distribution of the signal time measured by ZEUS in the RCAL (t_{RCAL}) versus the difference $t_{FCAL} - t_{RCAL}$ between signal times seen in FCAL and RCAL.

Chapter 3

Electron identification using the HES and CAL

Separation of hadrons and electrons is crucial for experiments at HERA. Even the simplest and most basic experiments must distinguish between charged current and neutral current events for which it is necessary to determine if any one of the high energy particles produced in the event was an electron. Separation of isolated electrons from hadrons by comparing the energy deposited in the EMC and HAC is relatively straightforward. The technique takes advantage of the differences in the longitudinal development of electron and hadron showers. However, electrons near or within hadron jets pose a special problem.

The electron-hadron (e-h) separation at ZEUS can be substantially improved by employing silicon pad detectors (diodes) behind a few radiation lengths in the EMC sections of the CAL. Semiconductor detectors (silicon diodes) are an almost ideal solution because they have excellent dE/dx resolution and large dynamic range, limited in practice only by the readout electronics; they are compact and have flexible design; they can be operated at low power with safe bias voltages at room temperature and are unaffected by magnetic fields; they contain no flammable gases for their operation. These properties indicate that semiconductor detectors should be very useful for e-h separation in calorimeters.

Electron-hadron separation in HES and CAL depends upon the fact that electron and hadron interactions behave differently in a calorimeter: electrons start showering early and the ensuing showers are narrow. Hadronic showers tend to be wide with low particle density. The HES is an essential detector component to measure non-isolated electrons, e.g. electrons coming from semileptonic decays of heavy flavour events.

We present here results on e-h separation in the ZEUS detector, comparing results from beam test data and single particle Monte Carlo, to determine the combined effectiveness of the HES and the CAL. The analysis was done on data taken at an experimental test performed at the CERN PS and SPS in 1988, using silicon detectors and the prototype ZEUS FCAL, in the energy range from 1 to 100 GeV. Results of the analysis performed with the 3, 5 and 9 GeV beam energy runs are shown [38]. Electrons and hadrons generated by a Single Track Generator and passed through the ZEUS Trigger Monte Carlo detector program ZG313T3 [39] were compared to the data. This analysis serves as a critical calibration of the HES Monte Carlo for e-h separation in real physics interactions where test data are not available.

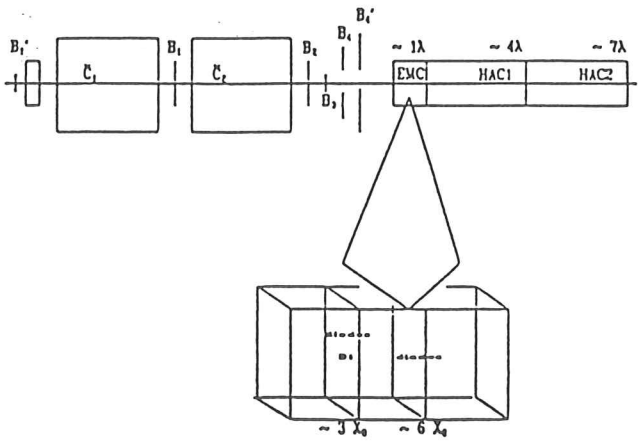

Figure 3.1: Experimental set-up of beam tests.

3.1 Beam test studies

The experimental set-up consisted of planes of silicon diodes that were inserted in FCAL DU-scintillator prototype modules (see figure 3.1). The module is divided into 16 towers which are read out independently. Two planes of diodes were inserted in the EMC portion of this prototype in towers 6 and 10. The beam was centrally shot at tower 6. CAL tests were done in parallel with occasional dedicated HES runs. Data were also taken for runs with one radiation length of extra material in front of the prototype FCAL in order to simulate the average amount of material in the ZEUS inner detectors. Thus these data more accurately reflect the expected performance of the ZEUS HES.

A coincidence of the beam defining counters, $B_1.B_2.B_3.\bar{B}_4$, was used to trigger the data acquisition system. Hadrons and electrons were then identified in the two Čerenkov counters C_1 and C_2. The pulse heights from the Čerenkov counters were sometimes included in the trigger in order to enhance the electron or hadron content of a particular run.

In order to determine the *e-h* separation on the silicon diodes, tight disjoint cuts were imposed on each of the two Čerenkov counters in order to identify electrons and hadrons; a particle was tagged as $e(h)$ only if it satisfied the $e(h)$ cuts in both counters. Some particles were not identified as either e or h, since the e and h cuts were disjoint, and were rejected. Table 3.1 shows the cuts used for both Čerenkov counters for the different energies studied (see figure 3.2).

Figure 3.3 shows the characteristic pulse height distributions on silicon pads for electrons and hadrons in ADC (Analog to Digital Converted) units at beam energies of 3, 5 and 9 GeV; the electron and hadron distributions are normalized to one. Most hadron signals are at a low pulse height; however, there is a long but weakly populated tail toward higher pulse heights. Electrons peak at distinctly higher pulse heights with an approximately Gaussian distribution.

Data were converted to units of *mip*'s (minimum ionizing particles) in order to compare later to Monte Carlo simulations. One *mip* was defined as the peak of the pulse height distributions

Energy	Cut for Hadrons	Cut for Electrons
3 GeV	$C_1 < 15(15); C_2 < 15(15)$	$C_1 > 50(60); C_2 > 50(60)$
5 GeV	$C_1 < 25(15); C_2 < 25(15)$	$C_1 > 50(70); C_2 > 60(70)$
9 GeV	$C_1 < 15(15); C_2 < 15(15)$	$C_1 > 70(75); C_2 > 70(75)$

Table 3.1: Cuts on Čerenkov counters for runs with (between brackets) and without material in front of the calorimeter.

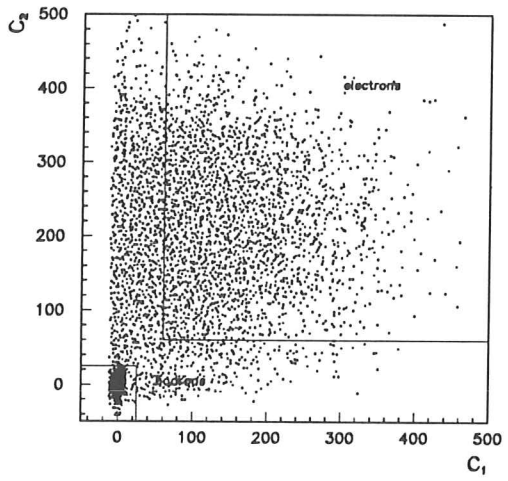

Figure 3.2: Pulse height correlation in the Čerenkov counters for 5 GeV runs.

of non-interacting hadrons, since a μ trigger was not available for these data samples. Figure 3.4 shows the pulse height distributions in *mip* units for the central diode in the first plane at 3, 5 and 9 GeV. Electrons and hadrons are normalized to one separately.

Electron - hadron separation can be achieved by cuts in the pulse height recorded for the silicon planes. The fraction of electrons with pulse height lower than the cut is defined as the electron inefficiency and the fraction of hadrons with pulse height higher than the cut is the hadron misidentification probability. Clearly, higher pulse height cuts imply lower hadron misidentification but also lower electron efficiency. The first two columns in table 3.2 show the hadron misidentification at 90% electron efficiency for one plane of diodes at two different depths and different energies. Clearly, satisfactory levels of *e-h* separation can be achieved with one plane of diodes inserted in the calorimeter. The improvement in hadron rejection with increasing energy seen in the second plane is due to the fact that the shower maximum moves deeper into the CAL as the electron energy increases.

Substantially improved *e-h* separation can be obtained using the correlation between the signals in two silicon planes placed at different depths in the calorimeter. Electrons and hadrons can be separated by using a hyperbolic cut in a two-dimensional analysis (see figure 3.5). The third column in table 3.2 shows the hadron misidentification at 90% electron efficiency for the correlation of two planes of diodes. These results illustrate directly the fact that two planes at different depths can separate hadrons and electrons more efficiently than only one at either

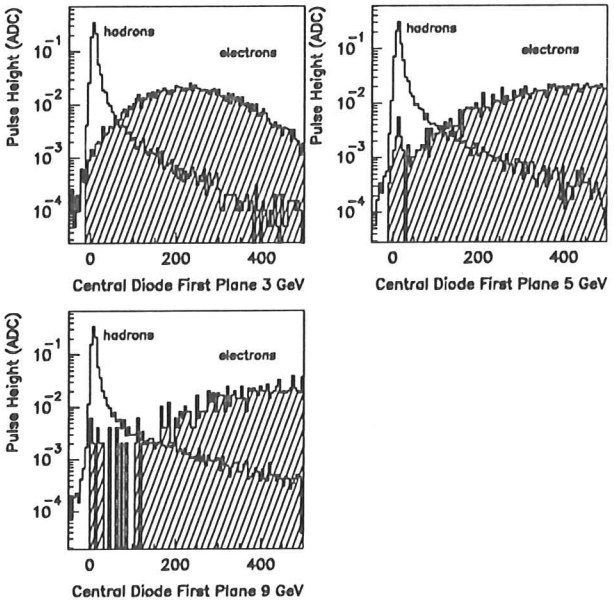

Figure 3.3: Pulse height distributions in ADC counts at 3, 5 and 9 GeV.

Energy	First Plane	Second Plane	Two Planes
3 GeV	3.7 ± 0.1 (2.9 ± 0.1)	4.1 ± 0.1 (6.1 ± 0.2)	0.8 ± 0.1 (1.2 ± 0.1)
5 GeV	3.7 ± 0.1 (2.6 ± 0.1)	2.9 ± 0.1 (4.4 ± 0.2)	0.6 ± 0.1 (0.9 ± 0.1)
9 GeV	3.8 ± 0.1 (3.3 ± 0.1)	1.7 ± 0.1 (2.6 ± 0.1)	0.7 ± 0.1 (0.9 ± 0.1)

Table 3.2: Hadron misidentification (in %) at 90% electron efficiency for the HES with (between brackets) and without extra material in front of CAL

depth.

In order to identify electrons in the calorimeter, the same Čerenkov cuts from table 3.1 were applied to define the beam. Figure 3.6 shows the energy deposited in the EMC. As can be seen in this figure, the EMC has energy deposited from minimum ionizing particles (left peak), early showering hadrons (central peak), and electrons (right peak). Figure 3.7 shows the e-h separation in the EMC. The first column in table 3.3 shows the hadron misidentification at 90% electron efficiency for the EMC. As can be seen in this table, there is an improvement in hadron rejection with increasing energy due to the fact that electrons give signals at larger pulse heights as the energy increases. The second column in table 3.3 shows the hadron misidentification at 90% electron efficiency, where electrons and hadrons are identified requiring that the fraction HAC/(HAC+EMC) is smaller than 0.015 for electrons and bigger than 0.015 for hadrons at all energies.

The HES beam test data have been used as a direct measurement of electromagnetic shower size. Data have been taken with the 3 and 9 GeV electron beam scanned across a diode in 3 mm steps (see figure 3.8) in the vertical direction. The beam defining counter was 3.5 mm wide. The approximate shower radius, as determined by the distance needed to reach half the shower maximum from either full pulse height or zero pulse height, is 6 mm. This is in fair agreement with Monte Carlo studies of shower development in the ZEUS CAL which indicate

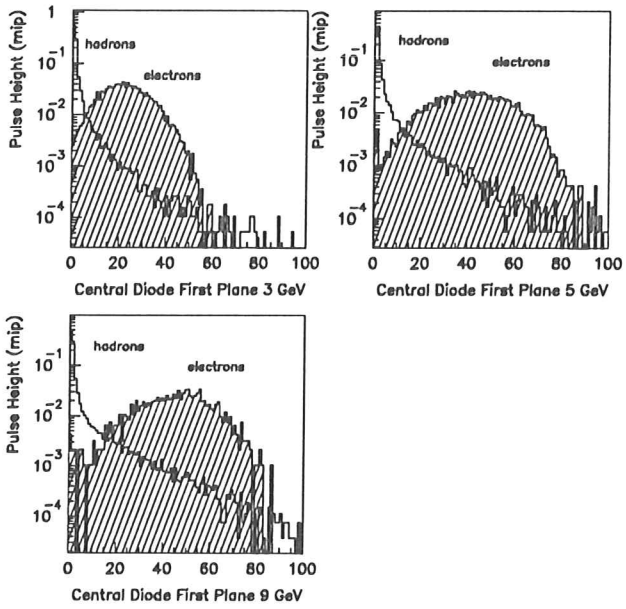

Figure 3.4: *e-h* separation in *mip*'s for central diode first plane.

Energy	EMC	EMC+HAC	EMC+HAC+lat dev
3 GeV	10.8 ± 0.3 (11.9 ± 0.3)	9.3 ± 0.2 (10.8 ± 0.3)	2.6 ± 0.2 (4.7 ± 0.2)
5 GeV	4.7 ± 0.2 (6.9 ± 0.2)	4.0 ± 0.2 (5.8 ± 0.2)	0.4 ± 0.1 (2.1 ± 0.2)
9 GeV	3.1 ± 0.1 (3.3 ± 0.1)	2.1 ± 0.1 (2.6 ± 0.1)	0.3 ± 0.1 (1.0 ± 0.1)

Table 3.3: Hadron misidentification (in%) at 90% electron efficiency with (between brackets) and without extra material in front of CAL.

that for these energies, at a depth of 3 radiation lengths, about 90% of the tracks in the electron shower are contained within a radius of 6 mm [40].

The *e-h* separation can be improved by taking advantage of the difference in lateral shower development of electrons and hadrons. This difference arises from the fact that electrons produce very narrow showers which will be most of the time concentrated in one strip of the EMC tower, whereas hadrons produce wider showers, hence a substantial fraction of their signals will be concentrated in the neighboring strips with high pulse heights and since electrons will deposit very low signals on these neighboring strips, this makes a good cut for better electron identification. At 3 and 9 GeV for runs with no material in front of the CAL and 3, 5 and 9 GeV for runs with extra material, the beam hits the central tower between strips 2 and 3, hence hadrons were rejected if their deposited energy in strips 1 and 4 was higher than 10 ADC counts for 3 GeV (no extra material), 15 ADC counts for 9 GeV (no extra material), 15 ADC counts for 3 GeV (extra material), 20 ADC counts for 5 GeV (extra material) and 25 ADC counts for 9 GeV (extra material). For the 5 GeV run with no extra material, the beam hits the central tower at the centre of the third strip, hence hadrons were rejected if the energy deposited in strips 1, 2 and 4 was higher than 20, 50 and 50 ADC counts, respectively. The last column in table 3.3 shows the hadrons misidentification at 90% electron efficiency for the combination EMC + HAC + *lateral development.*

In order to further improve the electron identification, the HES was added to the combi-

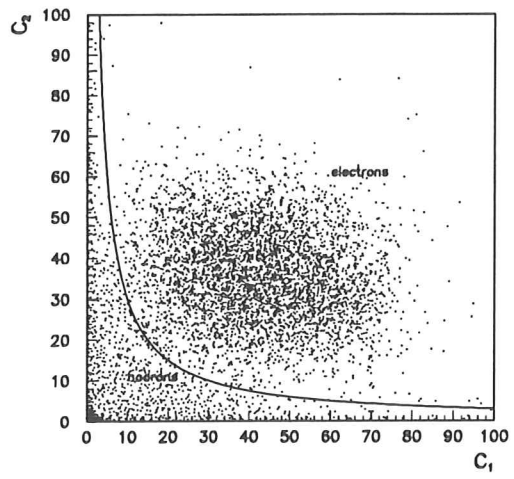

Figure 3.5: Pulse height distributions for central diode first plane vs. central diode second plane at 5 GeV.

Energy	EMC+HES	EMC+HAC+HES	EMC+HAC+HES+lat dev
3 GeV	2.5 ± 0.1 (2.0 ± 0.1)	1.7 ± 0.1 (1.4 ± 0.1)	0.7 ± 0.1 (0.8 ± 0.1)
5 GeV	2.1 ± 0.1 (1.6 ± 0.1)	1.4 ± 0.1 (1.3 ± 0.1)	0.2 ± 0.1 (0.6 ± 0.1)
9 GeV	2.1 ± 0.1 (2.8 ± 0.1)	1.5 ± 0.1 (1.0 ± 0.1)	0.1 ± 0.1 (0.4 ± 0.1)

Table 3.4: Hadron misidentification (in%) at 90% electron efficiency with (between brackets) and without extra material in front of CAL

nations of the different calorimeter elements. The first column in table 3.4 shows the hadron misidentification at 90% electron efficiency for the combination of EMC and HES (one plane). The second column shows the results for the combination EMC + HAC + HES and the last column in these tables shows the hadron misidentification for the combination EMC + HAC + HES + *lateral development*. As can be seen in the last column of these tables, a good electron identification with low hadron contamination can be obtained by taking advantage of all the elements present in the ZEUS CAL.

Comparing tables 3.2, 3.3 and 3.4, one can see that one plane of diodes gives a rejection factor of about 27 and two planes give a rejection factor of about 143 for 3 - 9 GeV. A combined analysis of EMC + HAC + *lateral development* gives a rejection factor of 38, 232 and 344 for 3, 5 and 9 GeV, respectively, whereas a combination of EMC + HAC + *lateral development* + HES gives a rejection factor of 143, 434 and 769, respectively. Therefore, the HES gives an improvement of factor 3.8, 1.9 and 2.2 for 3, 5 and 9 GeV, respectively.

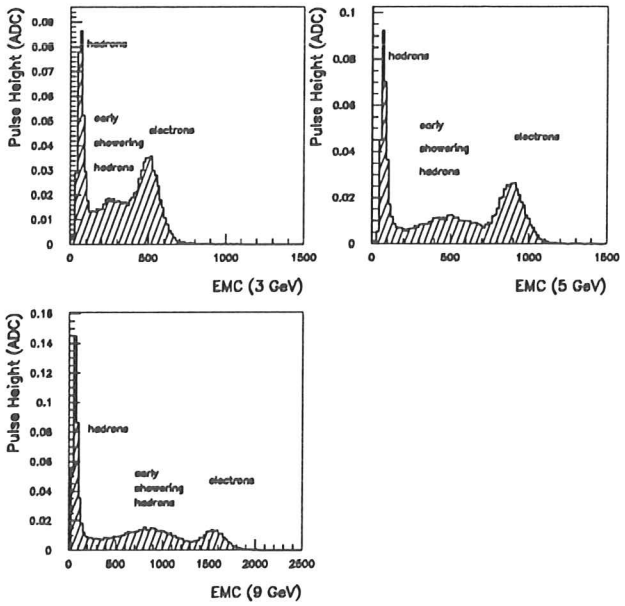

Figure 3.6: Energy deposited in the EMC.

3.2 Monte Carlo studies

Electrons and hadrons generated by a Single Track Generator and passed through the ZEUS detector simulation were compared to the data. The simulation was run using the standard ZEUS configuration as described in reference [39]. The beam was shot at normal incidence at the centre of a diode, the same relative position as in the beam tests. Figure 3.9 shows the energy deposited in *mip*'s by hadrons in the central diode of the first plane at 3, 5 and 9 GeV for data and Monte Carlo. The same distributions for electrons are shown in figure 3.10, where each of the distributions was normalized to one. As can be seen in figure 3.9, hadrons yield very similar distributions for data and Monte Carlo after the intrinsic electronic noise of the data has been simulated in the Monte Carlo. The noise was simulated [39] by adding random gaussian noise of 60 KeV width to the signal in each diode. The electrons also yield similar distributions (see figure 3.10), except for a larger tail in the Monte Carlo. This might be related to the fact that after about 50 *mip*'s, there is a saturation in the electronics used in these runs, lowering the pulse heights in the data.

A similar comparison was done for the calorimeter. Figure 3.11 shows the energy deposited in the EMC by hadrons, normalized to the beam energy. Data and Monte Carlo have similar distributions, though the data presents a longer tail. Figure 3.12 shows the energy distribution deposited in the EMC by electrons, normalized to the beam energy (both distributions were normalized to one). The Monte Carlo reflects the $\frac{15\%}{\sqrt{E}}$ resolution which has been put in by hand [39]. The data shows a resolution of around $\frac{20\%}{\sqrt{E}}$, in accord with the expected behaviour of the calorimeter. The results are the same for all three beam energies.

Tables 3.5 and 3.6 give the percentage of energy deposited for data and Monte Carlo in the CAL (EMC + HAC) for the central tower and the eight neighbours for hadrons and electrons, respectively. The percentage of energy deposited per tower for electrons and hadrons is similar for Data and Monte Carlo, hence the Monte Carlo reproduces closely both distributions.

Data			Monte Carlo		
2.0	4.3	3.0	1.1	4.6	1.1
3.2	69.4	8.8	4.3	77.9	4.1
2.0	4.4	3.1	1.1	4.6	1.1

3 GeV

Data			Monte Carlo		
3.1	6.7	2.1	1.3	4.8	1.3
6.2	71.8	3.4	4.5	76.3	4.4
1.9	3.0	1.6	1.3	4.8	1.3

5 GeV

Data			Monte Carlo		
1.6	4.6	2.7	1.4	4.4	1.4
2.9	78.0	1.0	4.3	77.2	4.2
1.6	4.9	2.8	1.4	4.5	1.4

9 GeV

Table 3.5: Tower content for hadrons

Data			Monte Carlo		
0.9	1.1	0.9	0.2	0.2	0.2
0.9	91.9	1.6	0.2	98.3	0.2
0.8	1.1	0.9	0.2	0.2	0.2

3 GeV

Data			Monte Carlo		
0.6	1.0	0.6	0.1	0.2	0.1
0.8	94.6	0.7	0.1	98.9	0.1
0.6	0.7	0.5	0.1	0.2	0.1

5 GeV

Data			Monte Carlo		
0.4	0.6	0.5	0.1	0.1	0.1
0.4	95.2	1.3	0.1	99.3	0.1
0.3	0.6	0.7	0.1	0.1	0.1

9 GeV

Table 3.6: Tower content for electrons

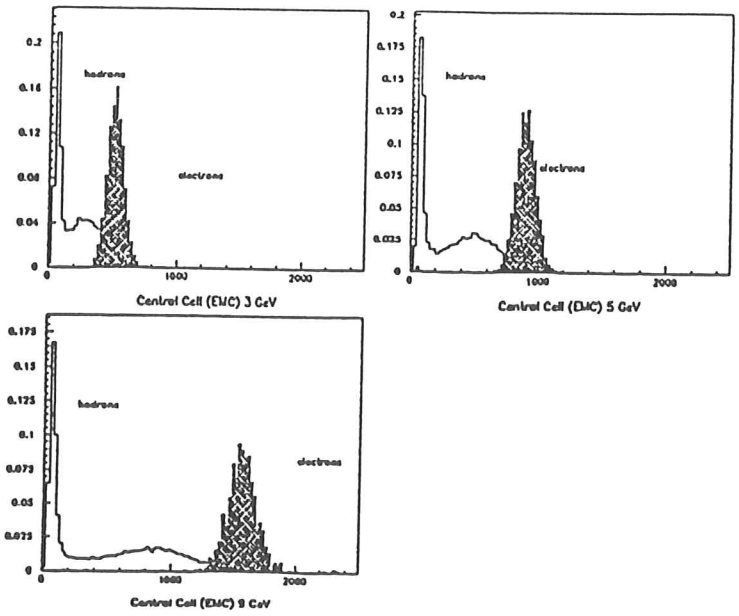

Figure 3.7: *e-h* separation in CAL.

	Data		Monte Carlo	
Energy	**electrons**	**hadrons**	**electrons**	**hadrons**
3 GeV	88.2% (86.2%)	9.2% (1.3%)	97.7% (94.7%)	1.4% (0.2%)
5 GeV	96.1% (95.7%)	2.0% (0.5%)	99.8% (98.2%)	0.7% (0.2%)
9 GeV	98.1% (97.5%)	3.7% (1.3%)	100% (99.5%)	0.6% (0.3%)

Table 3.7: Surviving events after cut **a** (**b**).

Figure 3.13 shows the fraction of energy deposited in the EMC by hadrons (EMC/(EMC + HAC)). As can be seen in the figure, the fraction of hadronic energy deposited in the EMC is well reproduced by the Monte Carlo.

In order to further compare the response of data and Monte Carlo, a set of cuts was applied on the combination of EMC and HES. The cuts applied were:

- a) $0.8 \leq \frac{E_{EMC}}{E_{beam}} \leq 1.2$, or,
- b) $0.8 \leq \frac{E_{EMC}}{E_{beam}} \leq 1.2$ and $E_{HES} \geq 5$ *mip*'s

Table 3.7 gives the percentage of electrons and hadrons that survived the cuts. As can be seen in these tables, electrons and hadrons are approximately reproduced by the Monte Carlo. However, hadrons yield a factor 7, 3 and 6 for 3, 5 and 9 GeV smaller in the Monte Carlo after cut **a** and 7, 2, 5 respectively after cut **b**. This effect can be explained by the fact that the Monte Carlo has a smaller tail than the data for hadrons. When EMC+HAC+*lateral development* cuts are applied to the data in order to have a better identification of hadrons and electrons, the Monte Carlo reproduces the data in a much closer way (see table 3.8).

Summarizing this chapter, an analysis on the CERN PS-SPS beam test data has been performed. Studies were done to test the HES and CAL electron identification at low energies. The results prove that a good electron identification with low hadron contamination can be

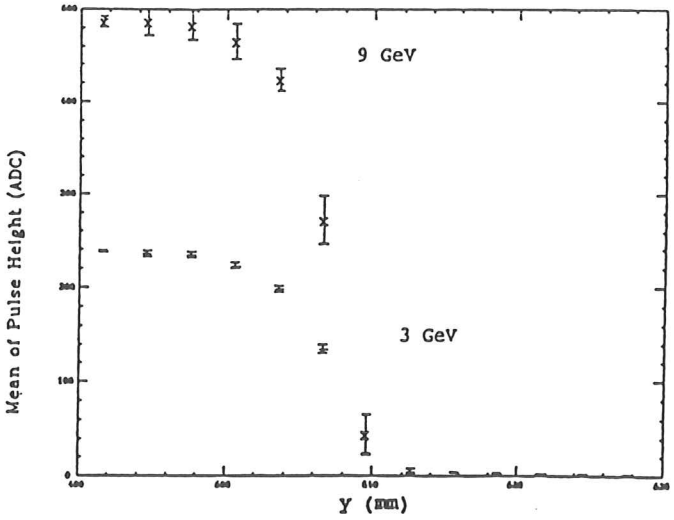

Figure 3.8: Lateral shower development at 3 and 9 GeV.

	Data		Monte Carlo	
Energy	**electrons**	**hadrons**	**electrons**	**hadrons**
3 GeV	88.9% (86.7%)	3.2% (0.5%)	97.7% (94.7%)	1.4% (0.2%)
5 GeV	97.6% (97.2%)	0.7% (0.1%)	99.8% (98.2%)	0.7% (0.2%)
9 GeV	99.7% (99.5%)	0.5% (0.1%)	100% (99.5%)	0.6% (0.3%)

Table 3.8: Surviving events after cut **a** (**b**) after EMC+HAC+lat development cuts.

achieved by using all the elements available in the CAL. A comparison to single particle Monte Carlo simulation was also carried out. From the different tests done, one can conclude that the Monte Carlo reproduces the data fairly well, though differences have been seen in the tails of some distributions.

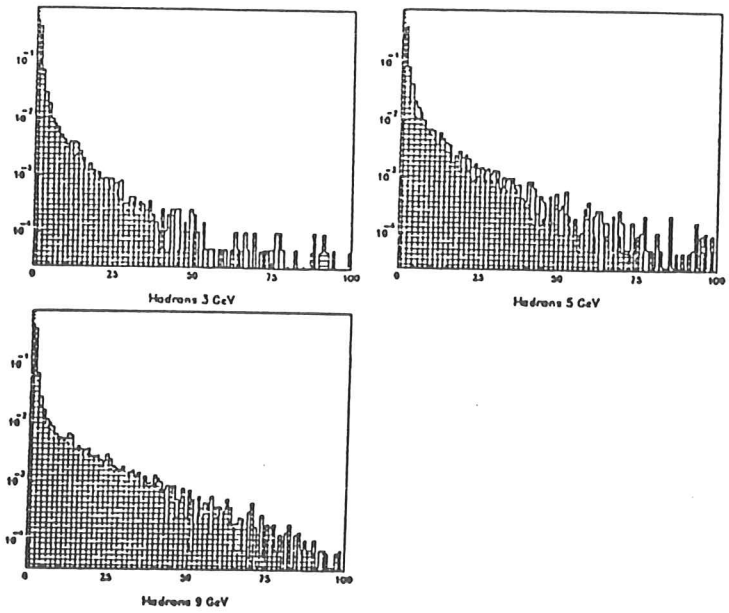

Figure 3.9: Hadrons in Monte Carlo (horizontal lines) and data (vertical lines) - HES.

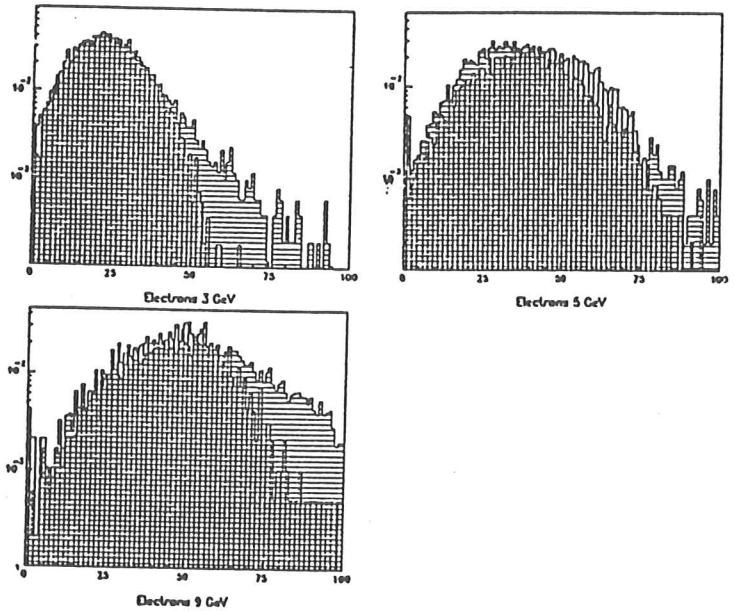

Figure 3.10: Electrons in Monte Carlo (horizontal lines) and data (vertical lines) - HES.

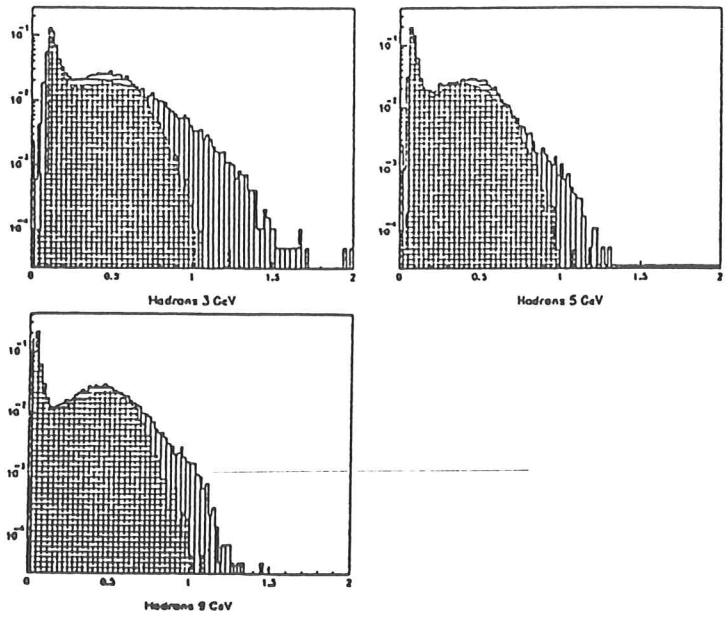

Figure 3.11: Hadrons in Monte Carlo (horizontal lines) and data (vertical lines) - EMC.

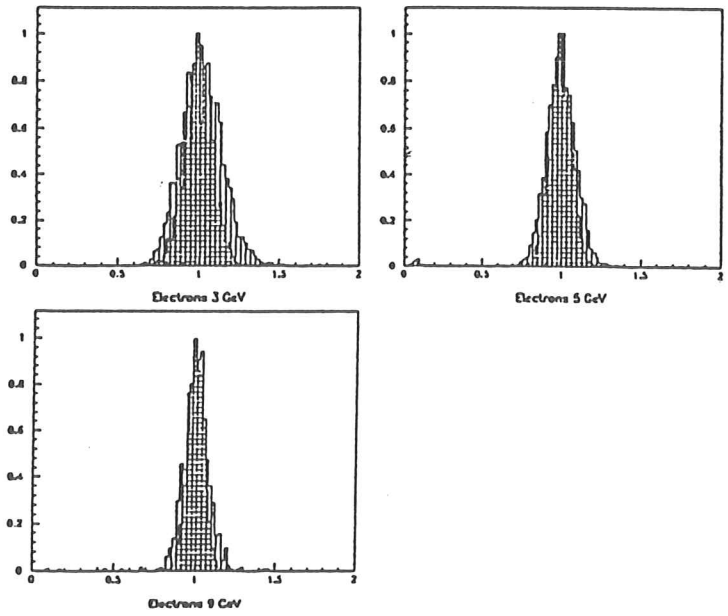

Figure 3.12: Electrons in Monte Carlo (horizontal lines) and data (vertical lines) - EMC.

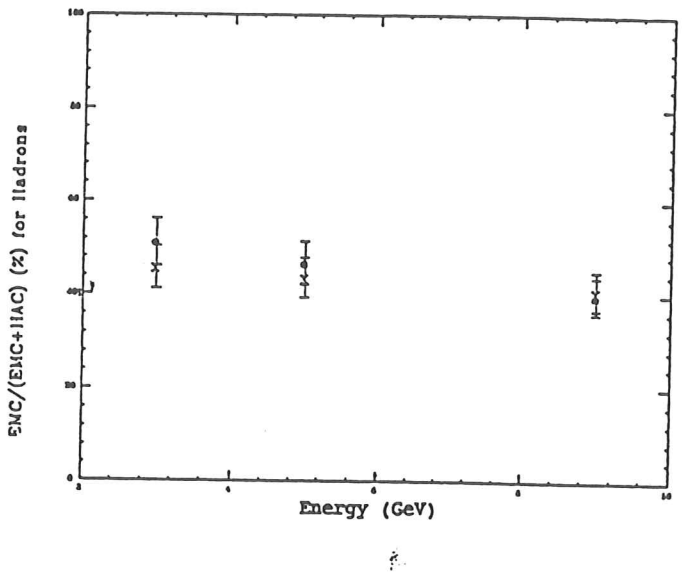

Figure 3.13: $EMC/(EMC + HAC)$ for hadrons in data (points) and Monte Carlo (cross).

Chapter 4

Observation of jet production at low Q^2

Hard collisions between quasi-real photons and partons from the proton give rise to two or more partons in the final state. In this case, the appearance of sprays of hadrons (jets) which come from the parton fragmentation are expected. Experimental evidence has confirmed this prediction, jets have already been observed in hadron-hadron collisions [21].

The first observation of jet structure in photoproduction was presented in ref. [6]. First evidence for jet structure in resolved processes was also presented there. Lately, it was shown that resolved processes dominate jet production in a wide kinematic range and the first evidence for the observation of two-jet structure in direct processes was reported [14]. After separating clearly both contributions, the measurement of the dijet cross sections for resolved and direct processes was performed.

In this chapter, the analysis that led to the observation of jet production at low Q^2 is presented [6, 14, 41, 42, 43]. The data sample used in the analyses presented in this chapter and chapters 5 and 6 was collected during 1992 with the ZEUS detector and corresponds to an integrated luminosity of 25.5 nb^{-1}. First, the selection criteria devised to obtain a clean sample of photoproduction events is discussed and the Monte Carlo simulation used in this chapter and chapters 5 and 6 is described. Then, the characteristics of the event sample obtained are studied and it is proven that the final selected sample is coming from *ep* collisions and that the events originate from photoproduction processes. Once a sample of photoproduction events has been isolated, we search for evidence of jet production in our data. The last section of this chapter is devoted to the study of inclusive jet production and its characteristics. Results on dijet production are presented in chapter 5.

4.1 Hard photoproduction data selection

Photoproduction processes are characterized by the fact that the outgoing electron is scattered at small very angles with respect to the initial electron direction (i.e. low-Q^2 values). These interactions can then be tagged by using the luminosity monitor which covers a range from 4 10^{-8} to 0.02 GeV^2 in Q^2. On the other hand, the main detector imposes a limit of $Q^2 > 4$ GeV^2 to tag the scattered electron. In order to have a data sample as large as possible, events were not constrained to have a signal in the luminosity monitor. We relied on other means to select photoproduction interactions and used the subsample of events with a signal in the electron calorimeter of the luminosity monitor (tagged events) to ensure the photoproduction origin of the whole sample.

A sample of photoproduction candidate events was isolated by taking advantage of the

features of the hadronic final state measured in the CAL. By using this method of isolation, the main source of physics background expected is from neutral current DIS, whose final state is characterized by the presence of the scattered electron at an angle $\theta < 176°$ (i.e. large-Q^2 values). This background is rejected by searching electromagnetic clusters in the CAL with characteristics compatible with the scattered electron in DIS. The number of charged current events expected is negligible for the 1992 integrated luminosity due to its small cross section.

The data taken by the ZEUS detector during the 1992 running period (see section 2.3) were passed through an offline filter designed to isolate hard photoproduction events [6, 14, 44]. The conditions set up in this offline filter were:

– no signal from the C5 counter in time with the proton beam

– no signal from the vetowall counter

– $|t_{FCAL}|$, $|t_{RCAL}|$, $t_{FCAL} - t_{RCAL} \leq 6$ ns

– REMC or BEMC trigger bit on

– $E_{RCAL} \geq 2.5$ GeV $\otimes$ $E_{FCAL} \geq 10$ GeV (branch 1) $\oplus$ $E_{TOT} \geq 20$ GeV $\otimes$ $E_{TR} \geq 10$ GeV $\otimes$ $E_{RCAL} \leq 40$ GeV $\otimes$ $\not{P}_T \leq 10$ GeV (branch 2).

where E_{TR} is the total transverse energy and $\not{P}_T$ is the missing transverse momentum. The first three requirements reject beam gas collisions with a negligible effect on ep interactions. The latter two require significant hadronic activity in the CAL and, in particular, they select the hardest collisions from the bulk of photoproduction interactions.

This filter reduced approximately four million triggered events from the 1992 data taking period to about 350,000 candidate events. Cosmic rays and beam halo muons were rejected at this stage with a suitable algorithm which takes into account the topology of these events seen in the CAL [7]. Then, events in data taking periods with the CTD or the magnet switched off were removed and more refined timing cuts were applied. A visual scan of a subsample of the remaining events and the analysis of the events coming from the unpaired proton bunch revealed that beam gas background was still large. At this stage, this contamination was estimated (using the BCN = 9) to be about 71%. About 22% of the sample was triggered by the REMC, with a proton beam gas contamination of 5%, and 78% of the sample was triggered by the BEMC, with a 90% proton beam gas contamination. The contamination coming from electron gas interactions was estimated to be negligible since no event from the unpaired electron bunch was found in the sample.

A second filtering stage was set up [41, 45] in order to reject the proton beam gas contamination with a minimal loss of physics events. Details on the selection criteria applied in this second filter can be found in appendix A. The conditions are:

Beam gas and cosmic rejection:

– accept events with $E_{RCAL} < 30$ GeV.

– a) rejection of REMC-triggered events with $t_{RCAL} <$ -3 ns and,
b) rejection of BEMC-triggered events with $|t_{BCAL}| > 8$ ns

– only events with a reconstructed vertex are accepted

– an event is accepted if $|14 \cdot t_{FCAL} + z| < 40$ (with t_{FCAL} in nsec and z in cm)

– rejection of events with $(E - p_z)/(2E_e) < 0.2$

DIS neutral current rejection:

– reject events with an electron candidate with $y_e < 0.7$

– reject events with $(E - p_z)/(2E_e) > 0.7$

where E is the total energy of the event as measured by the CAL, p_z is given by $\Sigma E^{cell} \cdot \cos\theta_{cell}$ with the sum carried over all CAL cells and the polar angle of the cell is computed using its geometrical centre and the vertex of the interaction as measured by the tracking detectors. The

variable y_e is given by

$$y_e = 1 - \frac{E'_e}{2E_e}(1 - \cos\theta'_e)$$

where E'_e denotes the energy of the electron candidate as measured by the CAL and θ'_e is the polar angle of the candidate as measured by the point of impact in the CAL and the vertex of the interaction.

In addition, only events with $E_{TR} > 10$ GeV were accepted in order to study the hard part of the spectrum. Monte Carlo studies show that soft photoproduction processes (elastic, single-diffractive, double-diffractive and low-p_T), have a tail in E_{TR} that does not extend beyond 10 GeV [6].

After the application of all these selection criteria, the final sample contained 19,589 events. The remaining beam gas contamination was estimated to be about 0.3% and the cosmic ray contamination, below 0.1%. The contamination from DIS events with an electron in the CAL ($Q^2 \geq 4$ GeV^2) was estimated by using Monte Carlo techniques to be below 0.5%.

4.2 The Monte Carlo simulation

The hadronic final state in ep scattering at low Q^2 has been modelled using the Monte Carlo programs PYTHIA [46] and HERWIG [47]. Direct and resolved processes are simulated in these generators according to the leading order matrix elements. These matrix elements are singular in the limit $\hat{p}_T \rightarrow 0$, hence a lower cutoff is imposed. Monte Carlo samples were generated setting this lower cutoff at 2.5 GeV/c.

Initial and final parton showers are included in both generators, though according to different models. The PYTHIA generators uses the LUND string model [48] as implemented in JETSET [49] to perform the fragmentation into hadrons. The cluster model is used in the case of the HERWIG program to fragment the partons.

The lepton vertex has been treated in the Weizsäcker-Williams approximation, with the scattered electron forced along the beam direction, except in the case of direct processes generated by the HERWIG program, where exact matrix elements have been used.

Different parametrizations of the photon and proton structure functions were used in order to study the behaviour of the distributions of the jet properties with the various prescriptions. The photon structure function was parametrized according to the prescriptions: LAC1 [25], GRV [26] and DG [29], and the parton densities in the proton were described via the parametrizations MRSD0 and MRSD− [27].

Samples of resolved and direct events generated by both programs were passed through a detector simulation which is based on the general purpose program GEANT 3.13 [50]. The description of the responses of the various detector components was tuned in this simulation to reproduce test data. Then, these samples were processed with the trigger and the same offline reconstruction procedure as the data.

4.3 Characteristics of the event sample

In section 4.1, the selection criteria that were set up in order to isolate a clean sample of photoproduction events were described. This section is devoted to prove that the final selected sample is indeed coming from ep collisions and that it is originated from photoproduction processes.

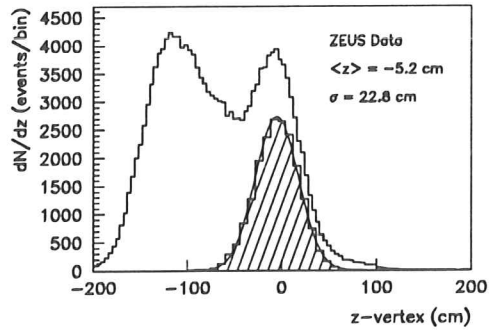

Figure 4.1: z-Vertex distribution: total sample (white histogram); final selected sample (shaded histogram).

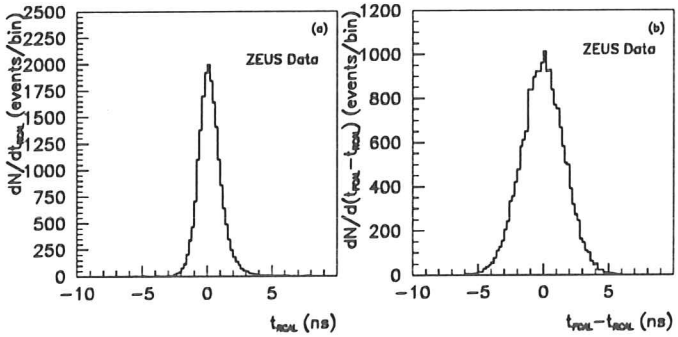

Figure 4.2: Calorimeter timing distributions for the final selected sample: (a) t_{RCAL}; (b) $t_{FCAL} - t_{RCAL}$.

Figure 4.1 shows the z-Vertex distribution of the selected sample (shaded area). The distribution is centered at -5 cm and the width is 23 cm. This is in agreement with the mean value of the z-position of the interaction point and the length of the proton beam bunch and shows that the contributions from non-ep backgrounds are negligible. The t_{RCAL} and $t_{FCAL} - t_{RCAL}$ distributions are shown in figures 4.2a and 4.2b, respectively. These distributions are centered at zero and fall rapidly confirming that the selected sample has no significant background from non-ep interactions.

The γp centre of mass energy ($W_{\gamma p}$) is given via the formula

$$W^2_{\gamma p} = 4E_\gamma E_p$$

The photon energy for the whole selected sample (tagged and untagged) can be estimated via $E_\gamma \approx y_{JB} E_e$ (W_{CAL}), where $y_{JB} = \frac{E-p_z}{2E_e}$ based on the Jacquet-Blondel method [51]. The range in W_{CAL} extends from 130 GeV to 250 GeV (see figure 4.3). The subsample of events with an electron in the luminosity monitor (the electron energy in the range 5 GeV $\leq E_{eLUMI} \leq$ 25 GeV, where E_{eLUMI} is the energy of the scattered electron as measured by the luminosity monitor) was used to ensure that the selected sample consists of photoproduction events. There are 5390 events with an electron in the luminosity monitor with an energy in the range quoted above, which corresponds to about 28% of the sample. This is in agreement with the expectations from the Monte Carlo simulations, since in a certain fraction of photoproduction events the scattered electron hits the electron calorimeter of the luminosity monitor. The W_{CAL} distribution for the

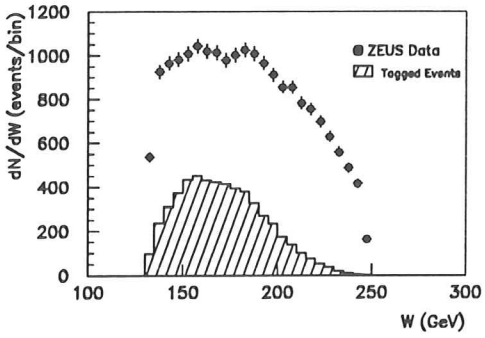

Figure 4.3: W distribution for the final selected sample. The distribution for the subsample of tagged events is included as a shaded histogram.

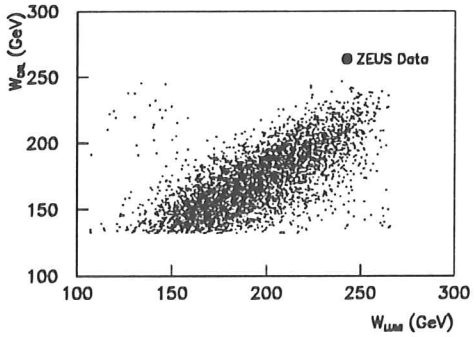

Figure 4.4: Correlation between W computed from the calorimeter energy deposits (W_{CAL}) and W computed from the electron energy measured in the luminosity monitor (W_{LUMI}).

tagged events is shown in figure 4.3 (shaded histogram). The shape of W_{CAL} distribution for the tagged sample is somewhat different from the one for the whole sample due to the restricted acceptance of the luminosity detector.

For the tagged events, $W_{\gamma p}$ can also be estimated by using the electron energy measured in the luminosity monitor (W_{LUMI}), via $E_\gamma = E_e - E_{eLUMI}$. Thus, a comparison of the $W_{\gamma p}$ as measured from the LUMI electron and from the hadronic system can be made. As can be seen in figure 4.4, the correlation is good. The W_{LUMI} estimation has an error of $\sim$ 2%, whereas the W_{CAL} measurement is influenced by the loss of particles in the rear beam pipe and in inactive material in front of the CAL. Monte Carlo studies show that these effects result in a systematic underestimation of W by W_{CAL} of about 10%; as can be seen in figure 4.5, this effect is adequately reproduced in the Monte Carlo simulation of the detector. These results allow us to reconstruct $W_{\gamma p}$ for all events (tagged and untagged) using the W_{CAL} estimation.

Taking into account the characteristics of the sample described above, we can conclude that the sample of events selected is due to photoproduction interactions at an average uncorrected centre-of-mass energy of about 180 GeV.

The selected sample consists of events coming from the hard part of the spectrum of the photoproduction interactions due to the condition $E_{TR} \geq 10$ GeV. The distributions for E_{TR} and the missing transverse momentum are shown in figure 4.6a and 4.6b, respectively, for the whole sample and the tagged events, together with the prediction of the Monte Carlo simulation

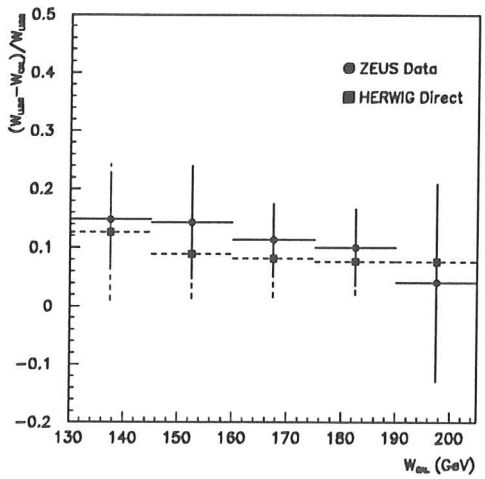

Figure 4.5: $(W_{LUMI} - W_{CAL})/W_{LUMI}$ as a function of W_{CAL}.

of HERWIG including resolved and direct processes. The total transverse energy deposit is large whereas the whole event is well balanced (small missing transverse momentum). This is what is expected in hard scattering in γp processes, where the final state consists of two back-to-back (in the transverse plane) jets with high transverse momentum balancing each other. Moreover, these events can not come from soft interactions since the E_{TR} is large, $E_{TR} > 10$ GeV. The Monte Carlo simulation of hard processes is in rough agreement with the data. The subsample of tagged events shares the same behaviour as the whole sample for both distributions.

The energy depositions in the different parts of the CAL can be used to check whether the Monte Carlo simulation gives an acceptable description of the events and if the observed distributions are consistent with what is expected in hard photoproduction as predicted by QCD. Figure 4.7 shows the energy and transverse energy depositions in the different parts of the CAL for the whole sample and for the subsample of tagged events. Both samples share the same characteristics. A comparison to the Monte Carlo simulations of HERWIG is shown as well. The sample shows a large energy deposit in the FCAL and a sizeable one in the RCAL, whereas the transverse energy in the FCAL is large, but in the RCAL is small. Hence, the large transverse energy activity is mainly associated to the forward direction. These energy depositions can be interpreted as the two jets and the remnant of the proton in the forward direction and the remnant of the photon in the rear; the two partons coming from the hard scattering are expected to be boosted to the forward direction due to the very asymmetrical configuration of the beams. The predictions for these distributions of the QCD-based Monte Carlo simulation are in agreement with the data.

Hence, we can conclude that the selected sample is coming from ep interactions since:

– the background from beam gas and cosmic rays are at a very low level (0.3% and below 0.1%, respectively)

– the z-Vertex and CAL timing distributions are well behaved and consistent with the expectations

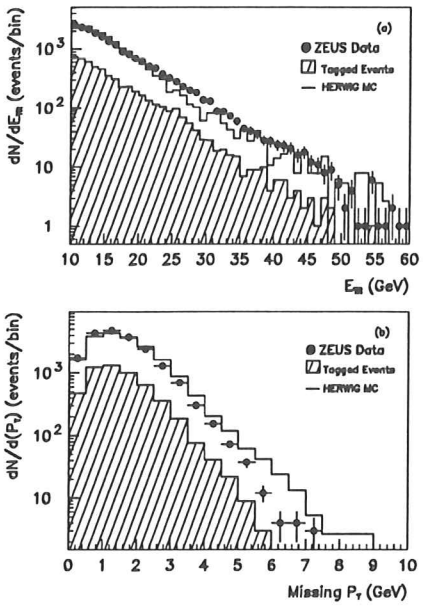

Figure 4.6: Transverse energy distribution (a) and missing transverse momentum (b) for the final selected sample. The distribution for the subsample of tagged events is included as a shaded histogram. The Monte Carlo simulation of HERWIG, normalized to the total number of events has been included as well (solid line).

Furthermore, it is originated from photoproduction processes since:

– the scattered electron is not hitting the main detector ($Q^2 < 4$ GeV^2), and the remaining DIS contamination with $Q^2 \geq 4$ GeV^2 is below 0.5%

– the total transverse momentum is well balanced

– the fraction of tagged events is consistent with expectations

– the kinematic distributions for the selected sample and for the subsample of tagged events share similar characteristics.

In addition, the sample comprises events from the hardest part of the transverse energy spectrum. The predictions of the QCD-based Monte Carlo simulations of hard scattering processes are in agreement with the data.

4.4 Observation of jet production

Our data sample shows a large deposit of transverse energy. In particular, the observed large tail in the transverse energy spectrum can not be explained in terms of soft processes. Moreover, the cross section integrated in transverse energy $\sigma(E_{TR} > E^0_{TR})$ has been measured [6] and found to be in agreement with the QCD-based expectations of the HERWIG generator. These facts lead naturally to the explanation that the events are the result of the hard scattering of the photon (and its constituents) and the partons in the proton. In this case, QCD predicts that the transverse energy appears as sprays of hadrons (jets) which are the result of the parton fragmentation. Furthermore, QCD predicts that two-jet production should dominate as the transverse energy increases, as it has been observed in hadron colliders. Hence, we first look for evidence of jet production in our sample. Once jet structure has been observed, we compare

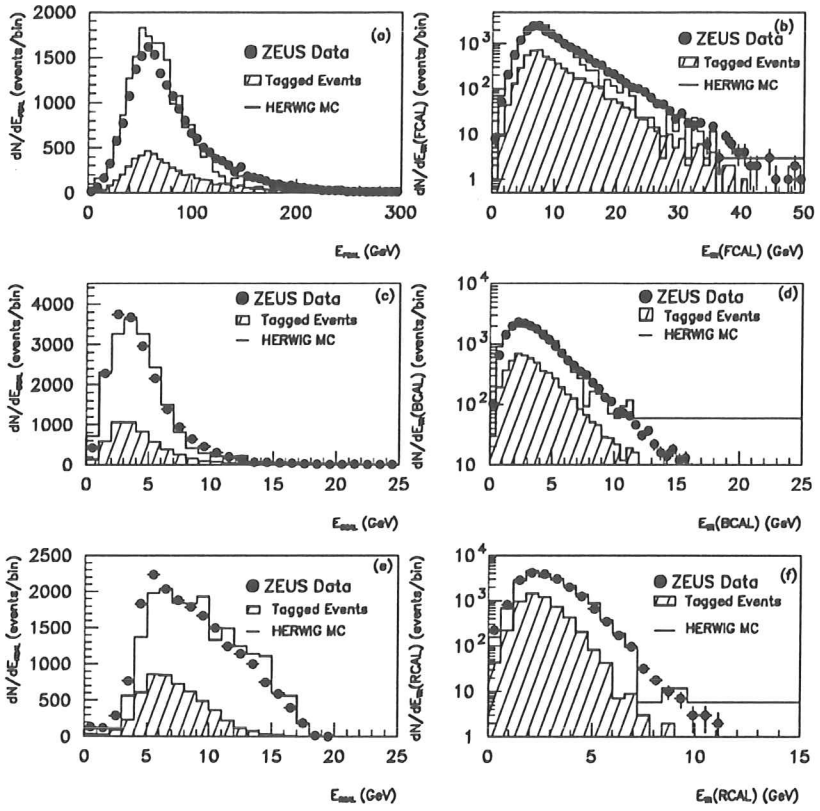

Figure 4.7: Distributions of the FCAL (a), BCAL (c) and RCAL (e) total energies, and of the FCAL (b), BCAL (d) and RCAL (f) transverse energies. The distribution for the subsample of tagged events is included as a shaded histogram. The Monte Carlo simulation of HERWIG, normalized to the total number of events has been included as well (solid line).

the rates to the QCD predictions. Then, we look into the inclusive jet distributions to check that the observed jet properties (jet transverse energy spectrum) are in agreement with QCD and, to study jet variables (like the jet pseudorapidity spectrum) which are sensitive to the underlying process, resolved or direct.

The multijet structure found in hard photoproduction interactions is expected to be similar to the one observed in hadron-hadron collisions [21]. Cone algorithms are generally used in hadronic collisions to reconstruct jets in the final state due to the presence of the fragments of the spectator partons (remnants). In this type of algorithm, jets are reconstructed taking into account only the particles inside a cone of fixed radius and according to transverse energy deposits. Hence, we have used a cone algorithm to look for jet structure in our sample.

We have searched for jet structure in the selected data sample using a jet cone algorithm [52] in pseudorapidity (η) - azimuth (φ) space [53, 54]. For the purpose of the present analysis, CAL cells in a cone of 10° ($\eta > 2.44$) with respect to the proton beam direction were excluded from the jet search. The $\eta - \varphi$ position of each CAL cell was taken from the unit vector joining the vertex of the interaction and its geometrical centre. In a first step, CAL cells with a transverse energy in excess of 300 MeV were considered as initiators for the search. These initiators were joined if the distance between them in $\eta - \varphi$ space, $R = \sqrt{\Delta\varphi^2 + \Delta\eta^2}$, was smaller than 1 unit.

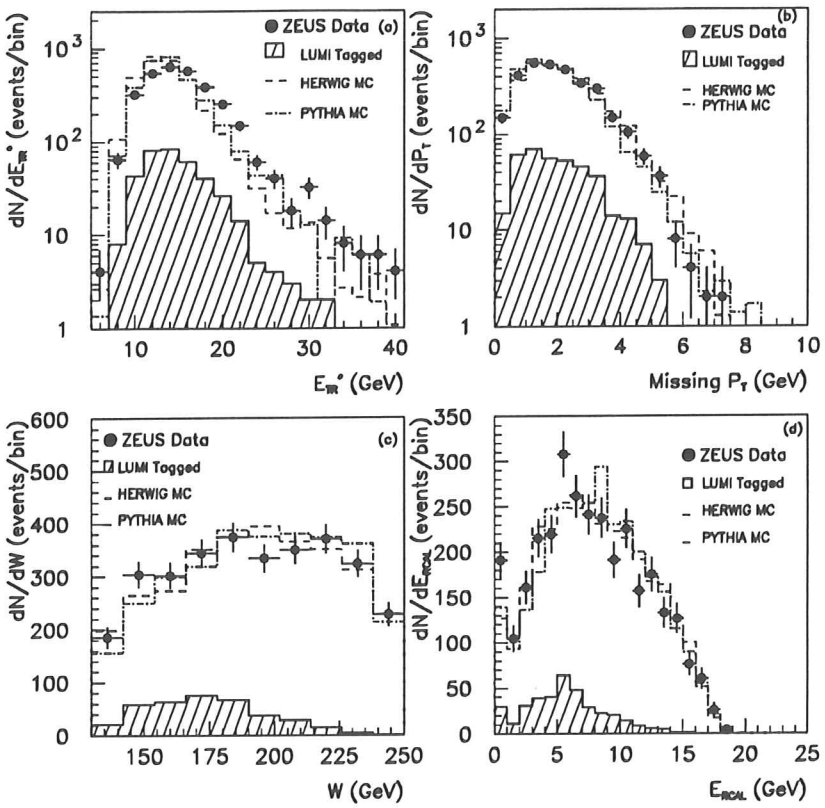

Figure 4.8: General characteristics of the events with jet structure: (a) E^*_{TR}, (b) missing transverse momentum, (c) W and (d) RCAL energy distributions. The data (solid dots) and the tagged subsample (shaded area) are compared to the predictions of the HERWIG (dashed) and PYTHIA (dash-dotted) Monte Carlos.

Then a cone of radius 1 unit, $R = 1$, was drawn around each initiator and the CAL cells within that cone were added to the initiator to form a cluster. The axis of the cluster was defined according to the Snowmass Convention [54]: η(cluster) and φ(cluster) are the transverse energy weighted mean pseudorapidity and azimuth of all the CAL cells belonging to that cluster. A new cone of radius 1 unit is drawn around the axis of the cluster. All cells inside the cone are used to recalculate a new cluster axis. The procedure is iterated until the content of the cluster does not change. The ambiguities concerning overlapping clusters are then considered: two clusters are merged if the sum of the transverse energies for the cells which are common to them exceeds 75% of the total transverse energy of the cluster with the lowest transverse energy; otherwise two different clusters are considered and the common cells are associated to the nearest cluster. The total transverse energy associated to each cluster, E_T(cluster), is taken to be the sum of the transverse energies of the cells belonging to it. The final clusters of cells were called jets if E_T(cluster) was larger than 5 GeV. Jets were accepted for the present analysis if η^{jet} was less than 1.6 ($\theta > 22.8°$). In addition, the cone radius R in the algorithm was varied to 0.7 units to study the dependence of jet production on the cone radius.

The application of this algorithm with $R = 1$ unit to the selected sample (19,589 events) yields 1264 (6.5%), 266 (1.4%) and 18 (0.1%) events of the one-jet, two-jet and three-jet type.

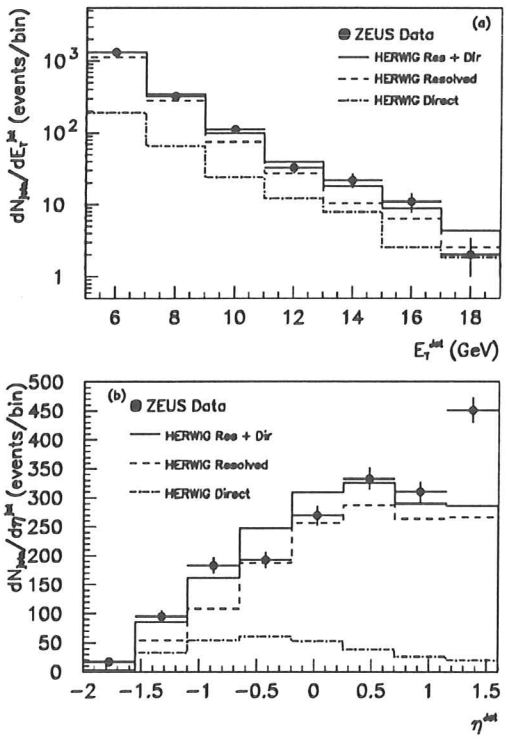

Figure 4.9: Inclusive jet distributions for (a) transverse energy of jets, (b) pseudorapidity of jets, where the Monte Carlo distribution is normalized to the data in the region $\eta^{jet} < 1.2$, as discussed in the text. The relative contributions of the direct and resolved processes as predicted by the Monte Carlo simulation are also shown.

The fact that most of the events are of the zero-jet type is a consequence of the pseudorapidity cut. Due to the very asymmetrical configuration of the colliding beam particles, many of the jets are expected to be boosted in the proton beam direction beyond the fiducial region considered in the jet finding.

From a comparable number of Monte Carlo events, the HERWIG generator predicts the fractions to be in the range 6.3-9.8% and 0.7-1.9% for the one-jet and two-jet categories, respectively. The quoted ranges indicate the spread of the values obtained with the different proton and photon parton distributions. The agreement between data and Monte Carlo for the jet multiplicities is also good if the radius of the cone is set to 0.7 units. The fraction of three-jet events in the Monte Carlo sample, which does not include higher order matrix elements, is 0.01%.

Before studying the jet properties, we have checked that the global variables of the events with jet structure are in agreement with the expectation of the QCD based Monte Carlo simulation. The global variables of the events with jet structure are shown in figure 4.8. The distributions of the total transverse energy outside a cone of 15° with respect to the proton beam direction (E^*_{TR}) (figure 4.8a), the missing transverse momentum (figure 4.8b), W_{CAL} (figure 4.8c) and the energy in the RCAL (figure 4.8d) for the data are compared to the Monte Carlo simulations (normalized to the data) of HERWIG and PYTHIA including resolved plus direct processes. It should be noted that the data in these and subsequent figures are not cor-

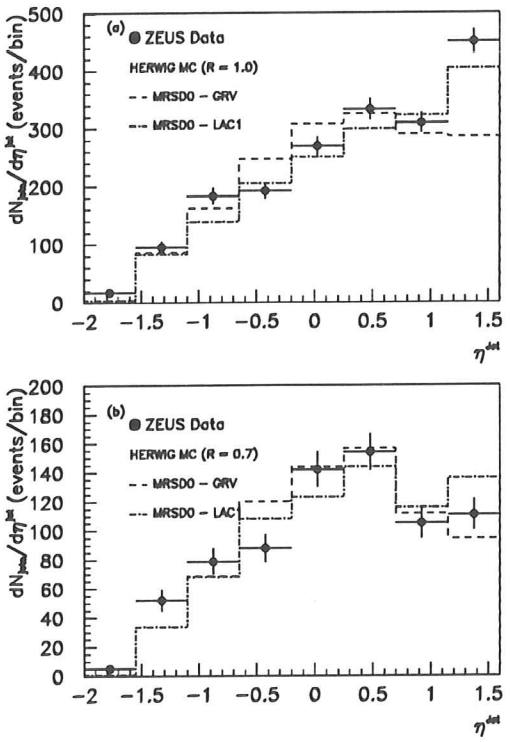

Figure 4.10: (a) Inclusive jet pseudorapidity distribution (with $R = 1.0$): data (solid dots) and the predictions of HERWIG including resolved and direct processes for two choices of the photon parametrization (GRV: dashed line; LAC1: dot-dashed line) and MRSD0 for the proton. (b) The same as (a) but with the cone radius set to 0.7 units.

rected for energy absorbed in inactive material nor for resolution smearing and other detector effects. These effects are included in the Monte Carlo simulation. Only statistical errors are quoted in the figures. The distributions for the tagged sample are shown as shaded areas. The features of the whole sample are in agreement with the ones of the tagged sample. The differences in the W_{CAL} and E_{RCAL} distributions reflect the restricted electron energy acceptance in the luminosity monitor. The Monte Carlo simulations of resolved and direct processes provide a good description of the global event shapes of the data. The E^*_{TR} spectrum shows a large tail while the missing transverse momentum is small. These are the properties of hard scattering events in γp processes, where the final state consists of two back-to-back partons well balanced. The E_{RCAL} distribution, where the photon remnant energy deposit is expected, is well reproduced by the Monte Carlo simulations which include resolved processes. The uncorrected γp centre-of-mass energy for the sample of events with jets ranges from 130 to 250 GeV.

The inclusive jet sample consists of 1850 jets. The jet transverse energy (E_T^{jet}) distribution, shown in figure 4.9a, falls steeply, and reaches values as high as 18 GeV. The Monte Carlo distribution (normalized to the data) for HERWIG including resolved+direct processes with parton densities in the proton and in the photon parametrized according to MRSD− and GRV, respectively, is shown as a full line. The shape of the data is described well. The expected relative contributions of direct (dot-dashed) and resolved (dashed) processes are also shown. The different behaviour of resolved and direct processes can be seen in the figure. The resolved

process dominates over the direct for a wide range of E_T^{jet}. The expected contribution from resolved processes, calculated using Monte Carlo techniques, is about 85%. The shapes using different structure functions for the proton and/or the photon are similar to those presented.

The inclusive jet pseudorapidity (η^{jet}) distribution is sensitive to the type of underlying process, resolved or direct. The distribution is shown in figure 4.9b together with the Monte Carlo simulations from HERWIG. Also shown for the Monte Carlo simulation are the separate contributions from resolved and direct processes. The two contributions are expected to have a different behaviour in pseudorapidity since for resolved processes, the interacting parton coming from the photon takes a fraction of the photon momentum, which is already a fraction of the incoming electron energy. On the other hand, the momentum carried by the interacting parton coming from the proton is usually higher since the initial proton energy is larger. In this case, the two parton centre-of-mass system is boosted in the proton direction. For direct processes, the photon enters the interaction as a whole and its momentum can be comparable to the fraction carried by the interacting parton of the proton. Hence, the boost to the proton direction is usually much smaller for direct processes than in the case of resolved, and the jets are distributed in the central and rear direction.

As can be seen in the figure, the data require a substantial resolved component. Also the data show a rise of the jet rate towards high η^{jet} values which is not well reproduced by the Monte Carlo simulation. It is not clear whether this excess is due to an incorrect description of the proton remnant region or to the choice of parton distributions[1] (see below). In the figure, the Monte Carlo distribution is normalized to the number of jets in the data excluding the highest η^{jet} bin.

The inclusive η^{jet} distribution should have an increased sensitivity to the parton densities in the photon due to the dominance of the resolved contribution and to the fact that the distribution of the fraction of the proton momentum carried by the interacting parton in this type of processes peaks at high values, within a kinematic region which has already been measured with good precision. The data for two choices of the cone radius ($R = 0.7$ and 1.0) are compared to simulations using two different parametrizations for the photon structure function (GRV and LAC1) in figure 4.10a and 4.10b, respectively. The shape of the distribution for $R = 0.7$ is rather well described by the simulation using either GRV or LAC1. It is observed that the comparison between data and Monte Carlo predictions in the range $\eta^{jet} > 1$ is shown to be dependent on the cone radius and the discrepancy mentioned above disappears for $R = 0.7$. Therefore, this discrepancy can be interpreted either as an effect of the low fractional momentum behaviour of the photon parametrizations or of the proton remnant in the most forward region.

Summarizing this section, the results obtained show that the jet rates and the E_T^{jet} distribution are in agreement with QCD based Monte Carlo simulations. Jets were observed with a E_T^{jet} spectrum that reaches values as high as 18 GeV. The η^{jet} distribution is reasonably described (except in the most forward region). All the results obtained are consistent with the dominance of resolved processes. The data show clearly that the specific properties of the jets studied are consistent with the expected features of the hard scattering of the photon (and its constituents) and the partons in the proton. The same conclusions are reached using the PYTHIA Monte Carlo and other parameterizations of the proton (MRSD−) and photon (DG and LAC1) parton distributions.

[1]The Monte Carlo samples have been generated without any tuning of the parameters of the programs.

Chapter 5

Two-jet production: resolved and direct processes

Two main processes are expected to contribute to dijet production in γp interactions: resolved and direct. This chapter is devoted to investigate the appearance of two-jet structure in the data sample, and the identification of the specific mechanisms, resolved and direct processes. The description given by the QCD expectations is investigated. In addition, the distribution of the scattering angle in the centre-of-mass system of the two jets gives information about the spin of the exchanged particle in the hard collision and the jet-jet mass distribution is a very useful tool for studying possible deviations from QCD predictions.

5.1 Analysis of dijet events

Dijet production has been studied by selecting events from the data sample as explained in section 4.4 with *two or more* jets in the accepted rapidity range. In the case of events with more than two jets, the two jets with highest E_T^{jet} are taken as these are expected to most closely reflect the kinematics of the final state partons in LO QCD. The dijet sample for a cone radius of 1 unit, consists of 284 events, which corresponds to $\sim$ 1.4% of the total sample, in agreement with HERWIG which predicts fractions between 0.7 and 2%. Agreement is also found when the cone radius is lowered to 0.7 units.

The dijet invariant mass (M^{jj}) spectrum, shown in figure 5.1a, extends up to values of 40 GeV. Monte Carlo simulations from HERWIG for resolved+direct events with MRSD0 and GRV for the proton and photon parton parametrizations, respectively, are included as well. The simulations (normalized to the data) reproduce the steep fall-off exhibited by the data. The E_T^{jet} spectrum of the dijet sample, which reaches values as high as 18 GeV, is compared to the Monte Carlo simulations from HERWIG in figure 5.1b. The behaviour of the jet pseudorapidity distribution, shown in figure 5.1c, is similar to that of the inclusive jet sample (figure 4.9b). In all cases, the data and Monte Carlo distributions are in reasonable agreement. In particular, the agreement extends up to the highest pseudorapidity bin. Figure 5.1c shows again the need for a large contribution from resolved processes.

Further insight into the mechanism of dijet production is gained by studying the centre-of-mass scattering angle distribution. The $\cos\theta^*$ distribution reflects the angular distribution of the parton-parton scattering processes. This distribution depends on the spin of the exchanged particle in the process. The resolved processes are dominated by the channels in which a spin-1 particle is exchanged (the gluon) and the angular dependence of the cross section is given by

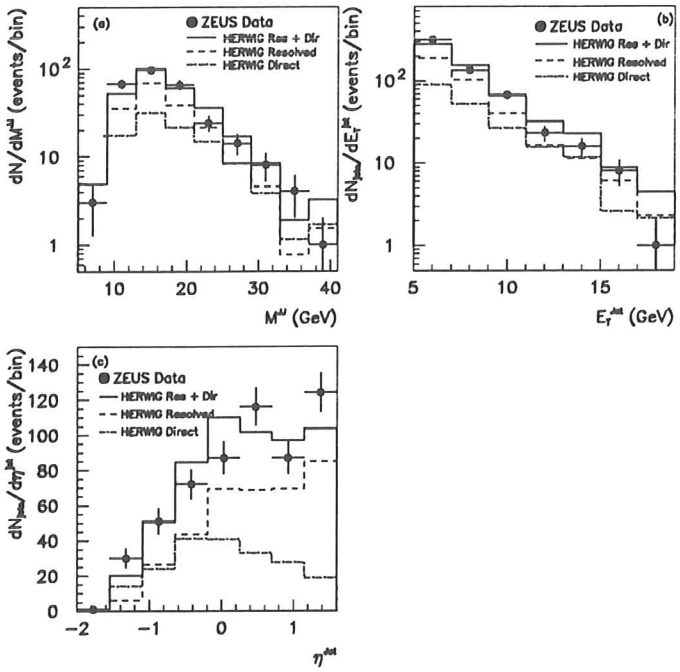

Figure 5.1: Kinematic distributions for events with two or more jets. The Monte Carlo is normalized to the data, and in all cases the relative contributions of the direct and resolved processes, as predicted by the Monte Carlo simulation, are shown. (a) Jet-jet invariant mass for jet pairs. (b) Transverse energy of jets. (c) Pseudorapidity of jets.

$\sim (1 - \cos\theta^*)^{-2}$ [55]. On the other hand, in direct processes the exchanged particle is a quark (spin 1/2) and thus, the angular dependence is given by $\sim (1 - \cos\theta^*)^{-1}$ [55].

The $\cos\theta^*$ variable is computed in the rest frame of the two selected jets with respect to the proton momentum boosted into the same frame. The angular distribution, displayed in figure 5.2a for jet-jet masses above 10, 12, 14 and 16 GeV, shows a rise towards large values of $\cos\theta^*$ (the distributions are normalized to unit area) for the highest mass cuts. This rise becomes more evident as the mass cut increases since the transverse momentum cut on the jets decreases the acceptance for events with low M^{jj} and high $\cos\theta^*$. The drop beyond $\cos\theta^* = 0.8$ is an artifact resulting from the η^{jet} region selected. The HERWIG simulations reproduce the data acceptably. This result, observed for the first time in γp interactions, complements similar results in hadron collider data [56, 57], where the 'Rutherford' scattering between partons have been observed.

Another characteristic of hard scattering photoproduction processes is the fact that the two high-p_T jets arising from the interaction balance their p_T. This can be seen in the transverse plane by looking at the difference in azimuth between the two jets, $\Delta\varphi = |\varphi^{jet_1} - \varphi^{jet_2}|$, since in the longitudinal direction the large boost due to the asymmetric beam configuration is present. Figure 5.2b shows the $\Delta\varphi$ distribution for different E_T^{jet} thresholds (the distributions are normalized to unit area). As can be seen in this figure, the two jets are more back-to-back as the E_T^{jet} increases. This is due to the fact that as E_T^{jet} increases, the jets are more collimated and, consequently, the distribution shrinks to $\Delta\varphi \sim 180°$. The simulations of HERWIG are in agreement with the data.

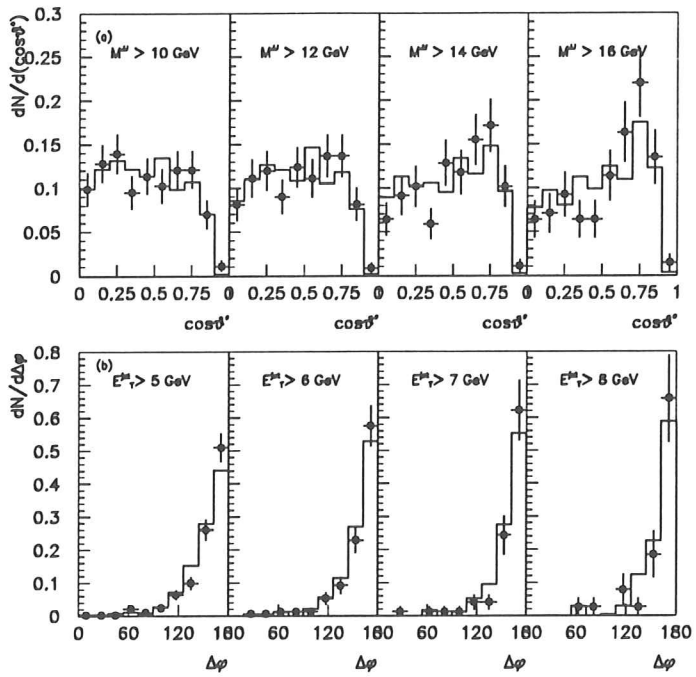

Figure 5.2: (a) $\cos\theta^*$ distribution for M^{jj} >10, 12, 14 and 16 GeV. (b) $\Delta\varphi$ distribution for $E_T^{jet} > 5$, 6, 7 and 8 GeV. The predictions of the HERWIG Monte Carlo for resolved and direct processes (normalized to the data) are presented as well (solid line).

The conclusions to this section are that in a certain fraction of the data sample, two-jet structure is observed. These events are characterized by a back-to-back structure, becoming more collimated as the E_T^{jet} threshold increases. These results give support to the explanation of these events in terms of the hard scattering of the photon and its constituents with the partons in the proton. The QCD predictions for the E_T^{jet} and η^{jet} distributions are in agreement with the data and they show once more the dominance of the resolved processes. The dijet centre-of-mass scattering angle distribution further supports an interpretation in terms of hard parton-parton scattering and the jet-jet mass distribution is well described by the QCD predictions; no significant deviations from QCD are observed.

5.2 Observation of resolved processes

As discussed above, a large contribution from resolved processes is needed to describe the η^{jet} distribution of the data. In addition to the different η^{jet} dependence in resolved and direct processes, the presence of a hadronic system steaming from the fragmentation of the photon remnant in the direction of the incident electron is a unique feature of resolved processes [58].

This has been investigated analyzing the topology of the dijet sample. The correlation between the energy deposited in RCAL and the minimum pseudorapidity of either of the two jets is shown in figure 5.3a for the dijet sample. It is observed that in a subset of the data there is a substantial energy deposit in the RCAL even when both jets appear in the forward region ($\eta_{min} \geq 0$), the nearest jet to the RCAL being at least one unit of rapidity away. This is an unambiguos signature of resolved interactions, where the two jets go forward and the photon

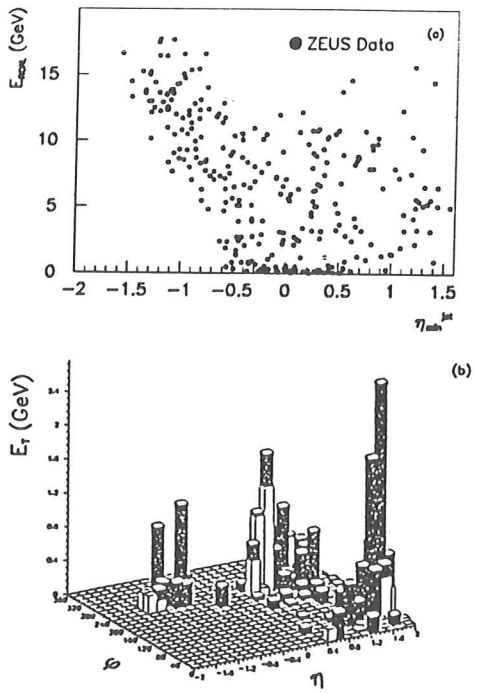

Figure 5.3: (a) Correlation between the energy deposited in the RCAL and the minimum pseudorapidity of the two jets. (b) Transverse energy in the $\eta - \varphi$ plane for an event showing a two-jet structure plus additional activity in the incident electron direction associated with the photon remnant.

remnant emerges approximately in the direction of the incident photon. A resolved candidate is shown in figure 5.3b, where two-jet structure is clearly seen together with a sizeable energy deposit in the electron direction.

By requiring $\eta_{min}^{jet} > 0$ and RCAL energy larger than 5 GeV for the two-jet sample, 61 events are selected. This is in agreement with Monte Carlo calculations which predict 66 ± 8 events in this region.

This observation confirms the presence of resolved processes in the dijet sample, which can now be identified as one of the mechanisms of jet production.

5.3 Observation of direct processes

The jet properties studied until now are consistent with the dominance of resolved processes. The direct processes are expected to contribute to the dijet sample. However, no evidence for the presence of the direct processes can be inferred from the data shapes discussed in the previous sections, as they can be roughly described by the resolved processes alone. In this section we use the selected dijet sample to separate the contributions from direct and resolved processes [14, 41, 42].

Direct processes are characterized by the fact that the photon enters the interaction as a whole, whereas in resolved processes, the photon 'resolves' into partons and one of them, carrying only a fraction of the photon momentum, participates in the interaction. Thus, for resolved processes the fraction of the photon momentum invested in the hard collision is smaller

than 1 and for direct processes it is equal to 1.

In two-to-two parton scattering, the two partons in the final state carry information on the momenta of the incoming partons. The fractional momenta of the incoming partons (x_p and x_γ) can be obtained using the final state partons via the relations [55]:

$$x_p = \frac{p_T}{2E_p}(e^{\eta_1} + e^{\eta_2}) \tag{5.1}$$

$$x_\gamma = \frac{p_T}{2E_\gamma}(e^{-\eta_1} + e^{-\eta_2}) \tag{5.2}$$

where p_T and $\eta_{1,2}$ are the transverse momenta and pseudorapidities of each of the final state partons, respectively, E_p is the proton beam energy and E_γ is the initial photon energy. For resolved processes, $x_\gamma < 1$, and for direct processes, $x_\gamma = 1$. Hence the different behaviour of the x_γ distribution for direct and resolved processes should allow the separation of these two contributions.

In order to calculate the fractional momenta of the incoming partons, the final state partons can be approximated by the two highest E_T final state jets:

$$x_p^{meas} = \frac{1}{2E_p}(E_T^{jet_1} e^{\eta^{jet_1}} + E_T^{jet_2} e^{\eta^{jet_2}}) \tag{5.3}$$

$$x_\gamma^{meas} = \frac{1}{2E_e y_{JB}}(E_T^{jet_1} e^{-\eta^{jet_1}} + E_T^{jet_2} e^{-\eta^{jet_2}}) \tag{5.4}$$

where $E_T^{jet_{1,2}}$ and $\eta^{jet_{1,2}}$ are the transverse energies and pseudorapidities of each jet, respectively, and the energy of the photon has been approximated by $E_\gamma \approx E_e y \approx E_e y_{JB}$.

Use of the formula 5.4 for x_γ has the advantages over using E_γ obtained from the energy of the electron measured in the luminosity monitor (which can be done only for tagged events) that a wide range of photon energies is accessible, and that many systematic uncertainties in the energy measurements in the CAL cancel out. The x_γ^{meas} distribution for direct processes calculated using eq. 5.4 is expected to peak at values slightly smaller than 1 due to the uncertainties coming from the finite size of the cone used in the jet search.

Monte Carlo studies were performed in order to optimize the momentum fraction measurements (see appendix B). From these studies it is found that imposing the requirements $|\eta^{jet_1} - \eta^{jet_2}| \leq 1.5$ and $|\varphi^{jet_1} - \varphi^{jet_2}| > 120°$ improves the x_p^{meas} and x_γ^{meas} resolution [14]. Based on the Monte Carlo studies performed, we reconstruct the initial state parton kinematics with a resolution of 10 to 25%. The number of data events surviving these cuts is 193.

High-p_T dijet production has been used in hadron colliders to extract an effective parton distribution in the proton [56]. Similarly, we can probe the low-x behaviour of the proton and photon parton distributions at HERA. However, in our case, the situation becomes more involved due to the presence of two processes: the direct component which depends solely on the proton parton distributions and the resolved one that depends both on the proton and photon parton distributions. Once both contributions are separated, direct processes constitute a probe of the gluon distribution in the proton due to the dominance of the BGF process at low x_p values (see chapter 6).

First, we study the range of x_p values probed by the selected dijet sample. The distribution of x_p^{meas} is shown in figure 5.4a together with the predictions of the simulation using HERWIG. The x_p^{meas} in the data ranges from 1.6 10^{-3} to 10^{-1}, with a mean value of 1.4 10^{-2}. The Monte Carlo distributions describe well the shape of the data and are insensitive to the choice of parton distributions in the proton. This is due to the fact that the bulk of the range covered by

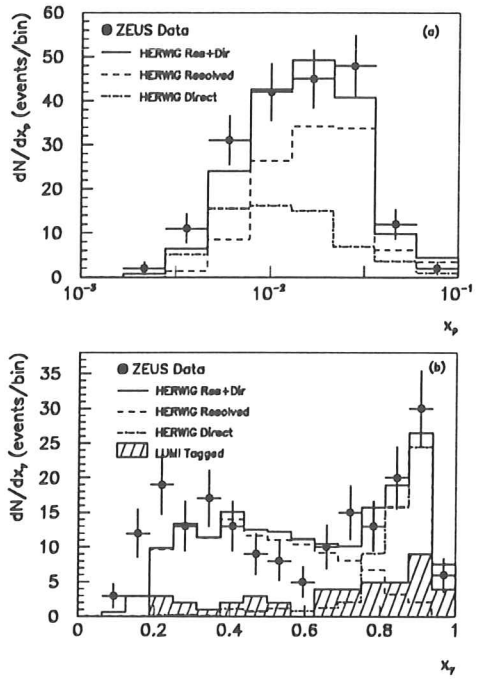

Figure 5.4: Kinematic distributions for events with two or more jets. (a) x_p distribution for the final sample. (b) x_γ distribution for the final sample and the tagged subsample (shaded histogram). For both figures, the Monte Carlo distributions are the result of the fit to the data shown in figure 5.4b (see text).

the present data is in the region where precise measurements of the proton structure function exist, and these are well described by the parameterizations of the proton structure function used here (MRSD0 and MRSD−).

The x_γ^{meas} distribution of the data is shown in figure 5.4b together with the predictions of the simulation using the HERWIG generator. The tagged subsample is shown as a shaded area. The data exhibits a two-peak structure, at low and high x_γ^{meas} values. The behaviour of the tagged subsample is consistent with that of the whole sample.

The predictions of the Monte Carlo simulations of resolved and direct processes have quite different behaviour. The resolved contribution rises towards low x_γ^{meas} values while the direct component peaks sharply at high x_γ^{meas}. It has been studied whether resolved processes alone can account for the peak at the high end. From the Monte Carlo simulation of the resolved processes, the distribution of $(x_\gamma^{meas} - x_\gamma^{gen})$ peaks at around 0.1 (0.2) and has a width of 0.14 (0.22) for HERWIG (PYTHIA), and we conclude that the peak at the high end of the x_γ^{meas} distribution cannot be reproduced from resolved processes by experimental and acceptance effects. The same conclusion is reached for both HERWIG and PYTHIA generators and for all the parton distributions in the proton and in the photon studied. On the other hand, the shape and location of this peak in the data is well described by the direct contribution. The direct processes predict a sharp rise towards high x_γ^{meas} as observed in the data and only a small number of events for $x_\gamma^{meas} < 0.75$. This constitutes an unambiguos evidence for dijet production through the direct process [14, 41, 42].

The relative contribution of the direct process to dijet production was evaluated as follows.

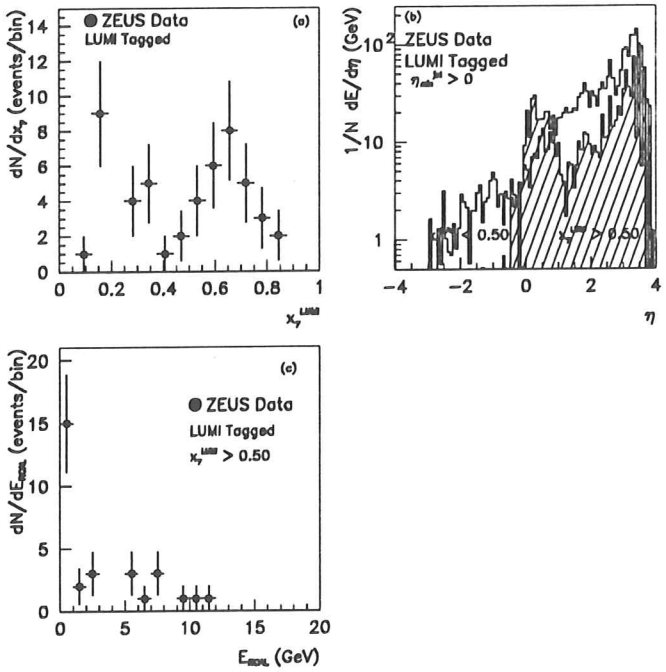

Figure 5.5: (a) x_γ distribution for the tagged subsample calculated using the electron energy measured by the luminosity monitor. (b) Energy flow of the hadronic system for the subset of the dijet data (tagged subsample) with the most backward jet with $\eta^{jet} \geq 0$ and either $x_\gamma \geq 0.50$ (shaded histogram) or $x_\gamma < 0.50$ (white histogram). (c) Distribution of E_{RCAL} for the subset of the dijet tagged sample with $x_\gamma \geq 0.50$.

The shapes of the simulation of resolved and direct processes were added with independent normalizations and fitted to the x_γ^{meas} distribution of the data (see appendix C). The fit, shown as a full line in figure 5.4b, reproduces acceptably the data, although at low x_γ^{meas} values is below the data. This is related to jets in the most forward region, where a discrepancy has already been observed in the η^{jet} distribution. The fit yields a contribution of 65±17 events (34% ± 9% of the selected dijet sample) coming from the direct processes, in good agreement with the predictions of the Monte Carlo simulation (38%).

The subsample of tagged events, which have $Q^2 < 0.02$ GeV^2, is used to check the photoproduction origin of the sample. This subsample also exhibits a peak in the high x_γ^{meas} region, as can be seen in figure 5.4b. For the tagged subsample, an alternative method can be used to estimate x_γ. In this case, E_γ in eq. 5.2 is estimated by using the electron energy measured in the luminosity monitor, $E_\gamma \approx (E_e - E_{eLUMI})$. In order to increase the statistics, the cut on η^{jet} was set to 1.8 in this case; the selected sample contains 50 events. Figure 5.5a shows the x_γ^{LUMI} distribution for these events. As can be seen in the figure, this distribution also presents a peak at high x_γ^{LUMI} values, though in this case, this peak is smeared and shifted towards smaller values than when x_γ was estimated using the CAL. This effect is due to the fact that when x_γ is estimated using the CAL for measuring the jets and the luminosity detector for measuring E_γ, the uncertainties in the energy measurement do no longer cancel.

This subsample of tagged events can be used to investigate the characteristics of the jets and the global shapes of the events. The sample of events with $x_\gamma^{LUMI} \geq 0.5$ is expected to

have an enriched contribution of direct processes. After applying this cut, 28 data events were selected. All the characteristics studied for this subsample exhibit the features expected for direct processes. As an example, the energy flow of the hadronic system for those events with the most backward jet at $\eta^{jet} \geq 0$ and $x_\gamma^{LUMI} \geq 0.5$ is shown in figure 5.5b (shaded histogram). This is to be compared to the same distribution for those events with the same cut on the most backward jet and $x_\gamma^{LUMI} < 0.5$ instead (unshaded histogram). For $\eta^{jet} \geq 0$, the jet activity is restricted to the forward region. The events with $x_\gamma^{LUMI} < 0.5$ exhibit a sizeable hadronic activity in the backward region while the events with $x_\gamma^{LUMI} \geq 0.5$ show little activity in that region. The former are consistent with originating from resolved processes, where the two partons go into the forward region and the photon remnant is in the backward direction. The latter are instead interpreted as emanating from direct processes due to the lack of activity in the backward region. This is a complementary method to the one described in section 5.2 for the observation of resolved processes.

In the region $x_\gamma^{LUMI} \geq 0.5$, a subset of the data shows little activity in the RCAL range. In fact, 15 events of the 28 have an energy deposit in the RCAL less than 1 GeV. The distribution of the energy deposit in the RCAL (E_{RCAL}) for the dijet selected sample is shown in figure 5.5c. The lack of hadronic activity in the backward region, as expected from Monte Carlo simulations of direct processes and as it has been shown in the comparisons of figures 5.5b and 5.5c confirm the observation of dijet production by direct processes [42].

In conclusion, firm evidence for the hard scattering processes responsible for dijet production in γp interactions, resolved and direct, has been given. In a subset of the data, two-jet structure appears together with energy deposit in the direction of the incident electron consistent with the remnant of the photon. This constitutes an unambiguos signal for dijet production through resolved processes. This is further substantiated by the agreement in the jet pseudorapidity distributions of the data and the QCD simulations involving the partonic content of the photon. In addition, the expected dominance of the resolved component is clearly demonstrated. In the dijet sample the distribution of the measured fraction of the photon energy participating in the hard collisions, shows a clear peak at large values consistent with the expectations of the direct process. This distribution allows a separation of the resolved and direct components.

5.4 Determination of direct and resolved dijet cross sections

This section is devoted to the measurement of the cross section for two-jet production. In the previous sections, it was shown that the shapes of the distributions for several jet properties are well described by the HERWIG Monte Carlo, thus we can go further and measure the dijet cross section which can be compared to theoretical calculations. Moreover, the resolved and direct two-jet cross sections are related to the structure functions of the proton and photon in the case of resolved, and to the proton structure function in the case of direct processes. Hence, the cross sections for both contributions were measured separately to check the agreement with the QCD predictions in each case.

The dijet cross section was measured for the kinematic region covered by the data ($0.2 < y < 0.7$) since extrapolation beyond this region implies a dependence on the Monte Carlo simulation which can not be checked against the data.

The clear separation between resolved and direct contributions as explained in the previous section, allowed us to measure the dijet cross sections for each of the two processes separately.

The cross section was calculated for resolved and direct processes via the expressions

$$\sigma(resolved) = \frac{N_{data}^{res}}{\varepsilon^{res}\, L} \tag{5.5}$$

$$\sigma(direct) = \frac{N_{data}^{dir}}{\varepsilon^{dir}\, L} \tag{5.6}$$

where $N_{data}^{res,dir}$ is the number of the data events corresponding to resolved (direct) processes, $\varepsilon^{res,dir}$ is the acceptance correction for resolved (direct) processes, and L is the integrated luminosity.

From the fit of the x_γ^{meas} distribution (figure 5.4b), we obtained a contribution of 65 $\pm$ 17 events from the direct processes. We subtracted this number from the total of 193 events in the data sample, and attributed all the remaining events to resolved interactions. This was done to reduce possible bias due to the poor agreement between the resolved Monte Carlo distribution and the data at low x_γ^{meas}.

The acceptance correction was calculated as follows: from the full Monte Carlo sample, generated over the complete y range, we calculated the number of reconstructed dijet events, N_{rec}, using the full detector simulation and including the experimental trigger conditions and the complete set of selection cuts used in the data analysis. Also from the full Monte Carlo sample, events with a generated y in the range 0.2 - 0.7 were selected. Using the generated momenta of the final state particles, two jets with transverse energies above 5 GeV and pseudorapidities below 1.6 were also required. These cuts select N_{gen} events and define the kinematic region of the quoted cross sections. The ratio N_{rec}/N_{gen} is the experimental dijet acceptance. In this way, the effects of the $|\varphi_1^{jet} - \varphi_2^{jet}|$ and $|\eta_1^{jet} - \eta_2^{jet}|$ cuts are also corrected.

The acceptance is determined separately for the direct and resolved processes (see appendix C). They are about 25% for both the resolved and direct components, and depend only weakly on the Monte Carlo simulation used.

A study of possible systematic errors in the cross section measurements, arising from uncertainties in the fit and the acceptance calculations, has been carried out separately for the resolved and direct contributions. In all cases, the uncertainties in both contributions are similar, and the larger of the two is quoted here. More details on the systematic errors can be found in appendix C. The principal sources of possible errors are:

– different proton and photon parton distributions in the Monte Carlo simulation: $\pm$12%

– different Monte Carlo generators (HERWIG and PYTHIA): $\pm$16%

– the p_{Tmin} cut off value used in the Monte Carlo: $\pm$8%

– different implementations of the jet finding algorithm and treatments of jet merging: $\pm$13%

– uncertainty in the absolute energy scale of the detector: $\pm$17%

– uncertainty in the trigger threshold energies: $\pm$5%

Moreover, a $\pm$5% uncertainty in the luminosity determination [13] was included.

The final results for the dijet cross sections are

$$\sigma_{dijet}(resolved) = 21.1 \pm 5.2\ (\text{stat.}) \pm 5.7\ (\text{syst.})\ \text{nb}$$

for the resolved contribution and

$$\sigma_{dijet}(direct) = 9.4 \pm 2.7\ (\text{stat.}) \pm 2.7\ (\text{syst.})\ \text{nb}$$

for the contribution of the direct processes [14]. The quoted cross sections are the averages of the values obtained with different parton distributions, different Monte Carlo generators and different jet finding procedures and the systematic errors were added in quadrature.

The measured values for the dijet cross sections can now be compared to the LO predictions given by the Monte Carlo simulation. In order to obtain agreement with the measured cross section, the LO predictions for both the resolved and direct contributions have to be scaled up by factors of 1.3 to 1.8, depending upon the Monte Carlo simulation and parton distributions used. A better agreement is expected in the comparisons to NLO calculations since their uncertainties are smaller [2]. However, the ratio of the measured cross sections for resolved and direct processes is consistent with the LO QCD predictions. This is expected due to the fact that NLO corrections to resolved and direct processes should be similar and therefore, the uncertainties largely cancel out in the ratio.

Chapter 6

The gluon content of the proton

The determination of the parton densities in the proton, especially at low values of x, is a very useful information for comparison to theoretical predictions based on QCD calculations, both to test perturbative QCD and to search for new non-perturbative effects. Moreover, these measurements give an empirical description of the proton, essential to understand the parton luminosities in the colliders of the next generation, like LHC. The parton densities are necessary ingredients in calculating production rates for new particles in hadron-hadron interactions. The hadron-hadron cross section at high energies is dominated by gluon-gluon interactions and thus the rates are specially sensitive to the gluon content of the proton, also needed for estimating conventional backgrounds.

Two-jet photoproduction at HERA can be used to extract an effective parton distribution in the proton. Moreover, the two-jet cross section, which is proportional to the partonic density in the proton, is dominated by the BGF process at low x, hence the gluon content of the proton can be estimated by studying a sample of two-jets events enriched in direct processes.

6.1 Application of a cluster algorithm to γp processes

The cone algorithm has been used so far to search for jet structure in our sample due to the characteristics of resolved and direct processes, as explained in section 4.4. Cluster algorithms, which were designed for e^+e^- collisions, take into account all particles measured in the detector to reconstruct the final state, since there are neither remnant nor a soft underlying event. The soft underlying event is present in hadronic collisions and is the result of the interactions between spectator partons in the two colliding hadrons. The application of a cluster algorithm to γp interactions is useful to determine the dependence of the estimated parton distribution in the proton on the jet finding algorithm. It can also be used to compare the results obtained by the cluster and cone algorithms in order to check the consistency between them and consequently, the underlying partonic structure of the jet candidates found. In order to apply it to these type of processes, the contributions from the resolved and direct processes have first to be separated due to the presence of the photon remnant in the case of resolved processes.

The jet clustering algorithm used is described in appendix D. Preliminary studies can be found in ref. [59], where this algorithm was applied to heavy quark events. The application of this algorithm to resolved processes leads to force each event to be reconstructed as a four-jet event: two jet candidates for the final state partons coming from the hard scattering and the other two candidates for the proton and photon remnants, respectively. However, the photon remnant is widely spread in the RCAL and can hardly be reconstructed as a jet. Most of

the time, particles belonging to the photon remnant get clustered into the jets coming from the hard interaction, which in turn get split to fulfill the four-jet condition. On the other hand, an event coming from a direct process must be forced to be reconstructed as a three-jet event, only one remnant (the proton) and two jet candidates for the final state partons, hence the reconstruction is cleaner. In both cases, when jets coming from the hard interaction go into the forward region, the particles from those jets can be mixed up with the fragments of the proton, therefore the pseudorapidity range of these jets in the forward region must be constrained. Hence, this algorithm should be able to reconstruct reliably events coming from direct processes.

Once an enriched sample of direct processes has been isolated, it has to be proven that the cluster algorithm can reconstruct reliably the jets coming from the hard interaction. Then, the cluster and cone algorithms can be applied to the selected sample in order to estimate the gluon content of the proton by two independent methods [60].

The cluster algorithm used in this analysis is able to reconstruct the jets coming from the hard interaction through direct processes as described in appendix E, where a detailed study on Monte Carlo simulations is presented. The quality of the jet reconstruction and the x_p measurement are analyzed there together with a comparison to the cone algorithm which proves that the jet reconstruction and the x_p estimation by both methods are equivalent and supports the fact that the jets reconstructed can be identified with the final state partons.

6.2 The x_p^{meas} distribution

As discussed in section 5.3, the x_γ^{meas} distribution was used to separate the contribution from resolved and direct processes. Once an enriched sample of direct processes is obtained, the cluster and cone algorithms are applied to the selected dijet sample in order to estimate the fraction of the proton momentum carried by the interacting parton and subsequently, the gluon content of the proton.

The method to obtain an enriched sample of direct processes is as follows: the 193 events of the selected dijet sample (see section 5.3) were used to estimate the contributions from direct and resolved processes [14, 41, 42] by exploiting the different behaviour of the two components in the x_γ^{meas} distribution. The sample of events with $x_\gamma^{meas} \geq 0.75$ is expected to be enriched in direct processes. There are 69 dijet events with $x_\gamma^{meas} \geq 0.75$, in agreement with Monte Carlo simulations of direct processes which predict 62$\pm$8 events. The expected background from resolved processes, estimated using Monte Carlo techniques, is $\sim$ 16%. Then, as explained in appendix E, the cluster algorithm was applied to the selected dijet sample in order to obtain a sample reconstructed by both algorithms. Two jets with $E_T^{jet} \geq 5$ GeV and $\eta^{jet} \leq 1.6$ (in addition to the cluster identified as the proton remnant) were required to be reconstructed in each event by the cluster algorithm. The final selected sample of dijet events reconstructed simultaneously by both jet algorithms consists of 67 events. This is the sample that is considered in what follows.

Having selected a sample enriched in direct processes, we proceeded to estimate the fraction of the proton momentum carried by the struck parton. This was done using two independent methods: first, eq. 5.3 was applied to the selected dijet sample reconstructed by the cone algorithm. In the second method, x_p^{meas} was calculated by applying eq. 5.3 to these events, using the jet energies and pseudorapidities reconstructed by the cluster algorithm. As it was proven in appendix E, the two methods give equivalent results.

The same selection procedure as in the data was applied to the Monte Carlo sample of

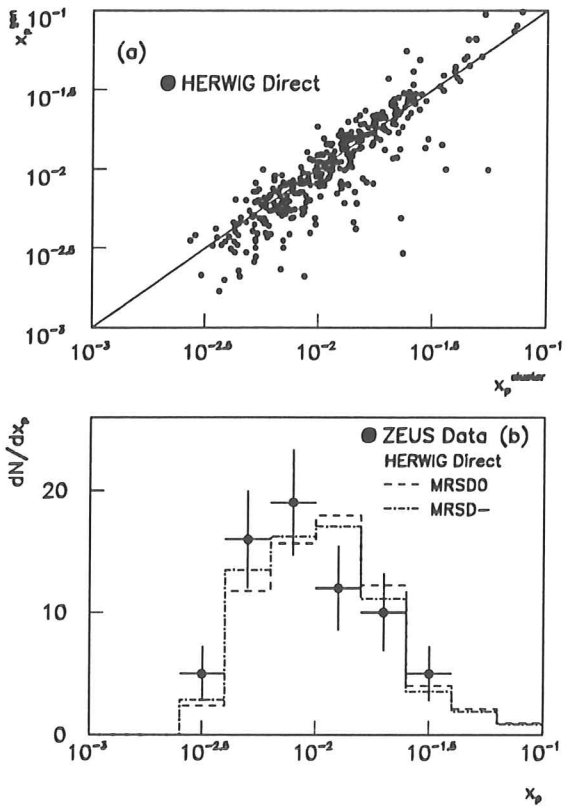

Figure 6.1: (a) Correlation between the reconstructed x_p and the generated value. The x_p value was estimated using two-jet events reconstructed by the cluster algorithm on direct processes simulated by the HERWIG generator which are selected by the cuts defined in the text. (b) x_p distribution for the selected dijet sample ($x_\gamma \geq 0.75$.): data (dots) and the simulation of the HERWIG Monte Carlo of direct processes for MRSD0 (dashed) and MRSD− (dot-dashed). The jets were reconstructed using the cluster algorithm.

direct processes. Figure 6.1a shows the correlation of the x_p^{meas} reconstructed using the cluster algorithm to the generated value for this sample. As can be seen in this figure, the reconstruction is fairly good.

The x_p^{meas} distribution (calculated using the jets reconstructed by the cluster algorithm) for the selected data sample is shown in figure 6.1b together with the Monte Carlo simulation of direct processes for different parton parametrizations of the proton, MRSD0 (dashed line) and MRSD− (dot-dashed line). The Monte Carlo distributions in this figure are normalized to the data and the errors for the data are only statistical. The distribution for the data ranges from 2.5 10^{-3} to 2.5 10^{-2}, with a mean value of 9.3 10^{-3}. The shape of the data is well described by the simulation of direct processes in the kinematic region defined by the cuts.

6.3 An estimation of the gluon distribution in the proton

In order to estimate the gluon content of the proton, we first performed Monte Carlo studies to choose the bins in x_p and to determine the migration effects and systematic errors in those bins.

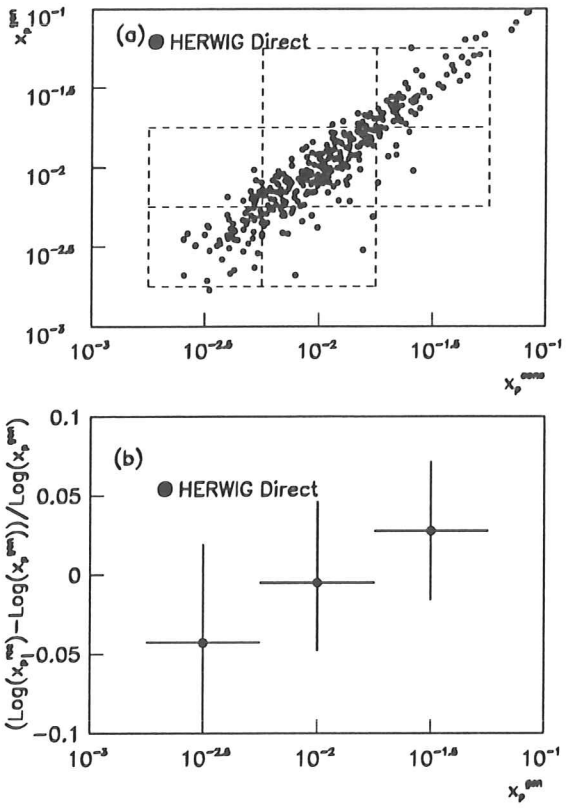

Figure 6.2: (a) Correlation between the reconstructed x_p and the generated value. (b) The relative error, $(\log x_p^{rec} - \log x_p^{gen})/\log x_p^{gen}$, as a function of x_p^{gen}. The x_p value was estimated using two-jet events reconstructed by the cone algorithm on direct processes simulated by the HERWIG generator using the final selected sample for the chosen binning.

Three bins in x_p were chosen to have enough statistics in each bin and to minimize migration effects. Figure 6.2a shows the correlation of x_p^{gen} to x_p^{rec} using the cone algorithm (figure 6.1a shows this correlation for the jets reconstructed using the cluster algorithm). The bins in x_p chosen are sketched in this figure (vertical dashed lines): **Bin 1** is $1.8\ 10^{-3} \leq x_p < 5.6\ 10^{-3}$; **Bin 2** is $5.6\ 10^{-3} \leq x_p < 1.8\ 10^{-2}$; **Bin 3** is $1.8\ 10^{-2} \leq x_p \leq 5.6\ 10^{-2}$. The migration effects can be observed as well (boxes outside the diagonal) and are found to be relatively small (27%, 18% and 22% in each bin, respectively). Figure 6.2b shows the resolution in the x_p reconstruction as a function of x_p^{gen} for the bins chosen; it is found to be better than 10% in the final sample. Similar results are obtained when estimating x_p with the cluster algorithm.

The two-jet cross section at low Q^2 for direct processes can be approximated by the BGF

	Bin 1		Bin 2		Bin 3	
	cone	cluster	cone	cluster	cone	cluster
HERWIG	1.69 (1.61)	1.54 (1.46)	1.08 (1.22)	1.16 (1.31)	0.76 (0.95)	0.73 (0.91)
PYTHIA	1.66 (1.72)	1.72 (1.79)	1.23 (1.44)	1.30 (1.52)	0.74 (0.98)	0.70 (0.89)

Table 6.1: Correction factors for MRSD0 (MRSD−)

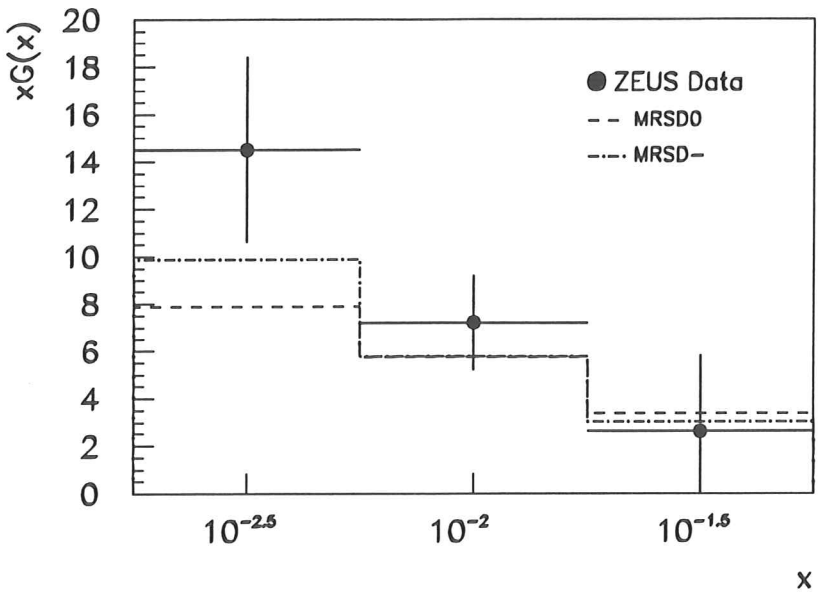

Figure 6.3: $xG(x)$ for data (dots), MRSD0 (dashed) and MRSD− (dot-dashed).

	Bin 1	**Bin 2**	**Bin 3**
$\boldsymbol{xG(x)}$	$14.5 \pm 3.1 \pm 2.5$	$7.2 \pm 1.8 \pm 0.9$	$2.6 \pm 3.2 \pm 0.3$

Table 6.2: $xG^{data}(x)$ (stat. and syst. errors)

contribution [1]

$$\sigma(ep \rightarrow jet + jet + X) \approx \int dy\ dx_p\ d\hat{p}_T^2\ f_{\gamma/e}(y)\ G(x_p)\ \frac{d\hat{\sigma}}{d\hat{p}_T^2}$$

where $f_{\gamma/e}$ is the flux of almost real photons, $\hat{\sigma}$ is the photon-parton cross section and $G(x_p)$ is the gluon density in the proton. Since all other factors are known, $G(x_p)$ at small values of x_p can be extracted from the data. The BGF and QCDC contributions to the final selected sample were estimated by Monte Carlo techniques. It was found that the BGF contribution amounts to 85% of the sample (87%, 85% and 80% in each bin, respectively). Hence, the effective parton distribution in the proton estimated from this sample should be dominated by the gluon contribution.

The unfolding of the acceptance was performed using the Monte Carlo samples. A bin-by-bin correction to the input structure function used in the Monte Carlo simulation was determined and thereby the gluon content of the proton in bin i ($G_i^{data}(x)$) was estimated by [61]

$$G_i^{data}(x) = \frac{N_i^{data}/L^{data}}{N_i^{MC}/L^{MC}} G_i^{MC}(x)$$

where $N_i^{data}(N_i^{MC})$ is the number of data (Monte Carlo) events in bin i, $L^{data}(L^{MC})$ is the luminosity for the data (Monte Carlo) and G_i^{MC} is the input gluon distribution averaged in bin

i. Table 6.1 shows the correction factors applied to G_i^{MC} for each bin estimated using different Monte Carlo generators, jet finding algorithms and parametrizations of the parton distributions in the proton.

The unfolding procedure was checked by taking a sample of events generated by HERWIG and a sample generated by PYTHIA. Each sample in turn was called 'data' and the other 'Monte Carlo' in the application of the procedure to estimate the gluon distribution. It was found that the input gluon distribution was always recovered within errors. This consistency holds for different choices of the input parton parametrizations and for the two jet finding algorithm used.

A study of systematic errors has been carried out taking into account the effects of different jet finding algorithms, parametrizations of the parton densities of the proton and Monte Carlo simulations as principal sources of error. In all cases, the error was calculated by varying one specific source and keeping the other unchanged. The two different jet finding algorithms used (cone and cluster) give a systematic error of 5%, 4%, 4% in each bin, respectively. The estimated uncertainty coming from varying the parametrization of the proton parton densities (MRSD0 and MRSD−) is 13%, 9%, 8%. Different Monte Carlo generators (HERWIG and PYTHIA) give variations of 9%, 7%, 2%. Finally, a 5% uncertainty in the luminosity determination is added.

The final results are shown in table 6.2. The quoted values for the estimated gluon distribution in the proton are the averages of the values obtained with the different jet finding algorithms, different parametrizations of the parton densities and different Monte Carlo generators. The systematic errors have been added in quadrature. Figure 6.3 shows the estimated gluon distribution as a function of x compared to MRSD0 (dashed line) and MRSD− (dot-dashed line). The errors shown in the figure are statistical and systematic added in quadrature. The data show a significant rise towards small values of x, increasing by more than a factor of two from the highest bin to the middle one, and by a factor of two from the middle bin to the lowest one. The data points lie on top of both predictions for the two highest x bins, though it seems to favour a more singular distribution than the one of MRSD− at low x values.

Chapter 7

Inclusive jet differential cross sections at low Q^2

In the previous chapters we have reported the observation of jet production in γp interactions and the analysis that led to the identification of the main processes contributing to hard scattering in the kinematic range studied: resolved and direct. The QCD-based Monte Carlo simulations reproduce reasonably the characteristics of jet production of the data and a first estimation of the gluon content of the proton has been made. In this chapter, we report the study of the partonic content of the photon and perform a test of QCD by measuring the differential cross sections for jet production. The raw data sample used in this analysis corresponds to an integrated luminosity of 550 nb^{-1}, which represents a twentyfold increase with respect to that collected in 1992.

As was explained in section 1.2, differential cross sections $d\sigma/dE_T^{jet}$ and $d\sigma/d\eta^{jet}$ for jet production in the low Q^2 regime are sensitive to the partonic content of the proton and the photon [2, 1, 62]. The dependence on the parton content of the photon can be isolated studying jet production at sufficiently high-E_T to probe the proton structure in a region already covered by previous experiments, but still be in the E_T^{jet} range where the resolved processes are expected to dominate. Before HERA, the hadronic structure of the photon has been experimentally investigated mainly in inclusive $e\gamma$ deep inelastic scattering [28]. LO [25, 29] and NLO [26, 30, 31] fits to these data allowed the extraction of the quark densities in the photon but left the gluon density essentially unconstrained. Recently, measurements of jet cross sections in $\gamma\gamma$ interactions at TRISTAN have been presented [63]. These jet cross sections probed the photon structure function at scales $\hat{Q}_\gamma^2 \sim 6 - 100$ GeV^2 and involved partons in the photon with fractional momenta (x_γ) down to $\sim 10^{-1}$. The comparison to LO QCD predictions showed agreement with the measured cross sections. The measurement of $d\sigma/dE_T^{jet}$ and $d\sigma/d\eta^{jet}$ for inclusive jet production at low-Q^2 at HERA tests the predictions of the parametrizations of the photon parton distributions at higher $\hat{Q}_\gamma^2$ scales and gives information concerning the gluon density at lower x_γ values with respect to existing results. First measurements of these cross sections by the H1 Collaboration [64], performed in a narrower kinematic range than measured presented here, indicated a discrepancy in $d\sigma/d\eta^{jet}$ with respect to LO QCD expectations.

This chapter is devoted to explain the method and give the results obtained for the measurements of $d\sigma/dE_T^{jet}$ and $d\sigma/d\eta^{jet}$ for inclusive jet production in the region of E_T^{jet} (8 GeV $< E_T^{jet} <$ 41 GeV) and η^{jet} ($-1 < \eta^{jet} < 2$). These measurements are compared to LO QCD calculations using different parametrizations for the parton distributions in the photon.

7.1 Data selection criteria and Monte Carlo simulation

During the 1993 running period, physics-based filters were applied at the TLT. The TLT physics filter for hard photoproduction required: a) that the event should have a reconstructed vertex from the tracking chambers with the z-component in the range $|z| < 75$ cm; b) $E^*_{TR} \geq 12$ GeV, where E^*_{TR} is the total transverse energy as measured by the CAL excluding the CAL cells whose polar angles are below 10°; c) $E - p_z \geq 8$ GeV; and d) $p_z/E \leq 0.94$. In the computation of these and subsequent global CAL quantities for every event, the polar angles with respect to the vertex of the interaction as reconstructed using the tracking chambers have been used.

For the purpose of the present analysis, only the events with at least one jet fulfilling the conditions (uncorrected) $E_T^{jet} \geq 6$ GeV and $-1 < \eta^{jet} \leq 2$ were retained at the offline level. A total of 30,366 events satisfied these conditions. The contamination from beam gas interactions, cosmic showers and halo muons was negligible after demanding: a) at least two tracks pointing to the vertex; b) if there are only two tracks pointing to the vertex the opening angle between them (α) should satisfy $\cos\alpha > -0.996$; c) the vertex position along the beam axis in the range -48 cm $< z < 36$ cm; d) less than five tracks not associated with the vertex and compatible with an interaction upstream in the direction of the proton beam; and e) the total missing transverse momentum should be small compared to the total transverse energy, by requiring $\not{P}_T / \sqrt{E_{TR}} < 2$ GeV$^{\frac{1}{2}}$. The last condition also rejects events from DIS charged current interactions where the final state neutrino remains undetected. In order to select a sample of events from low-Q^2 interactions, DIS neutral current candidates were rejected as in previous analyses (see appendix A). After selecting those events with $0.16 < y_{JB} < 0.7$, the final sample consists of 19,485 events containing 24,504 jets. The only significant contamination was from DIS neutral current events with $Q^2 > 4$ GeV^2, which was estimated to be below 2% using Monte Carlo techniques.

For the present analysis, the programs PYTHIA and HERWIG were used to generate photoproduction events via resolved and direct processes. Samples of events were generated with $\hat{p}_T \geq 5$ GeV/c using the LO predictions by GRV for the photon and MRSD− for the proton parton distributions. Samples of events using LAC1 for the photon and MRSD0 for the proton parton densities were also studied. In addition, Monte Carlo samples of events from low-Q^2 diffractive processes were generated. It is expected that these processes contribute to inclusive jet production [65] and experimental evidence has been found at HERA [66]. The final states corresponding to these processes are not accounted for either by PYTHIA or HERWIG and have been simulated using the program POMPYT [67]. In these samples, the cutoff on the transverse momentum was set to $\hat{p}_T \geq 3$ GeV/c in the two-body hard collision. All generated events were passed through detailed detector and trigger simulation programs based on the GEANT package [50]. They were reconstructed using standard ZEUS offline programs and passed through the same analysis chain as the data.

These Monte Carlo samples were used to determine the response of the detector to jets of hadrons and thereby the correction factors to the observed inclusive jet distributions. First, jets of hadrons were searched for in the multihadronic final state (see section 7.2). These jets of hadrons (*had* jets) define the physical objects whose differential cross sections we measured. After these events were passed through the detector simulation, jets were searched for using the CAL cells (*cal* jets). The relationship between the *had* jets and the *cal* jets served to study the resolution of the reconstructed jet variables and to compute the energy corrections to the *cal* jets. Second, the generated events were also used to study the reconstruction of the kinematic variables, the efficiency of the trigger and selection cuts and thus to compute the acceptance

corrections to the observed inclusive jet distributions.

7.2 Jet search and kinematic region

The jet finding algorithm as described in section 4.4 was used to reconstruct jets, both from the final state hadrons and from the energy depositions in the CAL cells in data and generated events. In the present analysis, all CAL cells were included in the jet search and the cone radius R was set to 1 unit. A final cluster of CAL cells was called a jet if E_T(cluster) exceeded 6 GeV, and only jets with η^{jet} in the range $-1 \leq \eta^{jet} \leq 2$ were selected.

The same jet algorithm was applied to the multihadronic final state of the generated events by replacing the CAL cells with the final state particles. All particles with lifetimes larger than 10^{-13} sec and with polar angles between 5° and 175° were considered. The variables associated with the *had* jets are denoted by E_T^{had}, η^{had}, and φ^{had}, whereas the ones for the *cal* jets by E_T^{cal}, η^{cal}, and φ^{cal}.

The reconstruction of the variables of the *had* jets by the *cal* jets was studied using the Monte Carlo samples. The matching between the *cal* and *had* jets was based on the distance in the $\eta - \varphi$ plane: the pair of *had-cal* jets closest in $R = \sqrt{\Delta\eta^2 + \Delta\varphi^2}$ and $R < 1$ was considered to be matched. Unmatched *cal* jets were counted as impurity and unmatched *had* jets as inefficiency. These effects were corrected for in the final cross sections. In the Monte Carlo samples, the inclusive *had* jet and *cal* jet subsamples were thus extracted and the jet variables compared. From this comparison it is concluded that no significant systematic shift in the angular variables η^{cal} (φ^{cal}) with respect to η^{had} (φ^{had}) is present, and that the resolution in η^{cal} is 0.07 units of pseudorapidity and in φ^{cal} is 5°. On the other hand, the transverse energy of the *cal* jet underestimates that of the *had* jets by an average amount of $\sim$ 16%. Details of these studies can be found in appendix F.

The measurement of the inclusive jet differential cross sections are given in the kinematic range $0.2 \leq y \leq 0.85$ and $Q^2 \leq 4$ GeV^2, and refer to jets corrected to the hadron level with $E_T^{had} \geq 8$ GeV and $-1 \leq \eta^{had} \leq 2$. The details of the measurement of this kinematic range in the data can be found in appendix G.

7.3 Jet profiles

The energy corrections to *cal* jets and the correction factors to the observed inclusive jet distributions depend on the characteristics of the *had* jets. Therefore, the characteristics of the jets in the data must be adequately reproduced by the Monte Carlo simulations. This has been checked in the $|\eta^{jet}| \leq 1$ region by comparing the multiplicity distribution and the p_T-spectrum of charged particles within the *cal* jet for data and Monte Carlo. This comparison was extented to charged and neutral particles in the whole η^{jet} range by studying the transverse energy profiles of the *cal* jets.

The characteristics of the *cal* jets in Monte Carlo and data were compared using the tracks reconstructed by the tracking detectors. The tracks were required to be in the ranges $|\eta^{track}| < 1.5$ and $p_T^{track} > 300$ MeV, where p_T^{track} is the transverse momentum of the track with respect to the beam axis. Tracks were associated to a *cal* jet when the extrapolated trajectory hit the CAL within the cone of the *cal* jet. The distribution of the multiplicity of tracks in a *cal* jet and the p_T^{track}-spectrum for tracks in a *cal* jet for the inclusive jet data sample were compared to Monte Carlo samples (see appendix H). The mean value for the multiplicity of tracks in

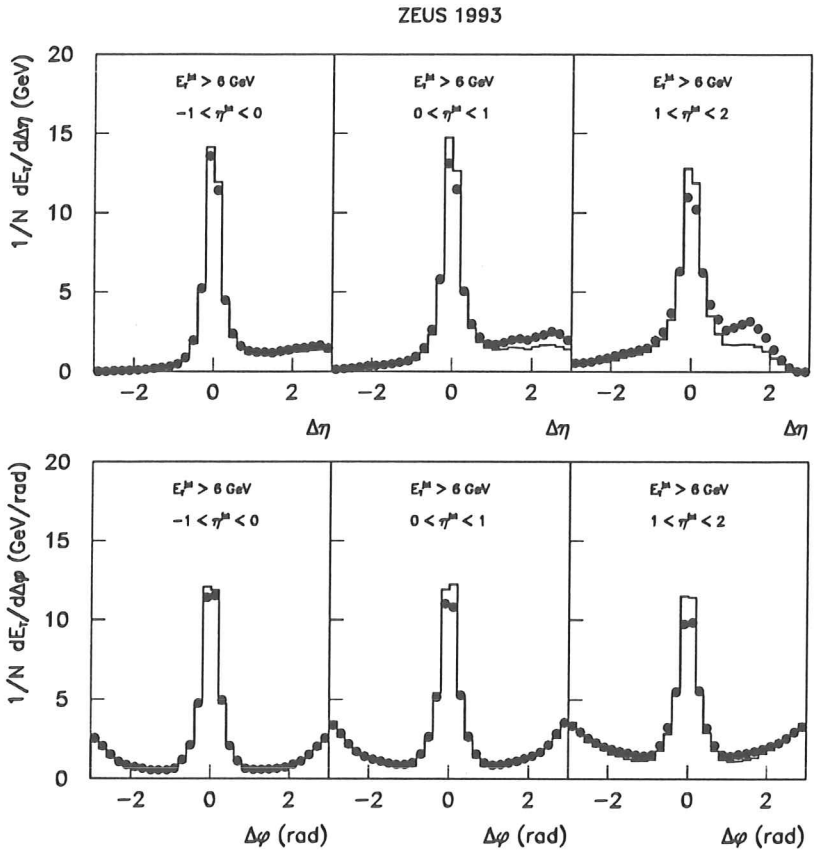

Figure 7.1: Transverse energy profiles as functions of the distance from the jet axis, $\Delta\eta$ (integrated over $|\Delta\varphi| < \pi/2$; top row) and $\Delta\varphi$ (integrated over $|\Delta\eta| < 1$; bottom row), for jets with $E_T^{jet} \geq 6$ GeV and $-1 \leq \eta^{cal} \leq 2$ in the data (black dots) and PYTHIA Monte Carlo samples including resolved plus direct processes (histogram).

a *cal* jet as a function of η^{cal} was also studied. The Monte Carlo describes well all the data distributions studied.

The size and shape of the *cal* jets have been investigated studying the transverse energy profile around the jet axis, $\Delta\eta \equiv \eta^{cell} - \eta^{cal}$ and $\Delta\varphi \equiv \varphi_{cell} - \varphi^{cal}$. The density of transverse energy in the hemisphere of the jet (integrated over $|\Delta\varphi| < \pi/2$) per unit of pseudorapidity, as a function of $\Delta\eta$, is shown in figure 7.1 (top row) for the inclusive jet data sample (black dots) in three η^{cal} ranges: $-1 < \eta^{cal} < 0$, $0 < \eta^{cal} < 1$ and $1 < \eta^{cal} < 2$. In addition, the density of transverse energy integrated over $|\Delta\eta| < 1$, as a function of $\Delta\varphi$, is presented in the bottom row of figure 7.1 for the same sample. The Monte Carlo expectations of PYTHIA including resolved plus direct processes (histogram) are compared to the data in the same figure. The transverse energies have not been corrected for detector effects and the comparison between data and Monte Carlo, which include detector effects, has been made in terms of uncorrected CAL transverse energy densities. The transverse energy profile within the jet and its vicinity for the data is well described by the Monte Carlo expectations in most of the η^{cal} range considered. The decrease of the $\Delta\eta$ distribution seen both in data and Monte Carlo in the region $\Delta\eta > 2$ for the forward jets ($1 < \eta^{cal} < 2$) is a geometrical effect: the most forward edge of the FCAL is at $\eta = 4.3$. These comparisons indicate that, although there is some discrepancy for the forward

jets in the region $\Delta\eta > 1$, the core of the jet (i.e. $|\Delta\eta| < 1$ and $|\Delta\varphi| < \pi/2$) is correctly reproduced by PYTHIA.

7.4 Energy corrections to jets

As it was mentioned in section 7.2, the E_T^{cal} underestimates E_T^{had} by $\sim 16\%$. There are several sources responsible for the energy losses of the *had* jets as measured by the CAL:

i) A *had* jet comprises a bunch of hadrons with very different energies and the compensating response of the CAL to electrons and hadrons is known [33] to differ significantly from 1 when the momentum of the hadron is below 1 GeV.

ii) The dead material in front of the CAL affects the measurement of the energies of the particles by the CAL.

iii) Low-p_T charged particles can be bent by the magnetic field such that they do not reach the CAL or they impinge on the CAL outside of the cone defined by the *had* jet.

iv) The CAL measures little or no energy for μ's or ν's from hadronic decays, resulting in energy losses.

These effects are taken into account in the simulation of the detector which has been used to process the generated events. The correct description of these effects was checked by the following procedure. In the region, $|\eta^{cal}| \leq 1$, the tracks in the *cal* jet were used to determine the total transverse energy carried by the charged particles, E_T^{tracks}. Then, the ratio E_T^{tracks}/E_T^{cal} was formed and the distributions of this ratio in the data and Monte Carlo compared. From this comparison, it has been found that the energy scale of the jets with $|\eta^{jet}| \leq 1$ is correct within $\pm$ 5%. Details of this study can be found in appendix H.

In the forward region, $1 < \eta^{cal} < 2$, the energy scale of the jets was studied using the transverse energy imbalance in dijet events. For this purpose, dijet events with one jet in the central region and the other jet in the forward region were used. The ratio E_T^{cal}(forward jet)/E_T^{cal}(central jet) was formed and the distributions of this ratio in the data and Monte Carlo compared. As the energy scale of the central jet has been checked using the tracks, this ratio is sensitive to differences in energy scale in the forward region between data and Monte Carlo. The results showed that the energy scale of the jets is correct within $\pm$ 5% also in the forward region (see appendix H).

Since the description of the main effects responsible for energy losses in the detector was found to be correct, the Monte Carlo samples were used to determine the transverse energy corrections to the *cal* jets. These corrections (C) have been constructed as a multiplicative factor, $E_T^{corr} = C(E_T^{cal}, \eta^{cal}) \cdot E_T^{cal}$ which when applied to the E_T of the *cal* jet give the 'corrected' transverse energy of the jet, E_T^{corr}. These correction factors have been made both η^{cal} and E_T^{cal} dependent to take into account the variation of the energy losses in these two variables. As mentioned in section 7.2, in the case of η^{cal}, no correction is needed ($\eta^{corr} \approx \eta^{cal}$).

The procedure to obtain the 'map' of transverse energy corrections is explained in appendix I. The corrections computed using the PYTHIA samples are approximately flat as a function of E_T^{cal} for values above 10 GeV and vary, in that region, between 1.08 and 1.18 depending on η^{cal}. They were also calculated for the HERWIG samples and are expected to differ from the transverse energy corrections obtained with PYTHIA due to the fact that the energy losses and, consequently the corrections, depend on the multiplicity and transverse momentum spectrum of the individual hadrons forming the jets. These features depend on the specific fragmentation scheme used and on the flavour content of the final state partons produced by the generator. The consistency between the various 'maps' has been checked applying the 'map' obtained with

a given generator to a sample of events from another generator. The transverse energy of the *had* jet is recovered to a level better than $\pm$ 5% (see appendix I).

7.5 Acceptance corrections to inclusive jet distributions

The samples of Monte Carlo generated events of resolved and direct processes were used to compute the acceptance corrections to the inclusive jet distributions. These corrections factors take into account the efficiency of the trigger, selection criteria and jet reconstruction. The differential jet cross sections are then obtained by applying bin-by-bin corrections to the inclusive jet distributions of the data sample in the variables E_T^{corr} and η^{corr}. For this approach to be valid, the uncorrected inclusive jet distributions in the data must be described by the Monte Carlo simulations. The predictions of the generators PYTHIA and HERWIG for the observed inclusive jet distributions were compared to those of the data for several choices of the parton densities in the photon and proton and for various combinations of the processes involved. A good description of the E_T^{jet} and η^{jet} data distributions by the Monte Carlo is obtained (see appendix J).

The dependence of the correction factors on the specific features of the generators were studied (see appendix K). First, the choice of the parametrizations of the parton densities in the photon and proton was found to change the correction factors by a negligible amount. Second, the correction factors as obtained from resolved processes alone were seen to differ by less than 7% of the values computed using resolved+direct processes. The dependence on the fragmentation scheme was checked comparing the correction factors evaluated with the two generators, HERWIG and PYTHIA, and seen to differ by less than 16%. In this case, the effects of the different fragmentation schemes implemented in PYTHIA and HERWIG were taken into account both in the 'map' of the energy corrections to the *cal* jets and in the bin-by-bin correction factors to the inclusive jet distributions. Finally, the dependence on the environment in which the jets are embedded was studied by using the samples of events generated with the program POMPYT. The POMPYT program simulates final states where there is an absence of colour flow between the hard partons and the spectator partons in the proton, and additional parton radiation is suppressed due the low centre-of-mass energy available in the hard collision. The simulation of non-diffractive (PYTHIA or HERWIG) and diffractive (POMPYT) processes allows to check the dependence of the correction factors on the jet environment. It was found that these effects change the correction factors by less than 10% (see appendix L). In summary, the correction factors depend very weakly on the fragmentation scheme, jet environment and type of process used. The small discrepancies seen were taken into account as contributions to the total systematic uncertainty of the measurements.

7.6 Inclusive jet cross sections

Using the selected data sample of jets and the correction procedure described above, we have measured the differential cross sections for inclusive jet production in the kinematic region defined by $Q^2 \leq 4$ GeV^2 and $0.2 < y < 0.85$. These cross sections, $d\sigma/d\eta^{jet}$ and $d\sigma/dE_T^{jet}$, refer to jets at the hadron level with a cone radius of one unit in η-φ. The cross section $d\sigma/d\eta^{jet}$ has been measured in the η^{jet} range between -1 and 2 integrated over various E_T^{jet} thresholds ($E_T^{jet} \geq 8$, 11 and 17 GeV). The cross section $d\sigma/dE_T^{jet}$ has been measured in the E_T^{jet} range above 8 GeV integrated over $-1 \leq \eta^{jet} \leq 2$.

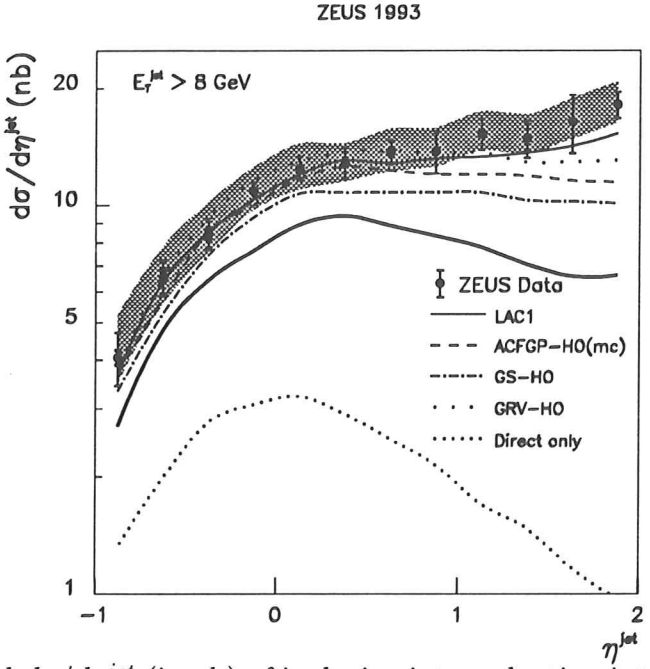

Figure 7.2: Measured $d\sigma/d\eta^{jet}$ (in nb) of inclusive jet production integrated over $E_T^{jet} \geq 8$ GeV (black dots; thick error bars $\equiv$ statistical errors of the data, and thin error bars $\equiv$ statistical and systematic errors —not associated to the energy scale of the jets— added in quadrature; the shaded band shows the uncertainty due to the energy scale of the jets) compared to PYTHIA calculations including direct (fine-dotted line) and resolved plus direct processes for various parametrizations of the photon parton distributions: LAC1 (thin solid line; the calculation with the gluon content of the photon switched off is shown as the thick solid line), GRV-HO (dotted line), GS-HO (dot-dashed line) and ACFGP-HO(mc) (dashed line). In all cases, the MRSD− proton parton distributions have been used.

The results for $d\sigma/d\eta^{jet}$ and $d\sigma/dE_T^{jet}$ are presented in figures 7.2 to 7.4. The η^{jet} and E_T^{jet} bins together with the weighted means of the bins used to present the measurements are given in tables 7.1 and 7.2. The statistical and systematic uncertainties are also shown. A detailed study of the sources contributing to the systematic uncertainties of the measurements was carried out (see appendix M). They were classified in six groups (an average value of the systematic uncertainty for each item is indicated in parentheses):

– Choice of the parton densities in the proton (MRSD− and MRSD0) and photon (GRV and LAC1) for the generation of the PYTHIA Monte Carlo samples ($\sim$ 0.2% for the proton and $\sim$ 3% for the photon).

– Simulation of either resolved or resolved plus direct processes in the generation of the multihadronic final states by PYTHIA ($\sim$ 3%).

– Inclusion of a contribution from hard diffraction processes simulated by POMPYT[1] to the non-diffractive event samples of PYTHIA ($\sim$ 0.5%).

– Use of the HERWIG generator to evaluate the energy corrections to *cal* jets and the correction factors to the observed inclusive jet distributions ($\sim$ 7%).

[1]The PYTHIA and POMPYT samples were added according to the cross sections given by the generators.

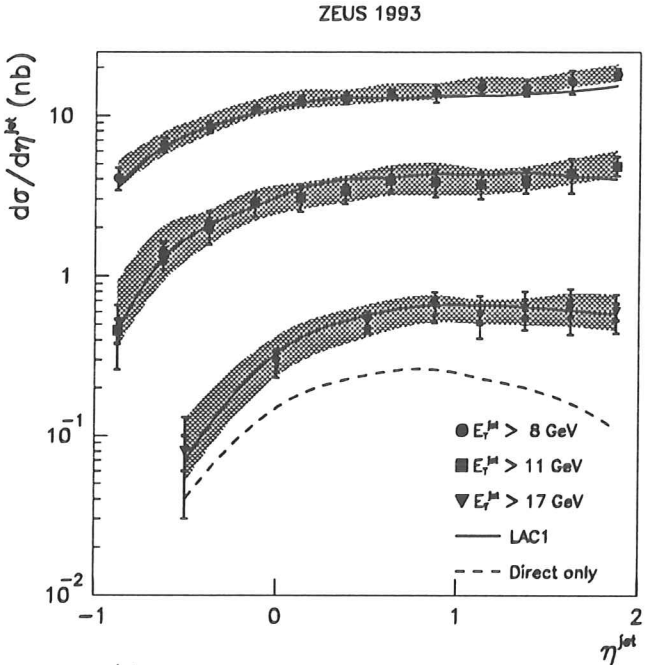

Figure 7.3: Measured $d\sigma/d\eta^{jet}$ (in nb) of inclusive jet production integrated over various E_T^{jet} thresholds (thick error bars $\equiv$ statistical errors of the data, and thin error bars $\equiv$ statistical and systematic errors —not associated to the energy scale of the jets— added in quadrature; the shaded bands show the uncertainty due to the energy scale of the jets) compared to PYTHIA calculations including resolved plus direct processes and using the LAC1 set of photon parton parametrizations (solid lines). The PYTHIA calculation for $E_T^{jet} \geq 17$ GeV including only direct process (dashed line) is also shown. In all cases, the MRSD− set of proton parton distributions has been used.

– Variation of the cuts used to select the data within the ranges allowed by the comparison of Monte Carlo and data distributions of the corresponding variables ($\sim 5\%$).

– Variation of the absolute energy scale of the *cal* jets by $\pm$ 5% to take into account the present understanding of the CAL response to *had* jets ($\sim 20\%$).

The dominant source of systematic error is the uncertainty in the absolute energy scale of the *cal* jets. The statistical errors on the measurements are indicated as thick error bars in figures 7.2 to 7.4. The systematic uncertainties not associated with the energy scale of the jets have been added in quadrature to the statistical errors and are shown as thin error bars. The additional uncertainty due to the energy scale of the jets is shown as a shaded band. We note that the systematic uncertainties have a large degree of correlation from bin to bin. These systematic uncertainties are to be understood as the maximum possible error associated to each data point. In addition, there is an overall normalization uncertainty of 3.3% from the luminosity determination, which is not included.

The measured differential cross sections are compared to the absolute predictions of the PYTHIA generator including resolved plus direct processes with a cutoff $\hat{p}_{Tmin} = 5$ GeV/c. They have been obtained selecting *had* jets using the same jet algorithm as for the data. The Monte Carlo calculations using MRSD− [27] for the proton and either LAC1 [25], GRV-HO

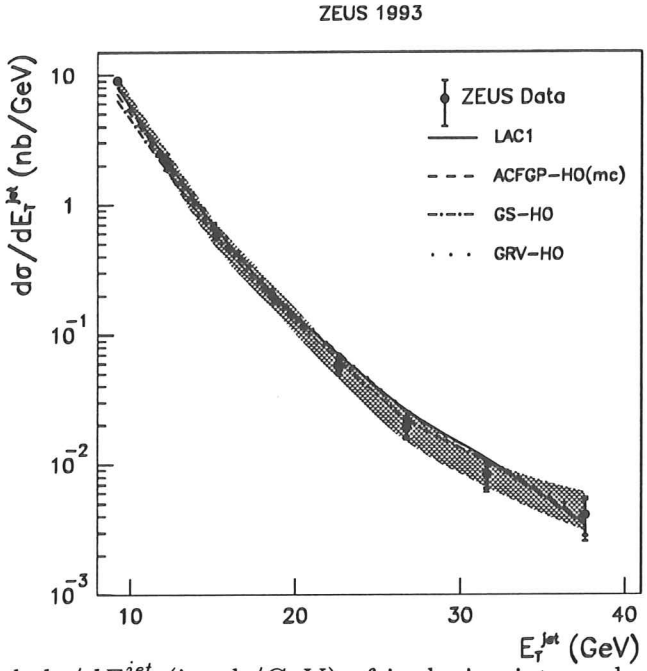

Figure 7.4: Measured $d\sigma/dE_T^{jet}$ (in nb/GeV) of inclusive jet production integrated over $-1 \leq \eta^{jet} \leq 2$ (black dots; thick error bars $\equiv$ statistical errors of the data, and thin error bars $\equiv$ statistical and systematic errors −not associated to the energy scale of the jets− added in quadrature; the shaded band shows the uncertainty due to the energy scale of the jets) compared to PYTHIA calculations including resolved plus direct processes for various parametrizations of the photon parton distributions: LAC1 (solid line), GRV-HO (dotted line), GS-HO (dot-dashed line) and ACFGP-HO(mc) (dashed line). In all cases, the MRSD− proton parton distributions have been used.

[26], GS-HO [30] or ACFGP-HO(mc) [31] for the photon parton distributions are compared to our measurements in figures 7.2 to 7.4. The parton distributions in the proton and the photon are evaluated at the hard scale set by the transverse momentum of the two outgoing partons, $\hat{Q}_p^2 = \hat{Q}_\gamma^2 = \hat{p}_T^2$. These calculations involve the photon parton distributions at $\hat{Q}_\gamma^2$ scales up to $\sim$ 300 GeV^2 and fractional momenta down to $x_\gamma \sim 10^{-2}$. As it was shown in section 1.2, these parametrizations of the photon structure function differ mainly in the gluon content. The LAC1 set contains a larger contribution of gluons at low fractional momenta than the other sets (see figure 1.2). These differences are reflected in the predicted $d\sigma/d\eta^{jet}$ in the forward region. The prediction based on the LAC1 set increases for $\eta^{jet} > 1$ whereas the predictions based on the other sets remain constant in that region (see figure 7.2).

In figure 7.2, the measured η^{jet} distribution integrated over $E_T^{jet} \geq 8$ GeV is compared to the Monte Carlo calculations using the sets of photon parton distributions mentioned above. The Monte Carlo calculation of $d\sigma/d\eta^{jet}$ for the direct processes alone is also shown. It can be seen that the direct processes alone cannot describe the shape of the measured η^{jet}-spectrum and that the resolved processes dominate in the kinematic range studied. The shape and normalization of $d\sigma/d\eta^{jet}$ of the data are well described in the region $-1 < \eta^{jet} < 1$ by the LO QCD calculations of PYTHIA including resolved plus direct processes and using LAC1, GRV-

η^{jet} range	Weighted mean	$d\sigma/d\eta^{jet}$ ±stat.±syst.±syst. E_T^{jet}-scale (in nb)
(-1,-.75)	-0.88	$4.1 \pm 0.2 \pm 0.6\ ^{+1.1}_{-0.6}$
(-.75,-.5)	-0.62	$6.6 \pm 0.2 \pm 0.7\ ^{+1.3}_{-1.0}$
(-.5,-.25)	-0.38	$8.5 \pm 0.3 \pm 0.7\ ^{+1.7}_{-1.0}$
(-.25,0)	-0.12	$10.9 \pm 0.3 \pm 0.5\ ^{+1.6}_{-1.2}$
(0,.25)	0.12	$12.4 \pm 0.3 \pm 0.8\ ^{+1.9}_{-1.5}$
(.25,.5)	0.38	$12.8 \pm 0.3 \pm 1.1\ ^{+1.5}_{-1.4}$
(.5,.75)	0.62	$13.7 \pm 0.3 \pm 0.9\ ^{+2.0}_{-1.5}$
(.75,1)	0.88	$13.8 \pm 0.3 \pm 1.7\ ^{+2.0}_{-1.3}$
(1,1.25)	1.12	$15.2 \pm 0.4 \pm 1.4\ ^{+2.1}_{-1.5}$
(1.25,1.5)	1.38	$14.9 \pm 0.3 \pm 1.6\ ^{+2.2}_{-1.4}$
(1.5,1.75)	1.62	$16.4 \pm 0.4 \pm 2.8\ ^{+2.4}_{-1.6}$
(1.75,2)	1.88	$18.2 \pm 0.4 \pm 1.3\ ^{+2.6}_{-2.0}$

Table 7.1: Measured $d\sigma/d\eta^{jet}$ (in nb) of inclusive jet production integrated over $E_T^{jet} \geq 8$ GeV. The η^{jet} ranges used for the measurements and the weighted means in each bin are shown. The statistical and systematic errors are also indicated. The systematic uncertainties associated to the energy scale of the jets are quoted separately. The overall normalization uncertainty of 3.3% is not included.

HO or ACFGP-HO(mc). The calculation using the set GS-HO can be brought into agreement with the data by an overall normalization factor. This result does not confirm the discrepancy of $d\sigma/d\eta^{jet}$ with respect to LO QCD calculations observed in [64].

The sensitivity of our measurements to the gluon content of the photon predicted by the photon parton distributions studied can be seen in figure 7.2; the Monte Carlo calculation based on the set LAC1 including only the quark contribution (thick solid line) cannot describe the shape of the measured distribution. Using instead the other parametrizations of the photon parton distributions mentioned above in the calculation, leads to the same conclusion. This result shows the relevance of the gluon content of the photon to describe the measured η^{jet} distribution.

In the region $1 < \eta^{jet} < 2$, the measured $d\sigma/d\eta^{jet}$ increases as η^{jet} increases and is reasonably reproduced only by the calculation using the LAC1 set. However, this interpretation of the increase in the data is not unique. As was observed in the jet profiles (see section 7.3), there

E_T^{jet} range (GeV)	Weighted mean (GeV)	$d\sigma/dE_T^{jet} \pm$stat.$\pm$syst.$\pm$syst.E_T^{jet}-scale (in nb/GeV)
(8,11)	9.2	$9.0 \pm 0.1 \pm 0.4\ ^{+1.1}_{-0.7}$
(11,14)	12.2	$2.17 \pm 0.04 \pm 0.31\ ^{+0.51}_{-0.38}$
(14,17)	15.2	$0.59 \pm 0.02 \pm 0.05\ ^{+0.15}_{-0.11}$
(17,21)	18.6	$0.199 \pm 0.011 \pm 0.024\ ^{+0.052}_{-0.040}$
(21,25)	22.6	$0.058 \pm 0.006 \pm 0.007\ ^{+0.014}_{-0.012}$
(25,29)	26.7	$0.0195 \pm 0.0032 \pm 0.0026\ ^{+0.0063}_{-0.0045}$
(29,35)	31.6	$0.0084 \pm 0.0019 \pm 0.0013\ ^{+0.0024}_{-0.0017}$
(35,41)	37.6	$0.0041 \pm 0.0012 \pm 0.0009\ ^{+0.0021}_{-0.0010}$

Table 7.2: Measured $d\sigma/dE_T^{jet}$ (in nb/GeV) of inclusive jet production integrated over $-1 \leq \eta^{jet} \leq 2$. The E_T^{jet} ranges used for the measurements and the weighted means in each bin are shown. The statistical and systematic errors are also indicated. The systematic uncertainties associated to the energy scale of the jets are quoted separately. The overall normalization uncertainty of 3.3% is not included.

is a significant excess of transverse energy density in the data with respect to the Monte Carlo expectations for jets in the region $1 < \eta^{jet} < 2$. This excess is located outside of the jet core and in the forward direction, i.e. $\Delta\eta > 1$. The origin of this extra transverse energy is unclear, but one consequence might be that the transverse energy of very forward jets gets such a contribution that these jets, which otherwise would not have satisfied $E_T^{jet} > 8$ GeV, are included in the measurement of the cross section.

In order to further investigate the region $1 < \eta^{jet} < 2$, the behaviour of the measured $d\sigma/d\eta^{jet}$ as the E_T^{jet} threshold increases ($E_T^{jet} \geq 8$, 11 and 17 GeV) is studied in figure 7.3. The increase of the measured $d\sigma/d\eta^{jet}$ in the very forward region for $E_T^{jet} > 8$ GeV is not present for higher E_T^{jet} thresholds. The Monte Carlo calculations including resolved plus direct processes with the LAC1 set of photon parton distributions describe well the shape and magnitude of the measurements for the two highest E_T^{jet} thresholds over the entire η^{jet} range. The same conclusions are reached when any of the other sets of photon parton distributions are used instead. Thus, the discrepancies between the measurements and the LO QCD predictions (except for LAC1) are restricted to low E_T^{jet} very forward jets.

The comparison of the measured cross section for $E_T^{jet} \geq 17$ GeV to the Monte Carlo calculation of direct processes alone in figure 7.3 shows that even at these E_T^{jet} values the direct processes cannot describe the shape of the measured distribution and that the resolved processes still dominate the production of jets. These results show, for the first time, that resolved processes dominate the production of jets up to at least $E_T^{jet} \sim 17$ GeV. The succesful comparison to the Monte Carlo calculations including resolved plus direct processes shows that

LO QCD gives a good description of the measurements in this new kinematic regime of the structure of the photon. These measurements probe the parton content of the photon at scales as high as $\hat{Q}^2_\gamma \sim 300$ GeV^2.

In figure 7.4, the measured $d\sigma/dE_T^{jet}$ is compared to the Monte Carlo calculations using the various sets of photon parton distributions mentioned above. The predictions using LAC1 or GRV-HO describe the shape and normalization of the measurements in the whole range of E_T^{jet} studied. The predictions using GS-HO or ACFGP-HO(mc) reproduce the data points except for the lowest E_T^{jet} point, where they fall below the data. This discrepancy is related to the one observed in the measured $d\sigma/d\eta^{jet}$ for $E_T^{jet} > 8$ GeV at $\eta^{jet} > 1$, and is not present at higher E_T^{jet} values as was discussed above. This result extends the agreement with LO QCD calculations of $d\sigma/dE_T^{jet}$ reported in [64] up to the highest E_T^{jet} values measured here, $E_T^{jet} = 41$ GeV.

These corrected cross sections can be directly compared to higher order QCD calculations, where a well understood theoretical framework exists [2]. These comparisons, when NLO QCD calculations in our kinematic region become available, might shed light on the understanding of the region of low-E_T^{jet}, very forward jets.

Chapter 8

Summary and Conclusions

The study of high-p_T jets provides a test of QCD. At HERA, ep scattering is dominated by the exchange of almost real photons ($Q^2 \ll 1$ GeV^2). Most of the photoproduction cross section is due to soft processes. However, at the large centre-of-mass energies available, a fraction of the γp interactions is expected to contain high-p_T processes. In lowest-order QCD, these hard processes are of two main types: direct and resolved, which produce two or more partons in the final state giving rise to multi-jet structures. QCD calculations of resolved and direct processes predict that the resolved processes should dominate over the direct in a wide range of jet transverse energy. The direct processes allow the study of the gluon content of the proton, since at small values of the fraction of the proton momentum carried by the interacting parton, the gluon initiated processes dominate the two-jet cross section. The resolved processes are the main source of information on the photon structure function. In particular, the inclusive jet cross sections are sensitive to the gluon content of the photon.

From the data collected during 1992 by the ZEUS detector (~ 30 nb^{-1}), a sample of hard photoproduction events at γp centre-of-mass energies ranging from 130 to 250 GeV was isolated. These events are well balanced in p_T and the transverse energy spectrum exhibits a tail extending up to 50 GeV which can not be explained by soft processes.

The observation of a large transverse energy tail in the data suggests the existence of a component of hard collisions and with the large γp centre-of-mass energies available, the appearance of jet structure should be evident. Indeed, jet structure was observed in a fraction of the sample at rates that are in agreement with QCD-based Monte Carlo simulations. Jets were observed with a E_T^{jet} spectrum that reached values as high as 18 GeV. The η^{jet} distribution is well described in most of the range studied. All the results obtained are consistent with the dominance of resolved processes. The data shows clearly the expected features of hard scattering between the photon (and its constituents) and the partons in the proton.

Clear two-jet structure was observed in our data sample. The two jets were found to be back-to-back and compensated in transverse energy, becoming more collimated as the E_T^{jet} threshold increased. The QCD predictions for the E_T^{jet} and η^{jet} distributions are in agreement with the data and they show once more the dominance of the resolved processes. The dijet centre-of-mass scattering angle distribution supports an interpretation in terms of hard parton-parton scattering, and the jet-jet mass distribution is well described by the QCD predictions; no significant deviations from QCD were observed.

Evidence for the specific hard scattering processes responsible for jet production in γp interactions, resolved and direct, was found. In a subset of the data, two-jet structure appeared together with an energy deposit in the direction of the incident electron consistent with the

remnant of the photon. This constitutes, for the first time, an unambiguous signal for jet production through resolved processes. This was further supported by the agreement in the jet pseudorapidity distributions of the data and the QCD simulations involving the partonic content of the photon. In addition, the expected dominance of the resolved component was clearly demonstrated. In the dijet sample the distribution of the measured fraction of the photon energy participating in the hard collisions, shows a clear peak at large values consistent with the expectations of the direct process. This distribution allowed a separation of the resolved and direct components, and thereby the observation, for the first time, of jet production through direct processes.

Dijet *ep* cross sections involving the exchange of almost real photons in the kinematic region defined by $0.2 \leq y \leq 0.7$ and for jets with transverse energies greater than 5 GeV and pseudorapidities less than 1.6, were measured to be 21.1 $\pm$ 5.2 (stat.) $\pm$ 5.7 (syst.) nb for the resolved and 9.4 $\pm$ 2.7 (stat.) $\pm$ 2.7 (syst.) nb for the direct processes. The ratio of the leading order QCD predictions for these cross sections was found to be in agreement with the measured value.

The gluon content of the proton was probed by studying two-jet events coming from direct interactions. The reconstruction of the fraction of the proton momentum carried by the interacting parton (x_p) was studied and the resolution in this reconstruction was found to be better than 10% for a wide range in x_p. The jet reconstruction and x_p estimation by two different jet finding algorithms (a cone and a cluster algorithm) proved to be equivalent. This supports the fact that the jets reconstructed can be identified with the final state partons.

A data sample enriched in direct processes was selected by exploiting the different behaviour of resolved and direct processes in the measured fraction of the photon energy participating in the hard collision. The x_p distribution exhibited the behaviour expected for direct processes in the kinematic range considered. The Monte Carlo simulation of direct processes, using MRSD0 or MRSD$-$, described well the x_p distribution. The Monte Carlo samples were used to correct the data and a first estimation of the gluon content, $x_p G(x_p)$, was performed. These measurements were compared to the predictions of MRSD0 and MRSD$-$ and found to be in agreement, though at small x_p values, the data seems to favour a more singular distribution than MRSD$-$.

The data collected by ZEUS in 1993, which represented a twentyfold increase with respect to 1992, allowed the measurements of differential cross sections for inclusive jet photoproduction. The jet cross sections corrected for detector effects, $d\sigma/d\eta^{jet}$ and $d\sigma/dE_T^{jet}$, refer to jets at the hadron level with a cone radius of one unit in $\eta - \varphi$ space and were given in the kinematic region defined by $Q^2 \leq 4$ GeV^2 and $0.2 < y < 0.85$. The cross section $d\sigma/d\eta^{jet}$ was measured in the η^{jet} range between -1 and 2 integrated over various E_T^{jet} thresholds ($E_T^{jet} \geq 8$, 11 and 17 GeV). The cross section $d\sigma/dE_T^{jet}$ was measured in the E_T^{jet} range between 8 GeV and 41 GeV integrated over $-1 \leq \eta^{jet} \leq 2$. These measurements probe a new kinematic regime of the partonic structure of the photon, which involves $\hat{Q}_\gamma^2$ scales up to $\sim$ 300 GeV^2 and fractional momenta down to $x_\gamma \sim 10^{-2}$.

Leading logarithm parton shower Monte Carlo calculations using the predictions of currently available parametrizations of the photon parton distributions were compared to the measured jet cross sections. It was shown that resolved processes are essential to describe the measured η^{jet}-spectrum and, from the comparison of the distributions for various E_T^{jet} ranges, the dominance of the resolved processes up to at least $E_T^{jet} \sim 17$ GeV was established for the first time. For $E_T^{jet} > 8$ GeV, the data show an increase in the region $1 < \eta^{jet} < 2$ which is not completely reproduced by the calculations. For higher E_T^{jet} thresholds, the calculations described well the

measured cross sections in the entire η^{jet} range studied. The relevance of the gluon content of the photon, as predicted by the sets of photon parton distributions considered, to describe the shape of the measured η^{jet} distribution was shown. The measured E_T^{jet} cross section exhibited the expected behaviour given by LO QCD up to the highest E_T^{jet} values studied. Except for the region of very forward low-E_T^{jet} jets, these measurements were found to be consistent with QCD in the new kinematic regime of the structure of the photon studied.

The main conclusions drawn from the results presented in this thesis are:

– observation of jets in quasi-real photoproduction interactions in agreement with QCD predictions;

– identification of the specific mechanisms responsible for jet production, resolved and direct processes;

– the resolved and direct processes have been, for the first time, separated;

– observation of the dominance of resolved processes for a wide range of jet transverse energies;

– a first estimation of the gluon content of the proton at small x_p values by using a two-jet sample enriched in direct processes, shows a rapid increase of $x_p G(x_p)$ as x_p decreases;

and finally,

– the measurements of differential jet cross sections are consistent with LO QCD calculations in this new kinematic regime of the photon structure, and show the presence and relevance of the gluon content of the photon.

Bibliography

[1] 'Hadron Structure of High-Energy Photons'; M. Drees and F. Halzen, Phys. Rev. Lett. 61(275)1988;
'Measuring the parton content of the photon at the DESY ep collider HERA'; M. Drees and R. M. Godbole, Phys. Rev. D39(169)1989;
'The hadronic properties of the photon in γp interactions'; G. A. Schuler and T. Sjöstrand, Phys. Lett. B300(169)1993.

[2] 'Jet Photoproduction in $O(\alpha_s^3)$ at HERA'; G. Kramer and S. G. Salesch, Proc. of HERA Workshop, DESY (649) 1991 and DESY 93-10;
'The single jet inclusive cross section at HERA in next-to-leading order QCD'; L. E. Gordon and J. K. Storrow, Phys. Lett. B291(320)1992;
'Jet production at HERA in next-to-leading order QCD'; D. Bodeker, Phys. Lett. B292(164)1992;
'Photoproduction of high p_T jets in next-to-leading order QCD'; M. Greco and A. Vicini, Nucl. Phys. B415(382)1994;
'Inclusive jet production at HERA: next-to-leading order QCD corrections to the resolved and direct photon contribution'; D. Bodeker, G. Kramer and S. G. Salesch, DESY 94-42.

[3] 'Evidence for hard scattering of hadronic constituents of photons in $\gamma\gamma$ collisions at TRISTAN'; AMY Collaboration, R. Tanaka et al, Phys. Lett. B277(215)1992;
Jet production in $\gamma\gamma$ interactions'; PLUTO Collaboration, C. Berger et al, Z Phys. C33(351)1987.

[4] 'High energy photoproduction of large transverse momentum π^0 mesons: a quantitative test of QCD'; NA14 Collaboration, E. Auge et al, Phys. Lett. B168(163)1986; 'Photoproduction of charged hadrons at large transverse momenta'; R. Barate et al, Phys. Lett. B174(458)1986; 'Topological isolation of the deep inelastic QED Compton scattering'; E. Auge et al, Phys. Lett. B182(409)1986;
'Evidence for planar events and a forward double jet structure in deep inelastic muon scattering'; EMC Collaboration, J. J. Aubert et al, Phys. Lett. B100(433)1981; 'Jet production and fragmentation properties in deep inelastic muon scattering'; M. Arneodo et al, Z. Phys. C36(527)1987;
'Inclusive photoproduction of single charged particles at high p_T'; WA69 Collaboration, R. J. Apsimon et al, Z. Phys. C43(63)1989; 'A study of the point like interactions of the photon using energy flows in photoproduction and hadroproduction for incident energies between 65 GeV and 170 GeV'; R. J. Apsimon et al, Z. Phys. C46(35)1990.

[5] 'A Measurement of $\sigma_{tot}(\gamma p)$ at $\sqrt{s}$ = 210 GeV'; ZEUS Collaboration, M. Derrick et al, Phys. Lett. B293(465)1992.

[6] 'Observation of Hard Scattering in Photoproduction at HERA'; ZEUS Collaboration, M. Derrick et al, Phys. Lett. B297(404)1992.

[7] 'Initial Study of Deep Inelastic Scattering with ZEUS at HERA'; ZEUS Collaboration, M. Derrick et al, Phys. Lett. B303(183)1993.

[8] 'Search for Leptoquarks with the ZEUS Detector'; ZEUS Collaboration, M. Derrick et al, Phys. Lett. B306(173)1993.

[9] 'Observation of two-jet production in deep inelastic scattering at HERA'; ZEUS Collaboration, M. Derrick et al, Phys. Lett. B306(158)1993.

[10] 'Hadronic Energy Distributions in Deep-Inelastic Scattering Electron-Proton Scattering'; ZEUS Collaboration, M. Derrick et al, Z.f. Physik, C59(231)1993.

[11] 'Search for Excited Electrons using the ZEUS Detector'; ZEUS Collaboration, M. Derrick et al, Phys. Lett. B316(207)1993.

[12] 'Observation of Events with a Large Rapidity Gap in Deep Inelastic Scattering at HERA'; ZEUS Collaboration, M. Derrick et al, Phys. Lett. B315(481)1993.

[13] 'Measurement of the proton structure function F_2 in ep scattering at HERA'; ZEUS Collaboration, M. Derrick et al, Phys. Lett. B316(412)1993.

[14] 'Observation of Direct Processes in Photoproduction at HERA'; ZEUS Collaboration, M. Derrick et al, Phys. Lett. B322(287)1994.

[15] 'Measurement of Total and Partial Photon Proton Cross Sections at 180 GeV Center of Mass Energy'; ZEUS Collaboration, M. Derrick et al, DESY 94-032 (March 1994), accepted by Z. f. Physik.

[16] 'Observation of Jet Production in Deep Inelastic Scattering with a Large Rapidity Gap at HERA'; ZEUS Collaboration, M. Derrick et al, Phys. Lett. B332(228)1994.

[17] 'Comparison of Energy Flows in Deep Inelastic Scattering With and Without a Large Rapidity Gap'; ZEUS Collaboration, M. Derrick et al, DESY 94-117 (July 1994), submitted to Phys. Lett. B.

[18] 'Measurement of the Proton Structure Function F_2 from the 1993 HERA Data'; ZEUS Collaboration, M. Derrick et al, DESY 94-143 (August 1994), submitted to Z. f. Physik.

[19] 'Corrections to Weizsäcker-Williams approximation for low-Q^2 inelastic ep-scattering'; A. I. Lebedev, Proc. of HERA Workshop, DESY (613) 1991.

[20] 'Photoproduction of large transverse momentum hadronic jets'; J. F. Owens, Phys. Rev. D21(54)1980.

[21] See for example, 'Proton-Antiproton Collider Physics', edited by G. Altarelli and L. DiLella (World Scientific, Singapore, 1989);
for a recent review see 'QCD Tests in Proton-Antiproton Collisions'; J. E. Huth and M. L. Mangano, Annu. Rev. Nucl. Part. Phys. 43(585)1993.

[22] See 'Heavy quark physics at HERA'; A. Ali et al, Proc. of HERA Workshop, DESY (395) 1987.

[23] See 'Hard scattering of (almost) real photons at HERA'; S. J. de Jong et al, Proc. of HERA Workshop, DESY (533) 1987.

[24] 'Hadron production at large transverse momentum and QCD'; B. L. Combridge, J. Kripfganz and J. Ranft, Phys. Lett. B70(234)1977.

[25] 'Parametrization of parton distributions in the photon'; H. Abramowicz, K. Charchula and A. Levy, Phys. Lett. B269(458)1991.

[26] 'Photonic parton distributions'; M. Glück, E. Reya and A. Vogt, Phys. Rev. D46(1973)1992.

[27] 'New information on parton distributions'; A. Martin, W. J. Stirling and R. G. Roberts, Phys. Rev. D47(867)1993.

[28] For a recent review see: 'Some topics in *ep* scattering at HERA: 2 parton distributions in the photon'; H. Abramowicz et al, Int. J. of Mod. Phys. A8(1005)1993.

[29] 'Parametrizations of the photon structure and applications to supersymetric particle production at HERA'; M. Drees and K. Grassie, Z. Phys. C28(451)1985.

[30] 'The parton distribution functions of the photon and the structure function $F_2^\gamma(x, Q^2)$'; L. E. Gordon and J. K. Storrow, Z. Phys C56(307)1992.

[31] 'Higher order QCD corrections to the photoproduction of a direct photon at HERA'; P. Aurenche et al, Z. Phys C56(589)1992.

[32] 'HERA'; R. Brinkmann, DESY HERA 88-03 (1988).

[33] 'The ZEUS Detector', Status Report 1993, ed. U. Holm (February 1993).

[34] 'Construction and beam test of the ZEUS forward and rear calorimeter'; A. Andresen et al, Nucl. Inst. and Meth. A309(101)1991;
'Beam tests of the ZEUS barrel calorimeter'; A. Bernstein et al, Nucl. Inst. and Meth. A336(23)1993.

[35] 'Design and implementation of a high precision readout system for the ZEUS calorimeter'; A. Caldwell et al, Nucl. Inst. and Meth. A321(356)1992.

[36] 'Development of the ZEUS central tracking detector'; C. B. Brooks et al, Nucl. Inst. and Meth. A283(477)1989;
'The design and construction of the ZEUS central tracking detector'; B. Foster et al, Nucl. Inst. and Meth. A338(254)1994.

[37] 'First measurement of HERA luminosity by ZEUS lumi monitor'; J. Andruszków et al, DESY 92-066.

[38] 'Beam test and Monte Carlo studies for the HES and CAL at ZEUS'; C. Glasman, U. Karshon and A. Montag, ZEUS-Note 91-128.

[39] 'Monte Carlo shower terminators for ZEUS inside GEANT311'; G. F. Hartner, ZEUS-Note 88-49;
'ZEUS trigger Monte Carlo program status'; G. F. Hartner and Y. Iga, ZEUS-Note 90-84.

[40] 'Development of electron generated showers in a DU/scintillator calorimeter'; G. Barbagli, ZEUS-Note 87-34.

[41] 'Resolved- and Direct-Photon Interactions in Hard Photoproduction; the Proton and Photon Structure Functions'; C. Glasman, J. Roldan, J. Terron, ZEUS-Note 93-33.

[42] 'Inclusive jet and dijet photoproduction at HERA'; C. Glasman and J. Terron, ZEUS-Note 93-85.

[43] 'Addendum to Measurement of the Dijet Cross-Sections in Resolved and Direct Photoproduction at HERA'; P. Bussey, J. Butterworth, K. Desch, B. Diekmann, R. Feild, L. Feld, C. Glasman, S. Nam, R. Nania, B. Oh, E. Paul, J. Roldan, J. Terron and K. Tokushuku, ZEUS-Note 93-112.

[44] 'Hard Photoproduction with Fall '92 Data'; J. Terron, ZEUS-Note 92-118.

[45] 'Hard Photoproduction Data Selection'; J. Terron, ZEUS-Note 93-29.

[46] 'The LUND Monte Carlo for hadronic processes: PYTHIA version 4.8'; H. U. Bengtsson and T. Sjöstrand, Comp. Phys. Comm. 46(43)1987;
'PYTHIA5.6 and JETSET7.3: physics and manual'; T. Sjöstrand, CERN TH 6488/92.

[47] 'HERWIG: a Monte Carlo event generator for simulating hadronic emission reactions with interfering gluons. Version 5.1'; G. Marchesini et al, Comp. Phys. Comm. 67(465)1992.

[48] 'Parton fragmentation and string dynamics'; B. Andersson et al, Phys. Rep. 97(31)1983.

[49] 'The LUND Monte Carlo for jet fragmentation and e^+e^- physics: JETSET version 6.2'; T. Sjöstrand, Comp. Phys. Comm. 39(347)1986;
'The LUND Monte Carlo for jet fragmentation and e^+e^- physics: JETSET version 6.3'; T. Sjöstrand and M. Bengtsson, Comp. Phys. Comm. 43(367)1987.

[50] 'GEANT3'; R. Brun et al, CERN DD/EE/84-1 (1987).

[51] Method proposed by F. Jacquet and A. Blondel in 'Report from the study group on detectors for charged current events', U. Amaldi et al, Proc. of the Study for an *ep* Facility for Europe, DESY 79/48(377)1979.

[52] 'The Status of the Uranium Calorimeter Reconstruction Software'; P. de Jong, ZEUS-Note 92-19.

[53] 'Observation of jets in high transverse energy events at the CERN $p\bar{p}$ collider'; UA1 Collaboration, G. Arnison et al, Phys. Lett. B123(115)1983.

[54] 'Toward a standardization of jet definitions'; J. Huth et al, Proc. of the 1990 DPF Summer Study on High Energy Physics, Snowmass, Colorado, edited by E.L. Berger (World Scientific, Singapore, 1992) p. 134.

[55] 'Collider Physics'; V. D. Barger and R. J. N. Phillips, Frontier in Physics Science (Volume No. 71), Addision-Wesley (1987).

[56] 'Angular distributions and structure functions from two jet events at the CERN SPS $p\bar{p}$ collider'; UA1 Collaboration, G. Arnison et al, Phys. Lett. B136(294)1984.

[57] 'The dijet angular distribution in $p\bar{p}$ collisions at $\sqrt{s}$ = 1.8 TeV'; CDF Collaboration, F. Abe et al, Phys. Rev. Lett. 69(2896)1992.

[58] 'Identification of the high p_T jet events produced by a resolved photon at HERA and reconstruction of the initial state parton kinematics'; G. D'Agostini and D. Monaldi, Proc. of HERA Workshop, DESY (527) 1992.

[59] 'Gluon Momentum Fraction Measurements in the ZEUS Detector'; Y. Eisenberg, C. Glasman, U. Karshon and A. Montag, ZEUS-Note 92-16;
'Gluon Density Determination from Open Charm Events at HERA'; R. van Woudenberg, F. Ould-Saada, F. Barreiro, J. del Peso, J. F. de Troconiz, Y. Eisenberg, C. Glasman, U. Karshon, A. Montag and S. Egli, DESY 92-002/FTUAM-EP 92-01 and Proc. of the HERA Workshop, DESY (739) 1991.

[60] 'Probing the Gluon Content of the Proton with Two-Jet Photoproduction at ZEUS'; C. Glasman, ZEUS-Note 94-03.

[61] 'A Determination of F_2 with the 1992 Data'; H. Abramowicz et al, ZEUS-Note 93-078;
'J/ψ-production mechanisms and determination of the gluon density at HERA'; H. Jung, G. A. Schuler and J. Terron, Proc. of HERA Workshop, DESY (712) 1992.

[62] 'Photoproduction of large transverse momentum jets at HERA'; W. J. Stirling and Z. Kunszt, Proc. of HERA Workshop, DESY (331) 1987;
'Hadron Structure of High-Energy Photons'; M. Drees and F. Halzen, Phys. Rev. Lett. 61(275)1988.

[63] 'Measurement of the inclusive jet cross section of jets in $\gamma\gamma$ interactions at TRISTAN'; TOPAZ Collaboration, H. Hayashii et al, Phys. Lett. B314(149)1993;
'Measurement of the inclusive jet cross section in $\gamma\gamma$ interactions at TRISTAN'; AMY Collaboration, B. J. Kim et al, Phys. Lett. B325(248)1994.

[64] 'Measurement of inclusive jet cross sections in photoproduction at HERA'; H1 Collaboration, I. Abt et al., Phys. Lett. B314(436)1993.

[65] 'Jet structure in high mass diffractive scattering'; G. Ingelman and P. E. Schlein, Phys. Lett. B152(256)1985;
'Diffractive hard scattering'; E. L. Berger et al, Nucl. Phys. B286(704)1987;
'Hard QCD scatterings in diffractive reactions at HERA'; K. H. Streng, Proc. of HERA Workshop, DESY (365) 1987;
'Unusual high p_T jet events at HERA'; A. Donnachie and P. V. Landshoff, Phys. Lett. B285(172)1992;
'Diffractive hard scattering with a coherent pomeron'; J. C. Collins et al, Phys. Lett. B307(161)1993.

[66] 'Observation of Hard Scattering in Photoproduction Events with a Large Rapidity Gap at HERA'; ZEUS Collaboration, M. Derrick et al, contributed paper to the 27th International Conference on High Energy Physics (ICHEP), Glasgow, Scotland, July 1994;
H1 Collaboration, presented by T. Greenshaw at the 29th Rencontres de Moriond (Méribel les Allues, France, March 1994) and DESY 94-112.

[67] 'Diffractive hard scattering at ep and $p\bar{p}$ colliders'; P. Bruni and G. Ingelman, DESY 93-187, to be publ. in Proc. of the Europhysics Conf., Marseille (1993).

[68] 'Selection of jets in multi-hadron final states produced by e^+e^- annihilation'; K. Lanius, H. E. Roloff, H. Schiller, Z. Phys. C8(251)1981.

[69] 'HERACLES. An event generator for ep interactions at HERA including radiative processes. Version 4.1'; A. Kwiatkowski, H. Spiesberger and H.-J. Möhring, Proc. of HERA Workshop, DESY (1294) 1991.

[70] 'ARIADNE version 4: A program for simulation of QCD cascades implementing the color dipole model'; L. Lönnblad, Comp. Phys. Comm. 71(15)1992.

[71] 'Evidence for a superhard pomeron structure'; UA8 Collab., A. Brandt et al, Phys. Lett. B297(417)1992.

[72] See for example 'Factorization of Hard Processes in QCD', in *Perturbative QCD*, J. C. Collins, D. E. Soper and G. Sterman, edited by A. H. Mueller (World Scientific, 1989).

Appendix A

Details on data selection

Several features distinguish the proton beam gas interactions from the physics events.

Proton beam gas interactions produced upstream of the detector are characterized by a large deposit of energy in the RCAL region, usually larger than the kinematic limit. These can be rejected by imposing the condition $E_{RCAL} \leq 30$ GeV.

The proton beam gas contamination produced near or inside the detector can be seen as a bump in the RCAL timing distribution towards the negative values (figure A.1b). This bump also shows up in the $t_{FCAL} - t_{RCAL}$ distribution on the positive side (figure A.1c). Therefore, stringent cuts on CAL timing were applied: a) rejection of REMC-triggered events with $t_{RCAL} <$ -3 ns and, b) rejection of BEMC-triggered events with $|t_{BCAL}| > 8$ ns. The second requirement was imposed to reject remaining cosmic ray background which affects mainly the BCAL trigger when there is a coincidence of an unpaired bunch passing through the detector with a cosmic event.

Beam gas collisions usually do not have a reconstructed vertex or if they have one it is at large negative z values and not correlated with the event time measured by the FCAL, as opposed to physics events which have good correlation between their z-Vertex and measured FCAL timing. Therefore, only events with a reconstructed vertex were accepted and a cut on the t_{FCAL} vs. z-Vertex correlation was imposed. Figure A.2 shows the z-Vertex distribution for all events with a reconstructed vertex (figure A.2a), for the events with BCN = 9 (figure A.2b), for the REMC triggered events (figure A.2c), and for the BEMC triggered events (figure A.2d). The beam gas contamination to the whole sample can be seen as a bump towards the negative values of the z-Vertex distribution. The contamination to the REMC triggered sample (very small) can be seen as a tail on that same side. The huge contamination to the BEMC triggered sample can be appreciated by comparing the z-Vertex distribution of these events to the one for BCN = 9. Both distributions peak at very negative values, though there are events in the BEMC triggered sample whose vertex is situated around zero.

The correlation between the t_{FCAL} and the z-Vertex is shown in figure A.3 for the whole sample (figure A.3a), the events with BCN = 9 (figure A.3b), the REMC (figure A.3c), and BEMC (figure A.3d) triggered events. As can be seen in figure A.3c, the RCAL triggered subsample is mostly free from beam gas contamination since most of the events exhibit the expected correlation between the z-Vertex and the FCAL timing. The beam gas contamination can be appreciated as an accumulation of events at z-Vertex ~ -100 cm and t_{FCAL} ranging from -4 ns to 4 ns (figure A.3b). This accumulation is very small in the RCAL triggered subsample, but very large in the correlation of the BCAL triggered subsample. Therefore, the following condition was imposed for rejecting beam gas interactions: an event was accepted if

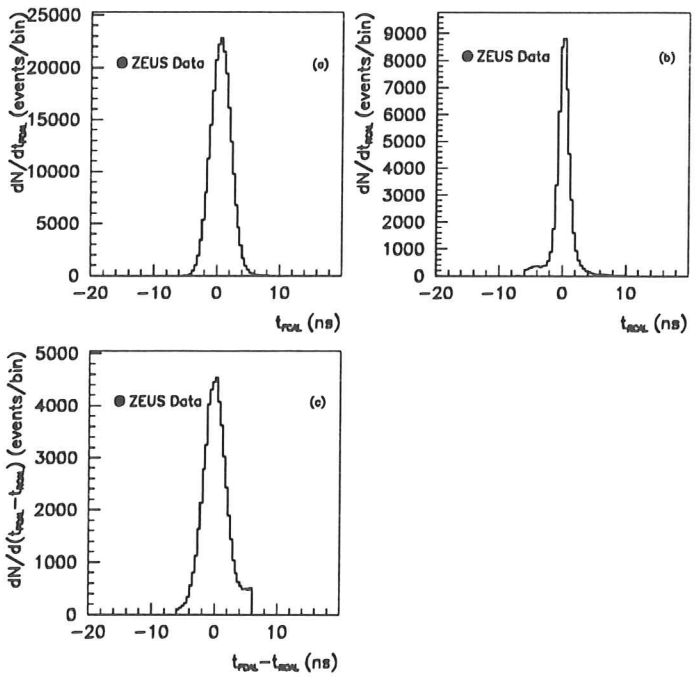

Figure A.1: Calorimeter timing distributions for (a) t_{FCAL}; (b) t_{RCAL}; (c) $t_{FCAL} - t_{RCAL}$.

$|14\ t_{FCAL} + z| < 40$ (straight lines in the figure), with t_{FCAL} in nsec and z in cm.

The variable $y_{JB} = \sum_i (E - p_z)_i/(2E_e)$, where i runs over all CAL cells, is useful to reject beam gas interactions produced inside the detector which leave small energy deposit in the RCAL. For this type of events this variable takes very small values, as opposed to physics events. Figure A.4 shows the transverse energy (E_{TR}) vs. y_{JB} correlation. In this figure, it can be seen that the beam gas interactions populate the region of small y_{JB} and rather large E_{TR}. This can also be observed in figure A.5, where the correlation of y_{JB} to the z-Vertex is presented for the whole sample (figure A.5a), the events with BCN = 9 (figure A.5b) and the REMC (figure A.5c) and BEMC (figure A.5d) triggered events. To eliminate this background, we restricted the sample to those events with $y_{JB} \geq 0.2$.

After applying all the cuts and requirements described above, the contamination from non-ep backgrounds is small. We now look into the physics backgrounds. The main source of physics background to the photoproduction sample is coming from DIS candidates. To remove this contamination, scattered electron candidates were searched for by using the pattern of energy distribution in the CAL [7]. If an electron candidate is found in the CAL, the inelasticity parameter y can be measured using the relation

$$y_e = 1 - \frac{E'_e}{2E_e}(1 - \cos\theta'_e)$$

where E_e (E'_e) denotes the incident (scattered) electron energy and θ'_e is the angle of the scattered electron with respect to the proton beam direction. For DIS events, high energy electrons and a good correlation between y_e and $y_{had} = \sum_i (E - p_z)_i/(2E_e)$, where i runs over all CAL cells excluding the cells belonging to the electron cluster, are expected. However, this correlation should be somewhat degraded due to initial and final state radiation. On the other hand, studies of photoproduction Monte Carlo's reveal that a number of photoproduction

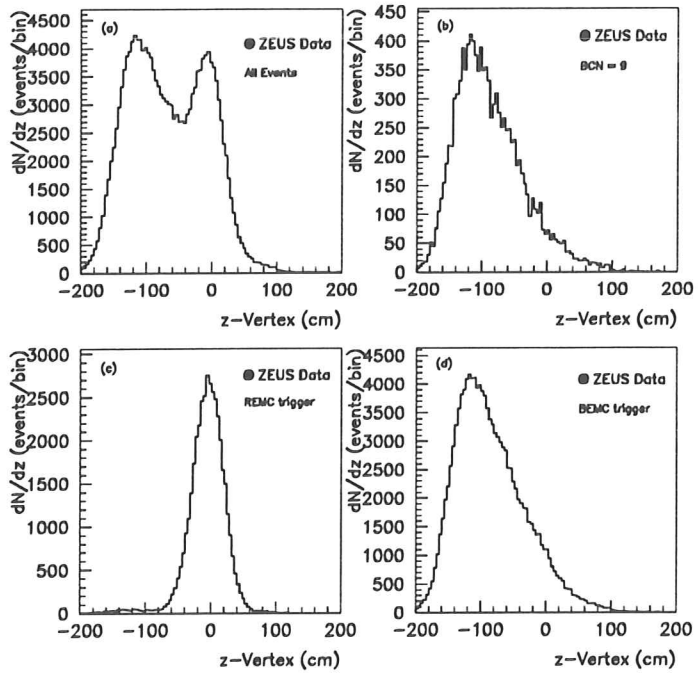

Figure A.2: z-vertex distributions for (a) all events; (b) events with BCN = 9 (c) REMC triggered events; (d) BEMC triggered events.

events have electron candidates found in the CAL. These are mainly photons coming from decays of π^0 and η mesons. Generally, for these candidates the calculated value of y_e is high and they populate the region $y_e \sim 1$, showing no correlation with y_{had}. Figure[1] A.6 shows the correlation of y_e to the variable y_{had}. Two regions can be distinguished in figure A.6: an accumulation of events at low y_e (high energy electron candidates) and an accumulation at high y_e (low energy electron candidates). Therefore, in order to minimize the loss of photoproduction events, an event was rejected only if $y_e \leq 0.7$. A small contamination of DIS interactions where the scattered electron either has low energy or has not been identified could possibly remain. These are rejected by requiring $y_{JB} \leq 0.7$ since $y_{JB} \approx 1$ for DIS events. The whole procedure efficiently removed scattered electrons in the CAL and the resulting sample is thus constrained to Q^2 values below 4 GeV^2.

[1] y_e was set to 1 in this figure for those events without an electron candidate.

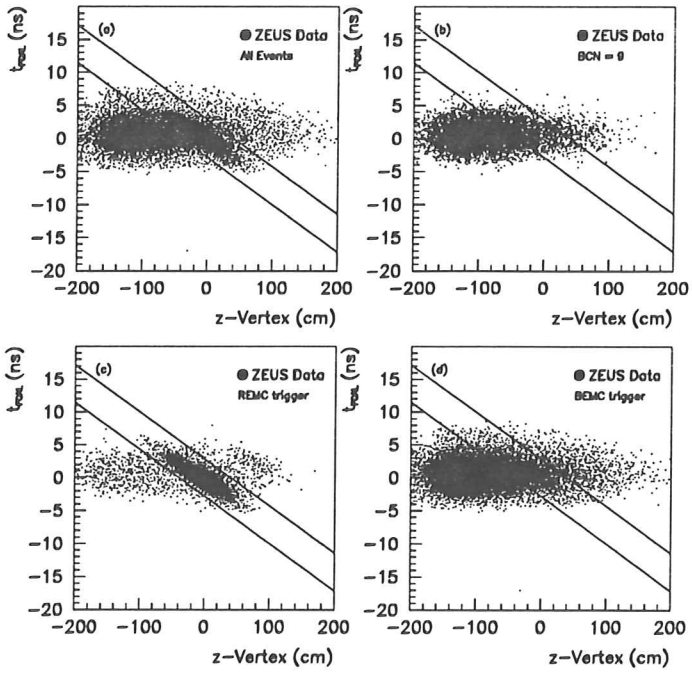

Figure A.3: Correlation between t_{FCAL} and z-vertex for (a) all events; (b) events with BCN = 9; (c) REMC triggered events; (d) BEMC triggered events.

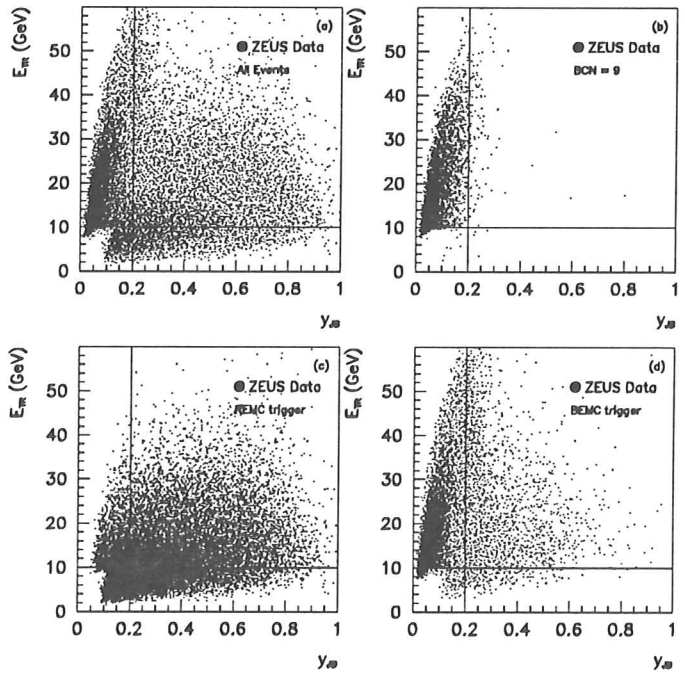

Figure A.4: Correlation between E_{TR} and y_{JB} for (a) all events; (b) events with BCN = 9; (c) REMC triggered events; (d) BEMC triggered events.

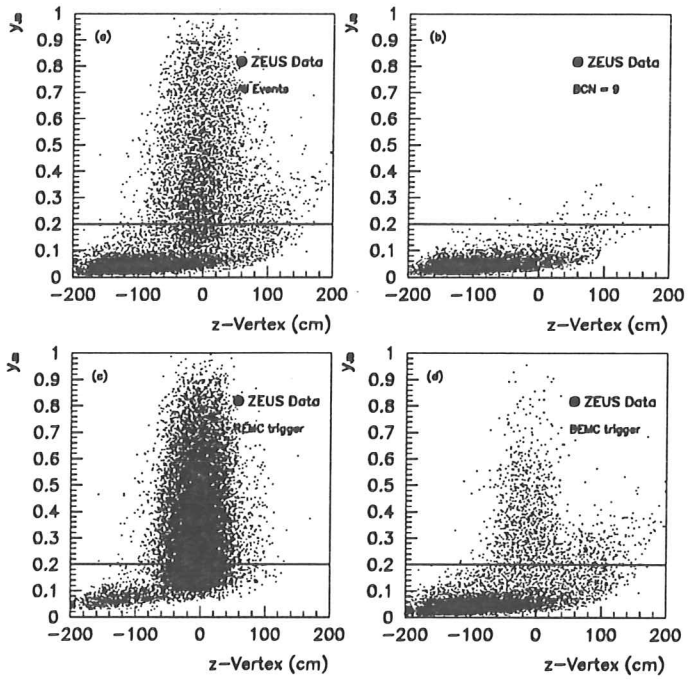

Figure A.5: Correlation between y_{JB} and z-vertex for (a) all events; (b) events with BCN = 9; (c) REMC triggered events; (d) BEMC triggered events.

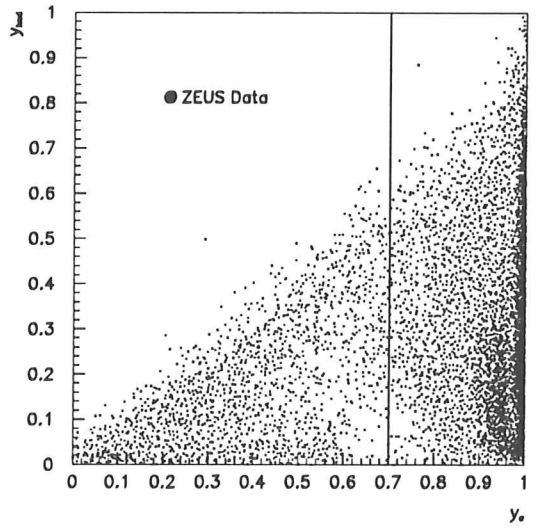

Figure A.6: Correlation between y_{had} and y_e.

Appendix B

Reconstruction of x_p^{meas} and x_γ^{meas}

The error in the x_p^{meas} and x_γ^{meas} reconstruction, calculated from Monte Carlo techniques, is $< \Delta(\log x_p)/\log x_p > = 0.14$ for resolved and -0.02 for direct processes and $< \Delta(x_\gamma) > = 0.17$ for resolved, with resolutions of 12% for x_p-direct, 25% for x_p-resolved and 25% for x_γ-resolved. It was observed that the $< \Delta(x_\gamma) >$ distribution for resolved processes has a long tail coming from those events in which the true x_γ value is small but the measured value is high. This migration into high values of x_γ^{meas} goes into the region where the direct processes are expected. Monte Carlo studies were performed in order to suppress this migration as much as possible. From these studies it is found that imposing the requirements $|\eta^{jet_1} - \eta^{jet_2}| \leq 1.5$ and $|\varphi^{jet_1} - \varphi^{jet_2}| > 120°$ improves the x_γ^{meas} resolution [14].

The distributions of the relative errors in the reconstruction of $\log x_p^{meas}$ and x_γ^{meas} using the HERWIG Monte Carlo simulations of resolved and direct processes are presented in figure B.1 after the cuts described above. As can be seen in this figure, a fairly good reconstruction is achieved. The distributions are centered at around zero ($< \Delta(\log x_p)/\log x_p > = 0.1$ for resolved and -0.01 for direct processes; $< \Delta(x_\gamma) > = 0.1$ for resolved) with resolutions of 9% for x_p-direct, 24% for x_p-resolved and 14% for x_γ-resolved. The correlations between the reconstructed and generated values of $\log x_p$ and x_γ for resolved and direct processes are given in figure B.2. These illustrate the quality of the reconstruction as a function of the generated values. Hence, based on these Monte Carlo studies, we reconstruct the initial state parton kinematics with a resolution of 10 to 25%.

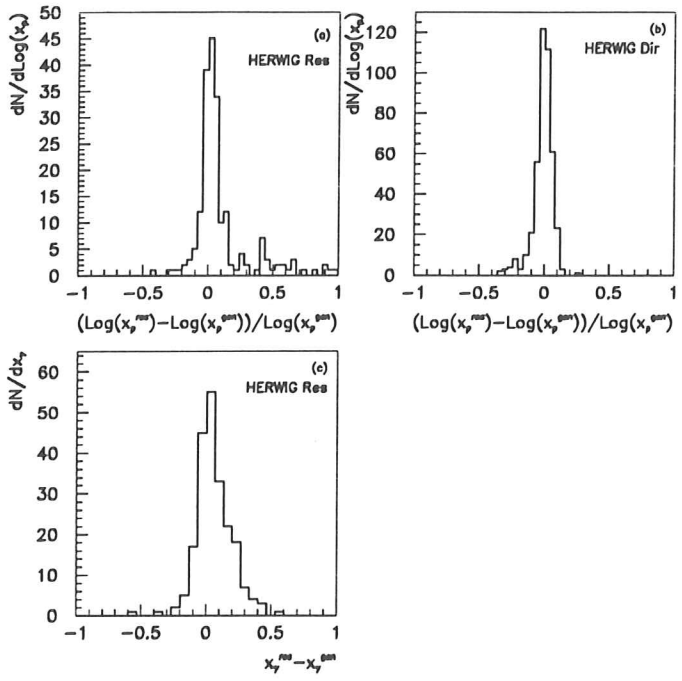

Figure B.1: Resolution of x_p and x_γ.

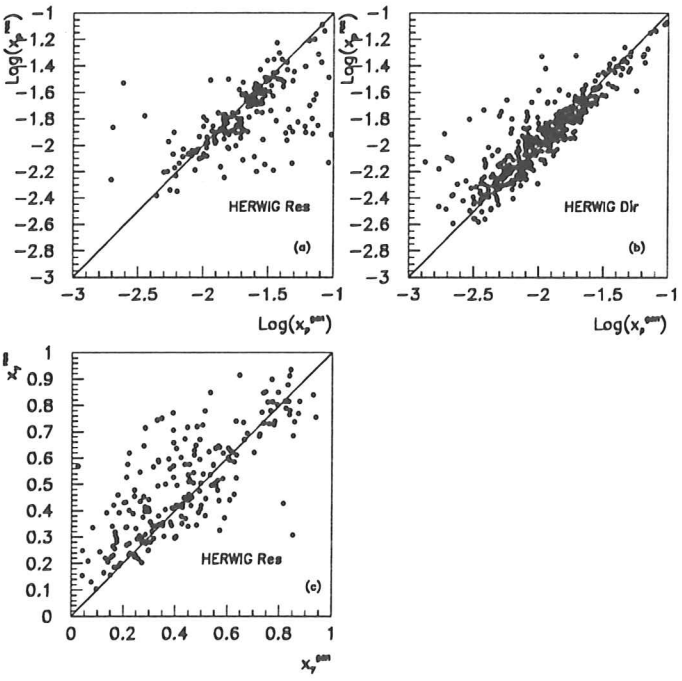

Figure B.2: Correlation between the reconstructed and generated Monte Carlo values of x_p and x_γ.

Appendix C

Dijet cross section evaluation

In this section, the details of the dijet cross section measurement are given. The measurement of these cross sections involves the evaluation of correction factors for the data. These corrections have been computed using Monte Carlo samples of resolved and direct processes. Two main issues were studied:

– Efficiency: only a fraction of the Monte Carlo events with two jets reconstructed at the hadron level survive the trigger, data selection and calorimeter jet reconstruction.

– Migration: Monte Carlo events that are generated outside the kinematic region considered in the cross section evaluation can survive all the selection criteria and be reconstructed inside the kinematic region considered.

The data must be corrected for these effects and different Monte Carlo generators have been used for this purpose (HERWIG and PYTHIA). In order to do this, from each Monte Carlo sample the following two subsamples have been selected and compared:

– Hadron level (class A): the event is required to have $0.2 < y^{true} < 0.7$ and two jets at the hadron level[1] with $E_T^{jet} \geq 5$ GeV, $\eta^{jet} \leq 1.6$.

– Detector level (class B): the event is required to pass the trigger conditions and the data selection, and to have two jets at the calorimeter level with $E_T^{jet} \geq 5$ GeV, $\eta^{jet} \leq 1.6$. In addition the two jets should fulfill the following conditions: $|\varphi^{jet_1} - \varphi^{jet_2}| \geq 120°$ and $|\eta^{jet(1)} - \eta^{jet(2)}| \leq 1.5$.

From the study of these two samples one obtains:

– Number of events that belong to class A: N_{had}

– Number of events that belong simultaneously to classes A and B: N_{good}

– Number of events that belong to class B: N_{det}

Then, the ratio N_{good}/N_{had} gives a measure of the efficiency for reconstructing the jets. On the other hand, the ratio N_{good}/N_{det} is a measure of the purity of the sample reconstructed in the offline analysis. For the resolved processes the efficiency varies between 13% and 16%, depending on the Monte Carlo, while for the direct processes, it is larger and between 18% and 24%. The purity is 55-63% for the resolved processes and gets larger for the direct, 72-82%. The main loss of purity comes from configurations where either the true y is outside the region $0.2 < y^{true} < 0.7$ and the reconstructed y (via the Jacquet-Blondel method) is in the range $0.2 < y_{JB} < 0.7$, or the true jet variables (E_T^{jet}, η^{jet}) are at the limits (but outside) of the regions considered and the reconstructed ones lie in the range under study. The second of these effects is enlarged due to the steep falling behaviour of the E_T^{jet} distribution. The results obtained with different Monte Carlo generators give an estimate of these effects and, consequently, the

[1] The cone algorithm was applied to the final state hadrons

size of their contribution to the total systematic error of the cross sections.

Finally, in order to compute the cross sections for the total dijet production and the resolved and direct contributions, a two-parameter fit is performed on the x_γ^{meas} distribution of the data. In order to obtain the number of resolved and direct events seen in the data, we divide the x_γ^{meas} range (0,1) in 16 bins (the first bin is not further considered as there is no event in this bin in the data nor in the Monte Carlo; thus 15 bins are actually used) and the data distribution is fitted with the resolved and direct Monte Carlo distributions. We minimize the quantity:

$$\chi^2 = \Sigma_{i=2,16} \frac{(n_i^{data} - n_i^{MC})^2}{n_i^{data} + N_{data}^2 (n_i^{dir}/N_{dir}^2 + n_i^{res}/N_{res}^2)}$$

where

- n_i^{data}: number of events (data) in bin i
- n_i^{dir}: number of events (MC direct) in bin i
- n_i^{res}: number of events (MC resolved) in bin i
- N_{data}: total number of events (data)
- N_{dir}: total number of events (MC direct)
- N_{res}: total number of events (MC resolved)
- n_i^{MC}: $= P_{dir}\ n_i^{dir} + P_{res}\ n_i^{res}$
- P_{dir}, P_{res}: free parameters of the fit

The expression in the denominator of χ^2 takes into account the statistical fluctuations in the data and in the Monte Carlo samples. The fitting procedure yields the best values for the free parameters, P_{dir}^* and P_{res}^*, out of which we compute the number of events coming from direct processes present in the data:

$$N_{dir}^* = \Sigma_{i=2,16} P_{dir}^*\ n_i^{dir}$$

The number of events coming from the resolved process is taken to be $N_{res}^* = N_{data} - N_{dir}^*$, as discussed in section 5.4. Once the numbers of events have been obtained, they are corrected for the effects mentioned above to get the cross sections:

- Direct cross section: $\sigma(direct) = N_{dir}^* \times$ Purity$_{dir}$ /(Efficiency$_{dir}$ $\times$ Luminosity)
- Resolved cross section: $\sigma(resolved) = N_{res}^* \times$ Purity$_{res}$ / (Efficiency$_{res}$ $\times$ Luminosity)
- Total cross section: $\sigma(total) = \sigma(direct) + \sigma(resolved)$

Sources of possible systematic errors in the cross sections measured using this procedure were studied. The main sources are given by the Monte Carlo generator used, the proton and photon parton parametrization used in the Monte Carlo, the implementation of the jet finding algorithm and the energy scale in the Monte Carlo. Besides, a study has been performed to check the effect of an improper simulation of the trigger. The precise relationship between the energy scale in the Monte Carlo simulation and in the data was investigated as a possible source of systematic error. A crucial parameter in the Monte Carlo programs that we used is the cutoff in the transverse momentum of the two produced final state partons p_{tmin} and the effect of this parameter on the cross section was studied as a source of systematic errors. Table C.1 summarizes our estimation of the systematic uncertainties on the cross section measurements. The uncertainties given in section 5.4 are the values as given here. The final quoted systematic error is the quadratic sum of the different contributions.

	Total	Direct	Resolved
Different MCs	13%	8%	16%
Trigger Conditions	5%	5%	5%
Calorimeter Energy scale	12%	17%	12%
Parton distributions	9%	12%	11%
Jet Algorithm	11%	13%	9%
Luminosity	5%	5%	5%
Vertex determination	2%	2%	2%
MC $\hat{p}_T^{min}$	8%	8%	8%
Total	25%	28%	27%

Table C.1: Summary of systematic uncertainties.

Appendix D

The cluster algorithm

The method is based on the complete linkage hierarchical clustering algorithm [68]. In the first step of the algorithm, "similarities" between all possible pairs of input objects are defined. The similarity of two objects i and j is described by a numerical value d_{ij} which must obey the following conditions:

- $0 \leq d_{ij} \leq 1$
- $d_{ij} = d_{ji}$
- $d_{ij} = \begin{cases} 1 & \text{for identical objects} \\ 0 & \text{for extremely different objects} \end{cases}$

After the similarities between all possible pairs are calculated, they are stored into a "similarity matrix", which is triangular and at this stage contains $\frac{N(N-1)}{2}$ independent coefficients, where N is the number of clusters. Next, the most similar (largest d_{ij}) clusters i and j are fused to form a new cluster called k. The entries from clusters i and j are then removed from the similarity matrix and they are no longer considered as independent clusters. In the next step, the new object k is defined as the sum of i and j and its similarity to all the remaining groups is calculated and added to the matrix. Now this matrix contains $\frac{(N-1)(N-2)}{2}$ elements.

After this is done, a new loop begins, looking for the most similar clusters of the remaining ones, fusing them, removing their entries from the similarity matrix and recalculating the similarities to all remaining particles for the new cluster. At each step, the similarity matrix dimension is reduced due to the removal of the entries belonging to the groups that are clustered.

This process continues until all the input objects are clustered. Usually, final states in high-p_T interactions consist of more than one jet. Therefore, one must combine the observed hadrons until the original number of jets is recovered. Cluster algorithms do not give the number of jets in the event as an output, therefore this value must be found by other methods. In general, jet finding algorithms stop the clustering at a predefined cutoff value and the number of clusters may change from event to event. In hadron induced interactions, the presence of spectator jets and the ensuing color flow between hard jets and the spectator ones, makes the assignment of particles to jets more difficult than in the case of the much cleaner e^+e^- events. In the case of HERA, the extra Lorentz boost due to the very asymmetric collision and the losses of particles into the beam pipe are sources of further complications. In this particular approach the input objects are forced to be combined into a predefined number of clusters.

Appendix E

Monte Carlo studies: cluster and cone algorithms

In order to estimate the quality of the jets reconstructed with the cluster algorithm, we have used events coming from direct processes generated by the HERWIG and PYTHIA Monte Carlo programs with a lower cutoff of $\hat{p}_{Tmin} = 2.5$ GeV. The parton densities in the proton were parametrized by using the MRSD0 and MRSD− sets. Events coming from resolved processes were also generated for background estimations. The selection criteria described in section 4.1 were applied to these Monte Carlo samples.

The clustering procedure was applied to these Monte Carlo samples using as input objects the EMC and HAC CAL cells. CAL cells with EMC (HAC) energy below 60 MeV (110 MeV) were excluded from the jet analysis.

The similarity definition used in this analysis is proportional to the relative transverse momentum of the two clusters i and j [49],

$$d_{ij} = \frac{\sqrt{2}p_i p_j}{p_i + p_j}\sqrt{(1 - \cos\theta_{ij})}$$

where θ_{ij} is the angle between the clusters i and j and $p_{i,j}$ are the momenta of those clusters. This similarity definition was properly normalized so that it fulfills the conditions listed in appendix D.

Three jets were reconstructed in each event. The remnants of the proton are expected to be predominantly at small angles around the proton beam direction, hence the cluster with a minimum angle with respect to the proton beam direction was identified as the proton remnant candidate and then removed. In order to study only those two-jet events with high transverse momenta and to reject those events in which the jets go in the forward direction, close to the proton remnant, the cuts applied in the previous analysis ($E_T^{jet} > 5$ GeV and $\eta^{jet} < 1.6$) were found to work in this case as well. Hence, an event was accepted if both remaining jet candidates have $E_T^{jet} > 5$ GeV and $\eta^{jet} < 1.6$.

For the events in which there are two reconstructed jets inside the kinematic region defined above, the energy, angular and transverse momentum resolutions of those jets were compared to the generated final state partons. The distributions are centered at around zero ($< \Delta E/E > \sim$ 0.06, $< \Delta\varphi/\varphi > \sim$ 0.01, $< \Delta\eta > \sim$ 0.26, $< \Delta E_T/E_T > \sim$ 0.30) with resolutions of the order of 10-40%. Figure E.1 shows the energy, angular and transverse momentum correlations of the reconstructed jets to the corresponding values for the generated final state partons (the assignment was done by choosing the closest parton in angular space to a given reconstructed

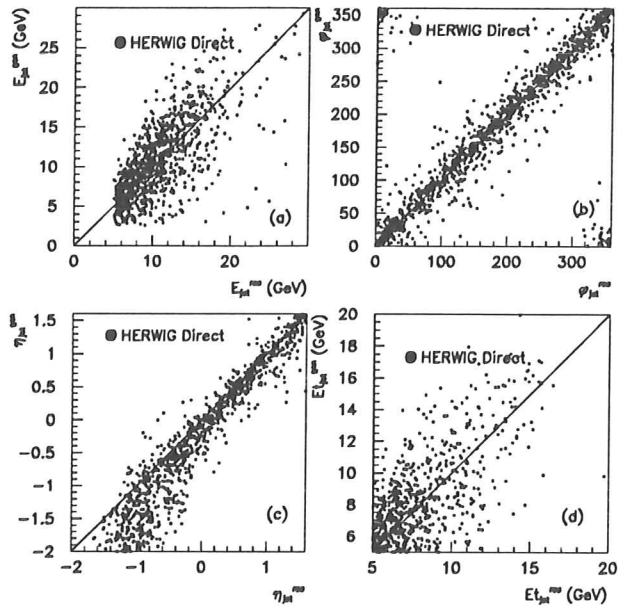

Figure E.1: (a) Correlation between the reconstructed jet E_{jet}^{rec} and the generated parton E_{jet}^{gen}. (b) Correlation between the reconstructed jet φ_{jet}^{rec} and the generated parton φ_{jet}^{gen}. (c) Correlation between the reconstructed jet η_{jet}^{rec} and the generated parton η_{jet}^{gen}. (d) Correlation between the reconstructed jet E_{Tjet}^{rec} and the generated parton E_{Tjet}^{gen}. These correlations correspond to events coming from direct processes simulated by the HERWIG generator, in which two jets were reconstructed inside the kinematic region defined in the text by using the cluster algorithm. The assignment of partons to reconstructed jets is performed by comparing the closest pair in angular space.

jet in each event). As can be seen in this figure, the quality of the reconstructed variables of the jets is within reasonable limits for the accuracy needed in this analysis.

In order to calculate the fraction of the proton momentum carried by the struck parton, the jet energies and momenta reconstructed by this algorithm were used in eq. 5.3. The quality of the reconstruction of x_p has been tested by comparing the generated x_p (x_p^{gen}) to the value obtained from eq. 5.3 (x_p^{rec}) using the E_T^{jet} and η^{jet} of the two reconstructed jets. The $(\log x_p^{rec} - \log x_p^{gen})/\log x_p^{gen}$ distribution is centered at -0.02 with a resolution of 11%. The correlation between the reconstructed and generated values of x_p is shown in figure E.2a, which illustrates the quality of the reconstruction. The relative error in the x_p reconstruction, $(\log x_p^{rec} - \log x_p^{gen})/\log x_p^{gen}$, as a function of x_p^{gen} is presented in figure E.2b. It shows that the initial state parton kinematics can be reconstructed with an error below 20% for x_p^{gen} values above 3.2 10^{-3}.

In order to check that the observed clusters are not an artifact of the clustering procedure, a jet reconstruction by an independent method was performed and the reconstructed jet variables compared. Jet structure was searched for in the same Monte Carlo sample using the cone algorithm as described in section 4.4. The cone radius was set to 1 unit. The same cuts as in the case of the cluster algorithm were applied in order to define a jet, i.e. $E_T^{jet} > 5$ GeV and $\eta^{jet} < 1.6$. In order to compare to the jets reconstructed by the cluster algorithm, events with *only* two jet candidates within the kinematic region defined were selected. The cone algorithm

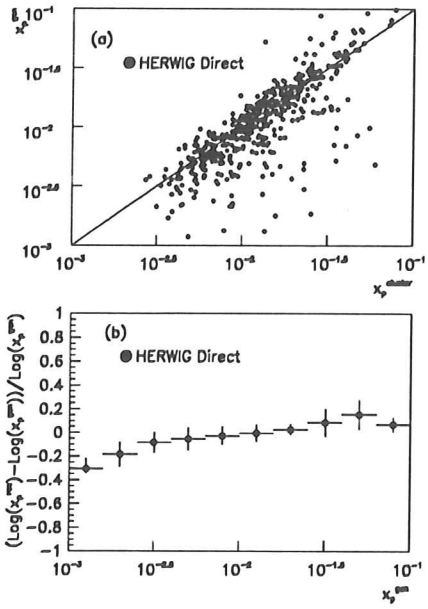

Figure E.2: (a) Correlation between the reconstructed x_p and the generated value. (b) The relative error, $(\log x_p^{rec} - \log x_p^{gen})/\log x_p^{gen}$, as a function of x_p^{gen}. The x_p value was estimated using two-jet events reconstructed by the cluster algorithm on direct-photon interactions simulated by the HERWIG generator.

does not reconstruct the proton remnant because it is based on transverse energy deposits, the proton remnant having little transverse energy.

Figure E.3 shows the correlation of the E^{jet}, φ^{jet}, η^{jet} and E_T^{jet} of each jet reconstructed by the cluster algorithm to the closest jet in R space reconstructed by the cone algorithm in each event. This comparison is done on the events that have been reconstructed by both algorithms, which amounts to more than 90% of the sample reconstructed by the cone algorithm. As can be seen in figure E.3, though the method behind these two algorithms for reconstructing the jets is completely different, the η^{jet} and φ^{jet} of each jet reconstructed by the two methods are highly correlated. On the other hand, the E^{jet} for each jet is somewhat higher for the jets reconstructed by the cluster algorithm since this algorithm groups all particles that fulfill the similarity condition, whereas the cone algorithm groups only the particles that are located within a finite size cone.

The $(\log x_p^{rec} - \log x_p^{gen})/\log x_p^{gen}$ distribution for the jets reconstructed using the cone algorithm is centered at -0.01 and has a resolution of 10%. Figure E.4a shows the correlation of x_p^{rec} to the x_p^{gen} and figure E.4b shows the correlation of the x_p calculated using the jets reconstructed by the cone algorithm to the value calculated using the jets reconstructed by the cluster algorithm. The reconstruction using the two different methods is very similar.

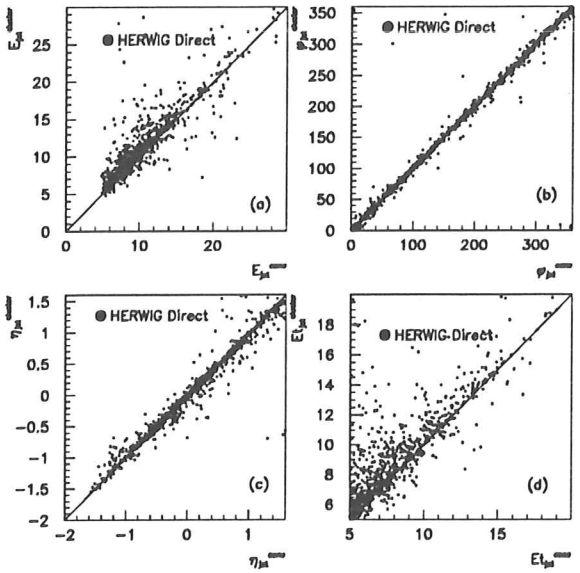

Figure E.3: (a) Correlation between the reconstructed E_{jet}^{cone} and $E_{jet}^{cluster}$. (b) Correlation between the reconstructed φ_{jet}^{cone} and $\varphi_{jet}^{cluster}$. (c) Correlation between the reconstructed η_{jet}^{cone} and $\eta_{jet}^{cluster}$. (d) Correlation between the reconstructed E_{Tjet}^{cone} and $E_{Tjet}^{cluster}$. These correlations correspond to direct processes simulated by the HERWIG generator, in which two jets were reconstructed (inside the kinematic region defined in the text) by the cluster algorithm and the cone algorithm. The assignment of jets is performed by comparing the closest pair in R space.

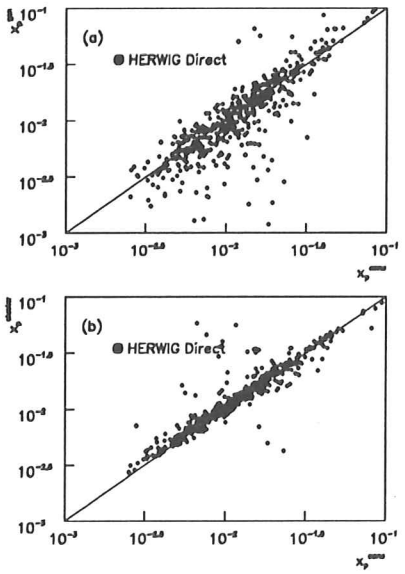

Figure E.4: (a) Correlation between the reconstructed x_p and the generated value. The x_p value was estimated using two-jet events reconstructed by the cone algorithm on direct processes simulated by the HERWIG generator. (b) Correlation between the reconstructed x_p^{cone} and $x_p^{cluster}$. This correlation corresponds to direct processes simulated by the HERWIG generator, in which two jets were reconstructed inside the kinematic region defined in the text by the cluster algorithm and the cone algorithm.

Appendix F

Reconstruction of jets

In order to study the reconstruction of jets based on the CAL, we have compared the *cal* jets to the *had* jets in samples of Monte Carlo generated events. The same jet algorithm as used for the data has been applied to the multihadronic final state and to the CAL cells in generated events of HERWIG and PYTHIA (see section 7.2). The samples of jets fulfilling the conditions $\{E_T^{cal} \geq 6$ GeV and $-1 \leq \eta^{cal} \leq 2\}$ and $\{E_T^{had} \geq 8$ GeV and $-1 \leq \eta^{had} \leq 2\}$ have been compared. In a given event, several jets of each type can be found and a definite rule for associating *cal* jets to *had* jets was set up: for each *had* jet the distance in η-φ space between that jet and each of the *cal* jets is computed via

$$d(had - cal) = ((\varphi^{had} - \varphi^{cal})^2 + (\eta^{had} - \eta^{cal})^2)^{1/2}$$

and the pair with minimum $d(had - cal)$ is taken if $d(had - cal) < 1$. Then, the variables characterizing the pair of matched jets are compared. As an example, figure F.1 shows the correlations of the jet variables with one entry per pair of matched jets for samples of resolved events from PYTHIA. These distributions show that the variables of the *cal* jets are well correlated with the ones of the *had* jets. Direct events from PYTHIA and resolved and direct events from HERWIG give similar results. The distributions for $\Delta\eta$, $\Delta\varphi$ and $\Delta E_T/E_T$ have been fitted to gaussian functions (see figure F.2) and the resulting values for the mean and the width are presented in table F.1. In the case of the angular variables, η^{cal} and φ^{cal}, there is no significant systematic bias and the resolutions are around 5° for φ^{cal} and 0.07 units for η^{cal}. These resolutions are a factor 10 smaller than the radius of the cone in the plane $\eta - \varphi$ which is used for the jet search ($R = 1$ unit). For the reconstruction of the transverse energy of the jet, E_T^{cal}, there is a systematic shift of $\sim$ -16% and the resolution is $\sim$ 11%.

MC sample	$\Delta\varphi$(mean)	$\Delta\varphi(\sigma)$	$\Delta\eta$(mean)	$\Delta\eta(\sigma)$	$\Delta E_T/E_T$(mean)	$\Delta E_T/E_T(\sigma)$
PYTHIA Resolved	0.6°	5.2°	−0.007	0.068	-16.5%	11.4%
PYTHIA Direct	0.4°	3.9°	−0.008	0.053	-16.2%	11.3%
HERWIG Resolved	0.3°	4.1°	−0.007	0.055	-14.5%	10.9%
HERWIG Direct	0.4°	3.8°	−0.009	0.049	-16.1%	11.2%

Table F.1: Resolutions for jet variables.

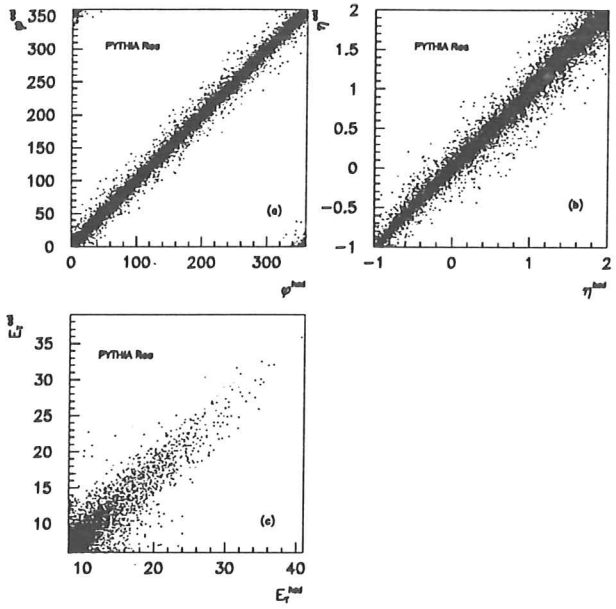

Figure F.1: (a) Correlation between φ^{cal} and φ^{had}; (b) Correlation between η^{cal} and η^{had}; (c) Correlation between E_T^{cal} and E_T^{had}.

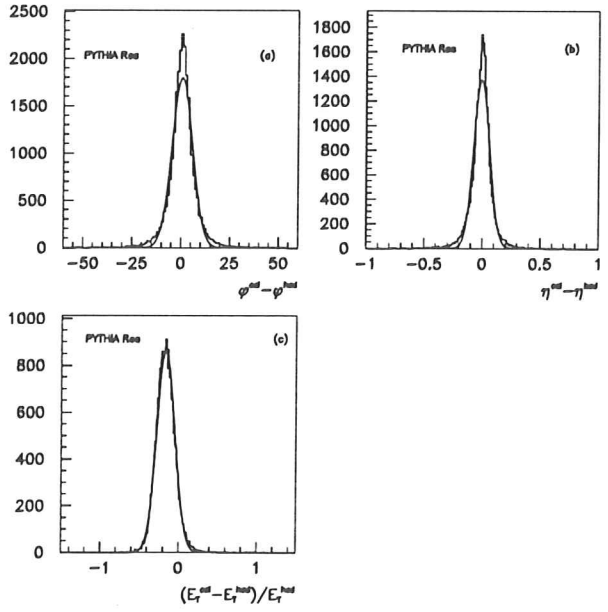

Figure F.2: (a) Distribution for $\varphi^{cal} - \varphi^{had}$; (b) Distribution for $\eta^{cal} - \eta^{had}$; (c) Distribution for $\frac{E_T^{cal} - E_T^{had}}{E_T^{had}}$.

Appendix G

Measurement of the kinematic region

The inclusive jet differential cross sections have been measured in the kinematic region given by $0.2 < y < 0.85$ and $Q^2 \leq 4$ GeV^2. The method used to constrain the data to this kinematic region is based on the rejection of DIS candidates, i.e. 'antitag condition' (see appendix A), and requiring $0.16 < y_{JB} < 0.7$.

The efectiveness of the antitag condition to restrict the data sample to the region $Q^2 \leq 4$ GeV^2 is studied here. In the PYTHIA and HERWIG generators, the lepton-photon vertex was modelled according to the Weizsäcker-Williams approximation except for direct processes in HERWIG, where the exact matrix elements were used (see section 4.2). Therefore, a sample of events of HERWIG direct should exhibit the correct Q^2 dependence. The $\log Q^2$-spectrum for the Monte Carlo generated events is presented in figure G.1 for the sample of matched pairs of *had-cal* jets (white histogram, one entry per match) with the *had* jets fulfilling $\{E_T^{had} \geq 8$ GeV; $-1 \leq \eta^{had} \leq 2$; $0.2 < y < 0.85\}$ and the *cal* jets with $E_T^{cal} \geq 6$ GeV and $-1 \leq \eta^{cal} \leq 2$; and the subsample of those events that passed all the selection criteria explained in section 7.1 (shaded histogram). At the second stage, among other requirements, the antitag condition was applied, resulting in the sharp cut of the $\log Q^2$-spectrum at $Q^2 \sim 4$ GeV^2 (vertical line). The fraction of number of entries with $Q^2 > 4$ GeV^2 with respect to the total is 1%. This result demonstrates that the antitag condition is very effective in restricting the sample to the region $Q^2 \leq 4$ GeV^2.

We have studied the reconstruction of y via the Jacquet-Blondel method using Monte Carlo samples. These samples have been selected requiring $\{E_T^{had} \geq 8$ GeV; $-1 \leq \eta^{had} \leq 2$; $0.2 < y < 0.85$; $Q^2 \leq 4$ GeV$^2\}$ and the *cal* jets have been selected according to $E_T^{cal} \geq 6$ GeV and $-1 \leq \eta^{cal} \leq 2$. Then, the 'true' value of y and the 'reconstructed' value y_{JB} were compared for each pair of matched *had-cal* jets. The correlation between y and y_{JB} has been studied for samples of PYTHIA and HERWIG (resolved and direct). It broadens as y increases and there is a systematic shift to lower values of y_{JB} which is slightly larger for resolved events than for direct. In order to choose the region of y_{JB} which corresponds to the range $0.2 < y < 0.85$, the mean value of the distribution for y_{JB} together with its width in each bin of y has been evaluated. The resulting values are shown in figure G.2 for PYTHIA, where the horizontal lines enclose the region $0.16 \leq y_{JB} \leq 0.7$. This interval constitutes a reasonable choice to select the region $0.2 < y < 0.85$, given the systematic shift and resolution of y_{JB}. The samples of HERWIG for resolved and direct processes give similar results. The effects of migrations inside and outside this region of y for the cross sections will be taken into account through the corrections for the purity (see appendix K).

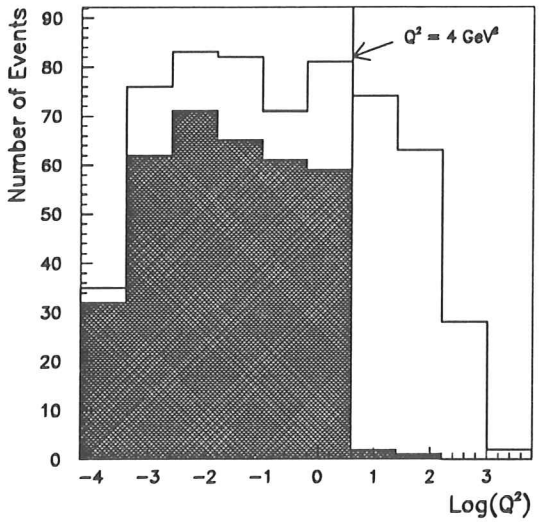

Figure G.1: Log Q^2 distribution for HERWIG direct events before data selection criteria (white histogram) and after full selection criteria (shaded histogram).

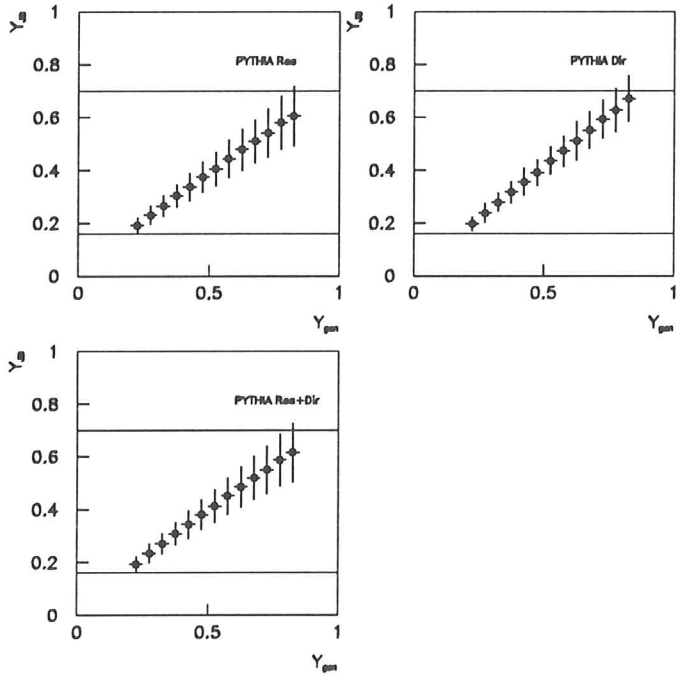

Figure G.2: $< y_{JB} >$ vs $< y >$ for PYTHIA.

Appendix H

Check of the energy scale of the calorimeter jets

In order to check the simulation of those aspects which affect the energy losses of the jets, we have compared for $|\eta^{cal}| \leq 1$ (region 1) the transverse momentum of charged particles as measured by the tracking detectors to the transverse energy of the *cal* jets, while in the region $1 \leq \eta^{cal} \leq 2$ (region 2), where the tracking information is at present insufficient, we have used the constraint that, due to transverse momentum conservation, the two jets in dijet events must be balanced.

H.1 Check of the energy scale of jets in the central region

In this region, we compare the transverse energy of the *cal* jets (E_T^{cal}) to the sum of the transverse momenta of charged particles as measured by the tracking detectors within the jet cone. The tracks are selected according to the conditions: $|\eta^{track}| \leq 1.5$ and $p_T^{track} > 300$ MeV. The pseudorapidity and azimuth of the line connecting the main vertex of the event with the entrance point of the track into the CAL is calculated, (η',φ'). A track is considered to be within a jet if

$$\sqrt{(\varphi' - \varphi^{cal})^2 + (\eta' - \eta^{cal})^2} < 1$$

The multiplicity of tracks within a jet for data (black dots) and PYTHIA (histogram) is shown in figure H.1a. The mean value of this distribution for data and Monte Carlo is 4.4 and the shape of the data distribution is well described by the Monte Carlo simulations. The mean multiplicity of charged tracks as a function of η^{cal} has been also studied (see figure H.1b). The mean multiplicity in the data (black dots) increases from 4 up to $\sim$ 4.75 as the jet moves forward from $\eta^{cal} \sim -1$ to 1, and the Monte Carlo simulations (white dots) reproduces well this increase. The distribution of the sum of the transverse momenta of the tracks within a jet for data (black dots) and Monte Carlo (histogram) is shown in figure H.1c. The data exhibit a steep spectrum which expands nearly three orders of magnitude in the range 1 to 20 GeV and it is well described by the Monte Carlo. From these comparisons, one can conclude that the Monte Carlo provides a good description of the characteristics of the tracks within a jet. Therefore, the transverse momentum of charged particles within a jet can be used to check the measurement of the jet transverse energy by the CAL.

For this purpose, we compare $E_T^{CTD} = \sum_{jet} p_T^{track}$ (sum of transverse momenta of the tracks

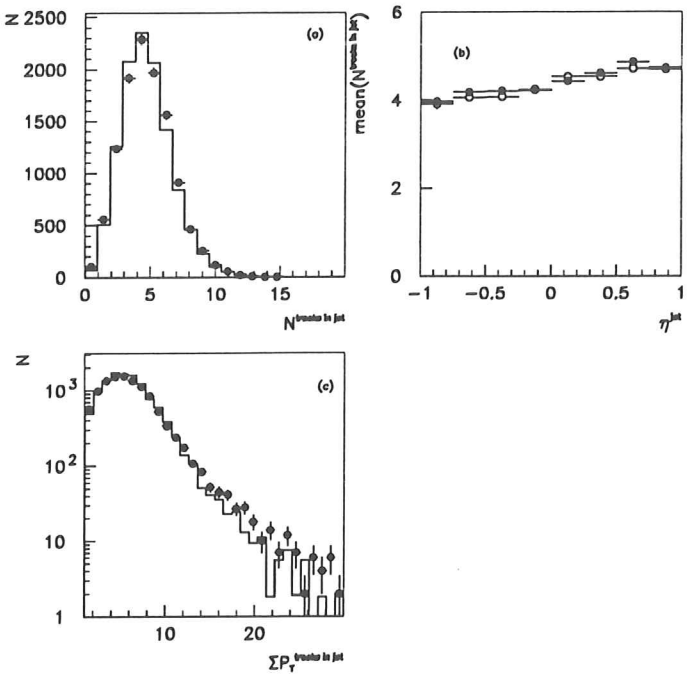

Figure H.1: (a) Multiplicity of charged particles within a jet for data (black dots) and PYTHIA (histogram); (b) mean multiplicity of charged particles within a jet as a function of η^{cal} for data (black dots) and PYTHIA (white dots); (c) sum of the transverse momentum of charged particles within a jet for data (black dots) and PYTHIA (histogram).

within a jet) and E_T^{cal}. An incomplete account in the simulation of the dead material in front of the CAL, will show as a difference in the ratio $f \equiv E_T^{CTD}/E_T^{cal}$ between data and Monte Carlo. In general, this ratio f can be written as

$$f = \frac{E_T^{CTD}}{E_T^{cal}} = \frac{x E_T^{had}}{E_T^{had}/(1+\delta)} = x(1+\delta)$$

The quantity x measures the fraction of the transverse energy of the jet carried by the charged particles and δ measures the CAL response to *had* jets. From this expression, it is seen that the difference $< f >_{data} - < f >_{MC}$ is sensitive to discrepancies in the energy scale of the jets:

$$\begin{aligned} < f >_{data} - < f >_{MC} &= x_{data}(\delta_{data}+1) - x_{MC}(\delta_{MC}+1) && \text{(H.1)} \\ &= (x_{data} - x_{MC}) + x_{data}\delta_{data} - x_{MC}\delta_{MC} && \text{(H.2)} \\ &\approx \Delta x + x\Delta\delta && \text{(H.3)} \end{aligned}$$

If we assume that $\Delta x = x_{data} - x_{MC} \approx 0$, i.e. that the relative amount of neutral particles in data and Monte Carlo is the same, then

$$< f >_{data} - < f >_{MC} \approx x\Delta\delta$$

and therefore

$$\Delta\delta = \delta_{data} - \delta_{MC} \approx \frac{< f >_{data} - < f >_{MC}}{x}$$

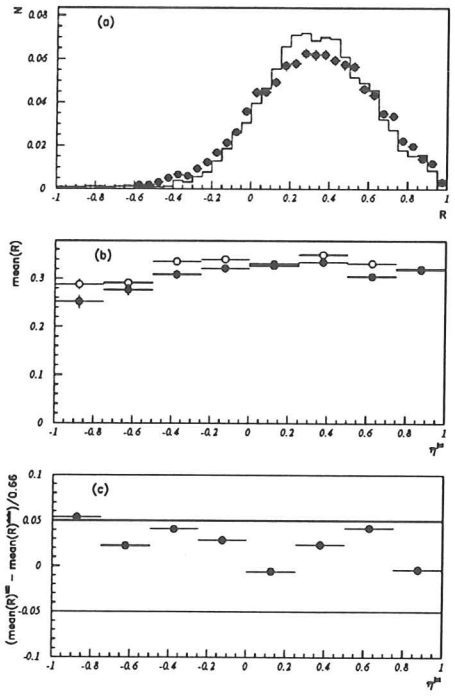

Figure H.2: (a) $R = (E_T^{cal} - E_T^{CTD})/E_T^{cal}$ for data (black dots) and PYTHIA (histogram); (b) Mean value $< R >$ as a function of η^{cal} for data (black dots) and PYTHIA (white dots); (c) Difference of the mean values $(< R >^{MC} - < R >^{data})/x$ (x is set to 0.66).

This assumption is justified since the charged multiplicity of the jets in data and Monte Carlo agrees and the validity of the LUND model for the fragmentation of partons has been supported (and indeed its parameter settings have been finely tuned) by experimental results in all high energy reactions. Therefore, the discrepancy in the transverse energy scale, $\Delta\delta$, can be estimated from this difference. The distribution of $R \equiv 1 - f$ for data and Monte Carlo is shown in figure H.2a. The most probable value is $\sim 30\%$ in both data and Monte Carlo and the shape of the distribution for the data is reasonably described by the Monte Carlo. The mean value of $R \equiv 1 - f$ as a function of η^{cal} for data and Monte Carlo is shown in figure H.2b. The Monte Carlo simulations exhibit the same features as the data although some differences can be seen; these differences are quantified in figure H.2c, where the value of $\Delta\delta$ is shown as a function of η^{cal} (the value of x has been taken ~ 0.66). The largest discrepancy amounts to $\sim 5\%$. From this study it is concluded that the discrepancy in the transverse energy scale of the jets between data and Monte Carlo is at most 5% and in average 2.7% in the region of $|\eta^{cal}| \leq 1$.

H.2 Check of the energy scale of jets in the forward region

In the forward region, we use the kinematic constraint that, for photoproduction interactions, $\not{P}_T \approx 0$, i.e. that the total transverse momentum is well balanced. In the case of dijet events, this balancing is done by the two jets: the mean value of the distribution $E_{T1}^{had} - E_{T2}^{had}$ is zero.

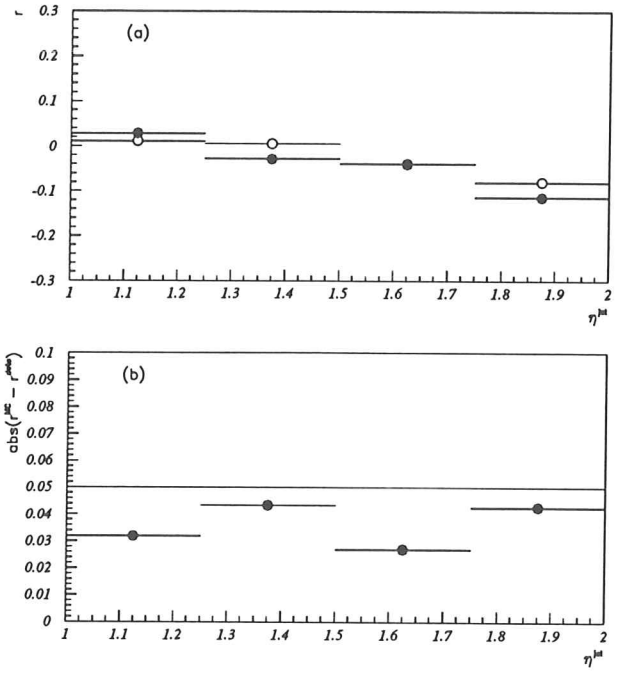

Figure H.3: (a) Mean value of the difference of transverse energies of jet 1 and jet 2 as a function of η^{jet2} for data (black dots) and PYTHIA (white dots); (b) energy scale uncertainty for forward jets obtained from (a).

On the other hand, due to the variation of the amount of dead material in front of the CAL with the polar angle, the mean value of this difference for the *cal* jets can be different from zero:

$$E_{T1}^{cal} - E_{T2}^{cal} = \frac{E_T^{had}}{1+\delta_1} - \frac{E_T^{had}}{1+\delta_2}$$

Therefore, if dijet events are selected such that one of the jets is in region 1, where the transverse energy scale of the *cal* jets has been checked (see previous section), and the other jet is restricted to region 2, the difference of the mean values of $(E_{T1}^{cal} - E_{T2}^{cal})/E_{T1}^{cal}$ in data and Monte Carlo is sensitive to discrepancies in the energy scale of the forward jets.

Figure H.3a shows the mean value of the distribution for $(E_{T1}^{cal} - E_{T2}^{cal})/E_{T1}^{cal}$, where jet 1 is in region 1, as a function of η^{jet2} for data (black dots) and PYTHIA (white dots). The Monte Carlo simulations exhibit the same trend as the data. The difference between data and Monte Carlo is quantified in figure H.3b; each point was obtained by taking the difference of the mean values for data and Monte Carlo in each bin of η^{jet2} and adding in quadrature the average uncertainty on the transverse energy scale of jet 1 (central region). From this figure it can be concluded that the discrepancies between data and Monte Carlo in the forward region are below 5%.

Figure H.4 summarizes the uncertainties on the simulation of the transverse energy scale for jets obtained with the two methods: they are below 5% in the range of η^{cal} considered. In order to take into account this uncertainty into our measurements of inclusive jet cross sections, a variation of the energy scale of the *cal* jets in the Monte Carlo by $\pm$ 5% has been included in the study of the systematic errors.

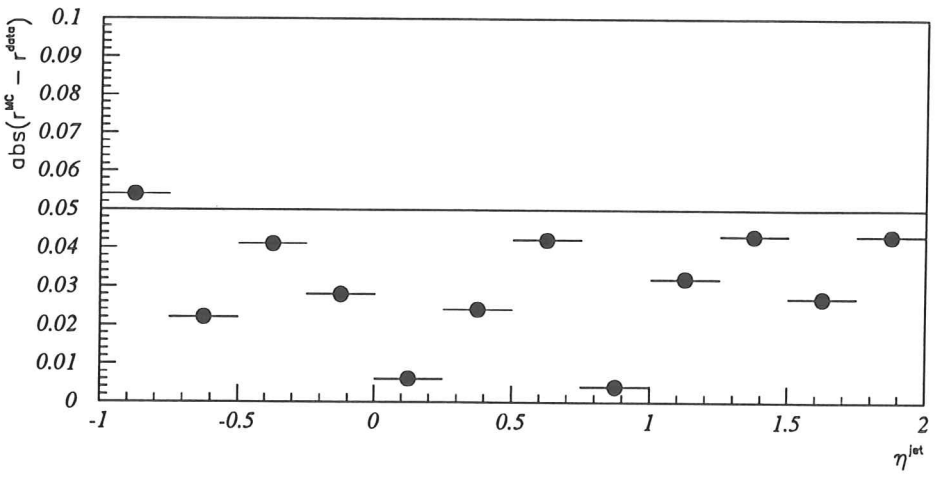

Figure H.4: Summary: energy scale uncertainty for jets as a function of η^{cal}.

H.3 Check of the energy scale of y

We have investigated the reliability of the CAL simulation for the measurement of y with the y_{JB} estimator by using the subsample of tagged events. Since the calibration of the electron energy in the LUMI has a precision of 1.5%, it is a good estimator of the true y. The reconstruction of y via y_{JB} is affected mainly by energy losses due to dead material in front of the CAL or in the rear beam pipe. In both cases, the y_{JB} method gives a value which underestimates the true y. An incomplete implementation of these effects in the simulation of the detector will show up in the comparison of the ratio $(y_{true} - y_{JB})/y_{true}$ in data and Monte Carlo. We have evaluated the mean value of this ratio in the data (using the value y_{LUMI} as y_{true}) and in the Monte Carlo (where the true y as given by the generator has been used) as a function of y_{true}. The mean values for data (black dots) and Monte Carlo (white dots) are presented in figure H.5a. The Monte Carlo simulations reproduce the trend of the data although some differences are visible in the high-y region. These discrepancies are quantified in figure H.5b, where the difference between the mean value for Monte Carlo and data is shown as a function of y. The largest discrepancy occurs at high-y values and is below 5%. We include a variation of y_{JB} in the Monte Carlo of -5% as an additional contribution to the total uncertainty of our measurement of the inclusive jet cross sections.

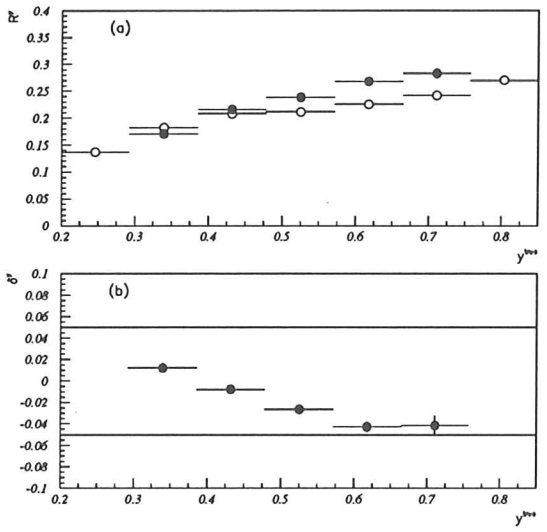

Figure H.5: (a) Data (black dots): $< (y_{LUMI} - y_{JB})/y_{LUMI} >$. PYTHIA (white dots): $< (y_{true} - y_{JB})/y_{true} >$; (b) energy scale uncertainty for y.

Appendix I

Energy correction to jets

In order to measure the inclusive jet differential cross sections, the 'observed' number of jets and the 'raw' variables E_T^{cal} and η^{cal} have to be corrected for detector effects and acceptances. For this purpose, we first determine the relationship between the 'raw' variables (E_T^{cal},η^{cal}) and the 'true' ones (E_T^{had},η^{had}) using Monte Carlo samples. Then, we use the Monte Carlo samples to determine the relationship between the 'observed' number of jets in each bin of the 'corrected' E_T^{cal} or η^{cal} and the 'true' number of jets in the same bins of E_T^{had} or η^{had} (see appendix K). Moreover, these 'observed' distributions refer to the number of jets observed in a given region of measured y and Q^2. The relationship between the kinematic region selected and the one where the cross section is given, has been studied using also the Monte Carlo samples (see appendix G).

For these studies, Monte Carlo samples of events have been generated with PYTHIA and HERWIG simulating resolved and direct processes and processed through the detailed simulation of the ZEUS detector. We have used these events to define the sample of *had* jets whose cross section we want to measure, and to define the sample of observed *cal* jets which should mimick the jets as measured using the ZEUS detector.

This appendix is devoted to explain the method developed to correct the transverse energy of the jets.

I.1 Construction of the 'map' of energy corrections

The angular variables, η^{cal} and φ^{cal}, and the transverse energy, E_T^{cal}, of the *cal* jets have to be corrected back to the values which characterize the *had* jets. In appendix F, the correlation between the variables of the *cal* and *had* jets was studied. The distributions for $\Delta\varphi$ and $\Delta\eta$ were fitted to gaussian functions and from the results obtained it was concluded that no significant systematic shift in the angular variables η^{cal} and φ^{cal} was present: for φ^{cal}, the mean value was slightly positive and below 1° and for η^{cal} it was below 10^{-2} in magnitude. The resolutions were around 5° in φ^{cal} and 0.07 units of pseudorapidity in η^{cal}. These resolutions settle the minimum bin size for the η^{cal} variable, which we take in the following as 0.25 units. Therefore, for the measurement of the differential jet cross sections in η^{jet} in the ranges $E_T^{had} \geq 8$ GeV and $-1 \leq \eta^{had} \leq 2$, the precision provided by the CAL is good enough that corrections to the angular variables of the jets are not needed and one can safely identify the η^{cal} of the jet as measured by the CAL with the η^{had} of the *had* jet: $\eta^{had} \sim \eta^{cal} \sim \eta^{corr}$.

Now we turn to the correction of the transverse energy of the *cal* jets. In appendix F, the distributions for $(E_T^{cal} - E_T^{had})/E_T^{had}$ were presented. A systematic shift between -14.5% and

-16.5% was observed depending on the Monte Carlo sample used. This indicates that there are energy losses which affect the E_T^{jet} as measured by the CAL which have to be corrected. Several sources are affecting the energy of a jet as measured by the CAL (see section 7.4). We evaluate the energy corrections using Monte Carlo samples of events that have been processed through the simulation of the ZEUS detector which takes into account those effects.

We construct the correction factor for E_T^{cal} as a multiplicative function:

$$E_T^{corr} = C(E_T^{cal}, \eta^{cal}) \cdot E_T^{cal}$$

The evaluation of this function C depends on the choice of the threshold for E_T^{cal}. In a first step we determine this threshold as a function of η^{cal}: how far we have to go down in E_T^{cal} to assure that we are selecting *cal* jets which probe the $E_T^{had} \geq 8$ GeV *had* jets we are interested in. One expects the threshold in E_T^{cal} to be η^{cal} dependent due to the different amount of dead material in front of the CAL as a function of the polar angle. In order to compute this threshold, we select *had* jets with the conditions $\{E_T^{had} \geq 8$ GeV; $-1 \leq \eta^{had} \leq 2$; $0.2 < y < 0.85$ and $Q^2 \leq 4$ GeV$^2\}$ and compare them to the matched *cal* jets restricted to fulfill all the offline conditions and $\{E_T^{cal} \geq 5$ GeV and $-1 \leq \eta^{cal} \leq 2\}$. Then, we evaluate the mean value of the distribution for E_T^{had}/E_T^{cal} in each bin of η^{had} (the range $-1 \leq \eta^{had} \leq 2$ is divided into 12 equally spaced bins),

$$T_I = < E_T^{had}/E_T^{cal} > (\eta^{had} \in bin\ I)$$

for $I = 1$ to 12. The function T has been computed using the Monte Carlo generators PYTHIA and HERWIG, and different processes (resolved, direct and a mixture of resolved+direct according to the Monte Carlo expectations for the cross sections of these two processes). The results for PYTHIA are shown in figure I.1. The function T as determined using the PYTHIA sample of resolved+direct varies between 1.18 and 1.31 in the η^{had} region considered, showing two prominent peaks in the regions $\eta^{had} \sim 1$ and $\eta^{had} \sim -1$. These are understood in terms of the increase of dead material implemented in the detector simulation in those regions. This structure is also exhibited by the individual samples (resolved or direct) and by the samples of HERWIG (see figure I.2). The largest discrepancy between HERWIG and PYTHIA is 3% of the value given by PYTHIA. The spread of the values of T exhibited by the different samples of events (resolved vs direct, PYTHIA vs HERWIG, etc) is due to the fact that the particle content of the jets varies from one to the other. The energy loss of a jet depends on the p_T-spectrum of the individual hadrons which form the jet, and the composition of the jet is expected to vary from resolved to direct events depending on the nature of the underlying parton (quark or gluon) and from one generator to another depending on the specific fragmentation scheme employed (PYTHIA uses the LUND model and HERWIG the cluster model). The whole procedure of computing the transverse energy corrections to jets will be made in parallel for PYTHIA and HERWIG samples, and the two set of corrections obtained will be used in the determination of the differential cross sections.The difference between them will serve to estimate the contribution of the fragmentation scheme to the total systematic uncertainty of the measurements.

Now that the function T has been determined, *cal* jets will be selected in what follows according to an η^{cal}-dependent threshold:

$$E_T^{cal}(\eta^{cal} \in bin\ I) \geq \frac{8\ GeV}{T_I}$$

In order to compute the 'map' of the CAL response to *had* jets, the distribution of E_T^{had}/E_T^{cal} is examined in bins of (E_T^{cal}, η^{cal}). The mean value of this distribution is displayed in figures I.3

(PYTHIA) and I.4 (HERWIG) as a function of E_T^{cal} for each bin of η^{cal}:

$$C_{\eta^{cal} \in bin I}(E_T^{cal}) =< E_T^{had}/E_T^{cal} > (\eta^{cal} \in bin I)$$

These functions have been fitted to the form

$$C_I(E_T^{cal}) = A_I^1 + A_I^2 \cdot e^{A_I^3 \cdot E_T^{cal}}$$

The parametrizations obtained are displayed in figures I.3 and I.4 as solid lines. The complete set of 12 functions, $C_I(E_T^{cal})$ for I = 1,...,12, for a given Monte Carlo generator (HERWIG or PYTHIA) represents the correction factor for the transverse energy of a jet, $C(E_T^{cal}, \eta^{cal})$, as a function of E_T and η of the jet as measured by the CAL.

We have checked the consistency between the two 'maps', the one of PYTHIA and the one of HERWIG, correcting the transverse energy of the jets in the sample of HERWIG using the function T and the 'map' C obtained with PYTHIA. The mean value of the distribution of E_T^{had}/E_T^{corr} thus obtained as a function of E_T^{corr} in each bin of η^{corr} is shown in figure I.5, where the shaded region indicates the band 1.00 $\pm$ 0.05. In this way, it is demonstrated that the transverse energy of the jets in the HERWIG sample as measured by the CAL is corrected back to the transverse energy of the *had* jets within $\pm$ 5%.

The choice of the bin size in E_T^{corr} has been determined studying the resolution on the E_T^{corr} variable. The distributions of $E_T^{corr} - E_T^{had}$ in bins of E_T^{corr} have been fitted to gaussian functions and the resulting σ_{E_T} are: 0.9, 1.5, 1.8, 1.8, 1.9, 2.0, 2.1 and 2.5 GeV for E_T^{corr} bins 8-11, 11-14, 14-17, 17-20, 20-23, 23-26, 26-32 and 32-41 GeV. We have chosen accordingly the bin sizes, taking approximately twice the value of σ_{E_T}: 8-11, 11-14, 14-17, 17-21, 21-25, 25-29, 29-35 and 35-41 GeV. These are the bins in E_T^{corr} used for the measurement of the differential cross section in E_T^{jet}.

At this point we have completed the program of correcting the 'raw' variables, E_T^{cal} and η^{cal}, back to the 'true' ones characterizing the *had* jets, E_T^{had} and η^{had}, that can be identified with E_T^{corr} and η^{corr}. In the rest of the section we study the validity of the 'maps' obtained (using γp generators) with samples of jets generated through the DIS process and the level of consistency with the 'map' resulting from applying the whole procedure to Monte Carlo samples of DIS.

I.1.1 Energy corrections to jets in DIS

To check the possible dependence of the function T and the transverse energy corrections to jets C on the specific models used in the γp generators (HERWIG and PYTHIA), we have evaluated the functions T and C using Monte Carlo samples of DIS. These samples were generated with $Q^2 > 4$ GeV^2 using the program HERACLES [69], which includes first order electroweak radiative corrections. The hadronic final state was simulated using the color-dipole model [48] including boson gluon fusion as implemented in ARIADNE [70] for the QCD cascade, and JETSET [49] for the hadronization. These samples will be referred to as CDMBGF. The proton parton densities were chosen to be the MRSD$-'$ set [27]. The same procedure as applied above for the jet search in the CAL using γp Monte Carlo samples has been performed in the DIS samples produced with the CDMBGF generator except that the CAL cells asociated with the scattered electron have been removed. In the same fashion, *had* jets have been searched in the multihadronic final state excluding explicitely the scattered electron and photons from initial or final state radiation off the electron.

First of all, the reconstruction of the *had* jets using the CAL has been made as in appendix F. The mean values and widths of the gaussian fits to the distributions of $\Delta\varphi$ and $\Delta\eta$ are

consistent with the ones from PYTHIA and HERWIG, showing no significant systematic shift and the same resolutions in the angular variables of the jets.

We have evaluated the function T using Monte Carlo samples of DIS where the jet search has been performed according to the criteria: $\{E_T^{cal} \geq 5$ GeV and $-1 \leq \eta^{cal} \leq 2\}$ and $\{E_T^{had} \geq 8$ GeV and $-1 \leq \eta^{had} \leq 2\}$, without any further requirement at the generator or offline levels. The resulting T function is compared to the ones obtained using the samples of HERWIG and PYTHIA in figure I.6. In this figure, the functions T for the HERWIG and PYTHIA samples have been evaluated without imposing any further requirements at the generator or offline levels. These estimations of the function T serve two purposes: a) the comparison to the ones in figures I.1 and I.2 shows that the function T for the γp Monte Carlo samples depends very weakly on the additional imposition of conditions at generator or offline levels; b) the function T_{DIS} exhibits the same behaviour as the ones of PYTHIA and HERWIG and the largest discrepancy between DIS and PYTHIA is 3% of the value of PYTHIA.

Once T^{DIS} has been evaluated, we compute the correction factor for the transverse energy of the jets C_{DIS}, selecting *cal* jets in the DIS sample according to the criteria:

$$E_T^{cal}(\eta^{cal} \in bin\ I) \geq \frac{8\ GeV}{T_I^{DIS}}$$

The mean value of the distribution of E_T^{had}/E_T^{cal} in bins of (E_T^{cal},η^{cal}) is shown in figure I.7 (black dots) together with the fits (solid lines) and the parametrizations obtained using PYTHIA (dashed lines). The DIS parametrizations agree with the ones of PYTHIA in most of the range in E_T^{cal} and η^{cal} considered. We have checked the consistency between the PYTHIA and the CDMBGF 'maps': *cal* jets are selected in the DIS sample according to the threshold function T^{PYTHIA}, and then, the selected *cal* jets are corrected using the function C^{PYTHIA}. Finally, the mean value of the distribution of E_T^{had}/E_T^{corr} for the E_T-corrected jets of the DIS sample as a function of E_T^{corr} in bins of η^{corr} is evaluated. These mean values are shown in figure I.8, where the shaded region indicates the band 1.00 ± 0.05. Thus, it is demonstrated that the transverse energy of the *cal* jets in the DIS sample is well corrected back to the transverse energy of the *had* jets within $\pm$ 5%.

These comparisons show that the effect of the detector on the *had* jets depends weakly on the specific Monte Carlo model used (low-Q^2 processes simulated by PYTHIA or HERWIG, or DIS processes simulated by CDMBGF). This is understood as we are comparing *had* jets and *cal* jets in the same region of jet variables (E_T and η), where one expects DIS and γp jets to be very similar.

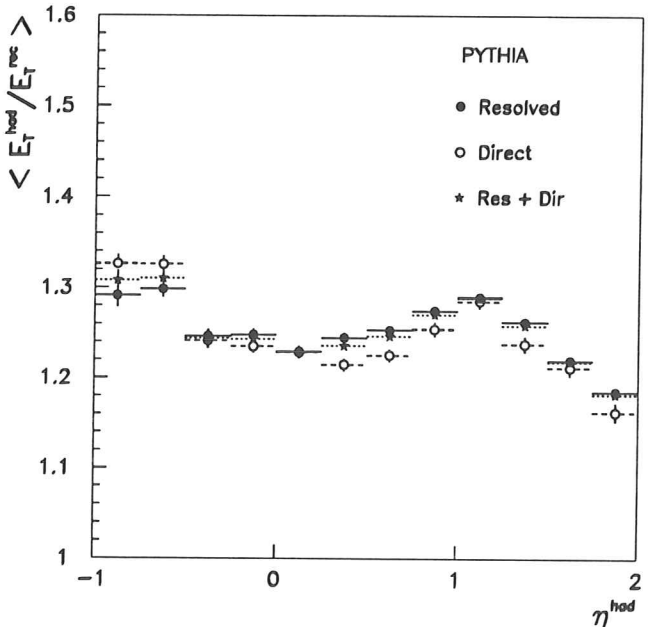

Figure I.1: Threshold function for PYTHIA: resolved (black dots); direct (white dots) and resolved+direct (black stars) ($E_T^{rec} \equiv E_T^{cal}$).

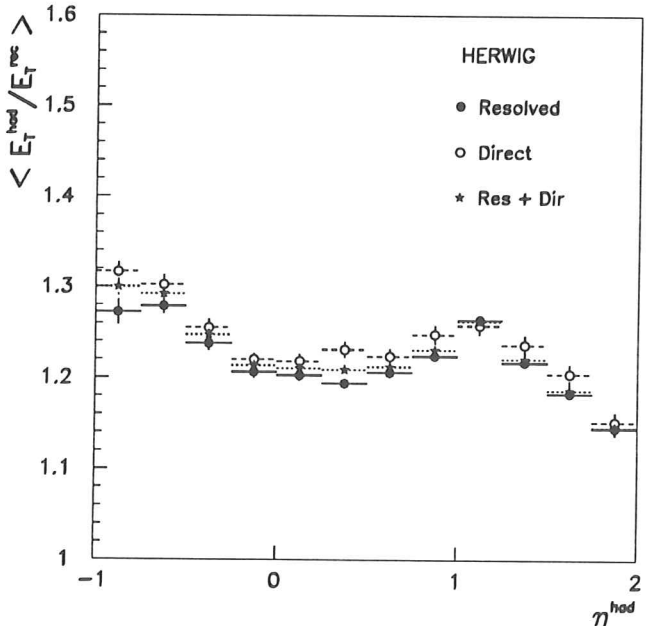

Figure I.2: Threshold function for HERWIG: resolved (black dots); direct (white dots) and resolved+direct (black stars) ($E_T^{rec} \equiv E_T^{cal}$).

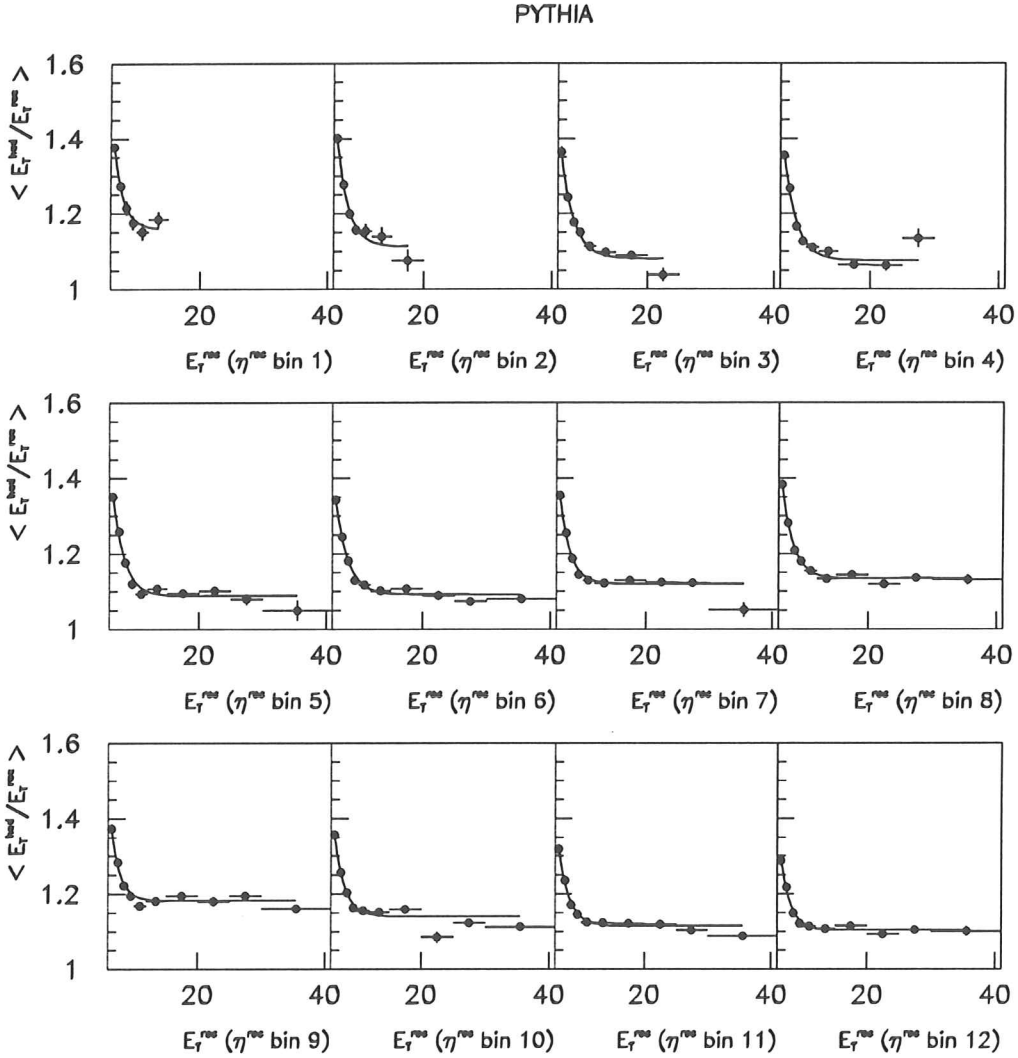

Figure I.3: PYTHIA map ($E_T^{rec} \equiv E_T^{cal}$).

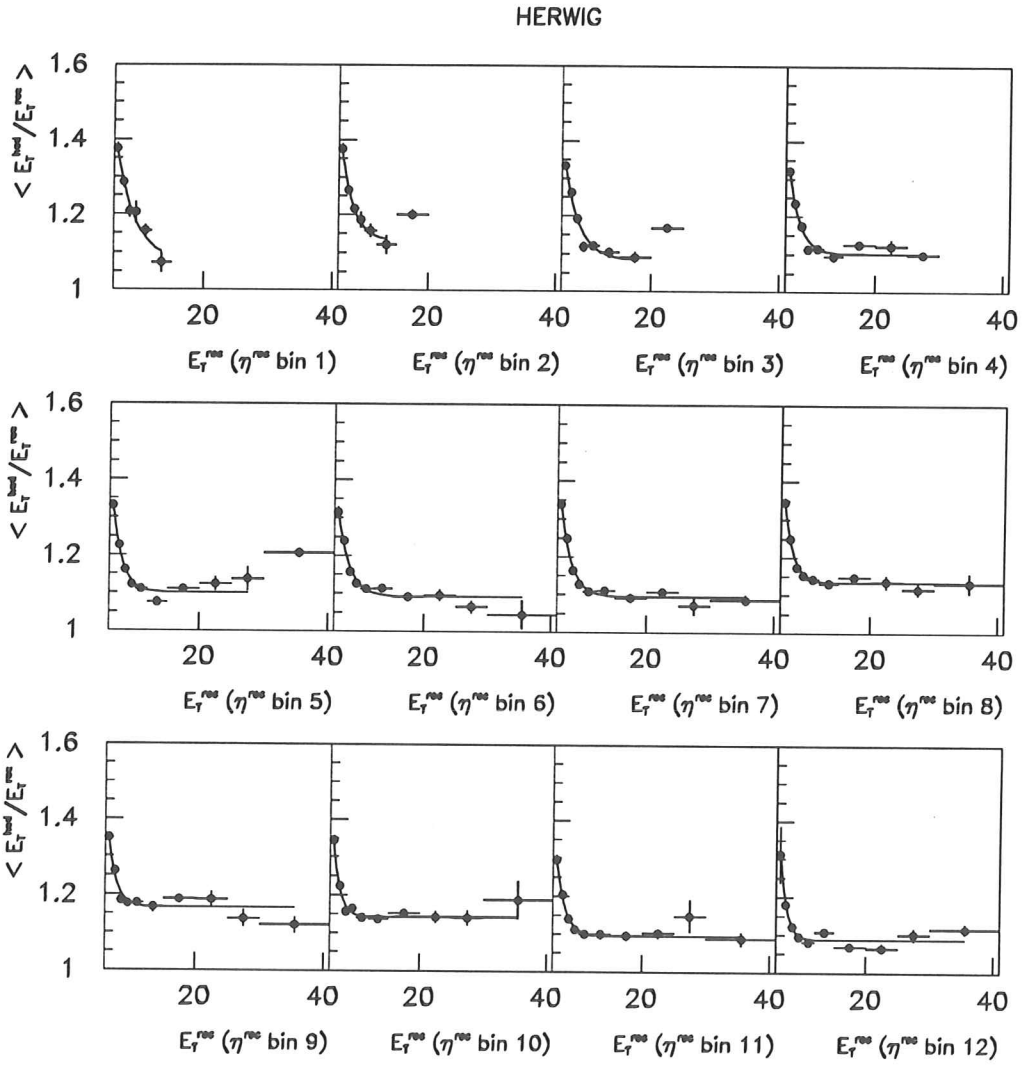

Figure I.4: HERWIG map ($E_T^{rec} \equiv E_T^{cal}$).

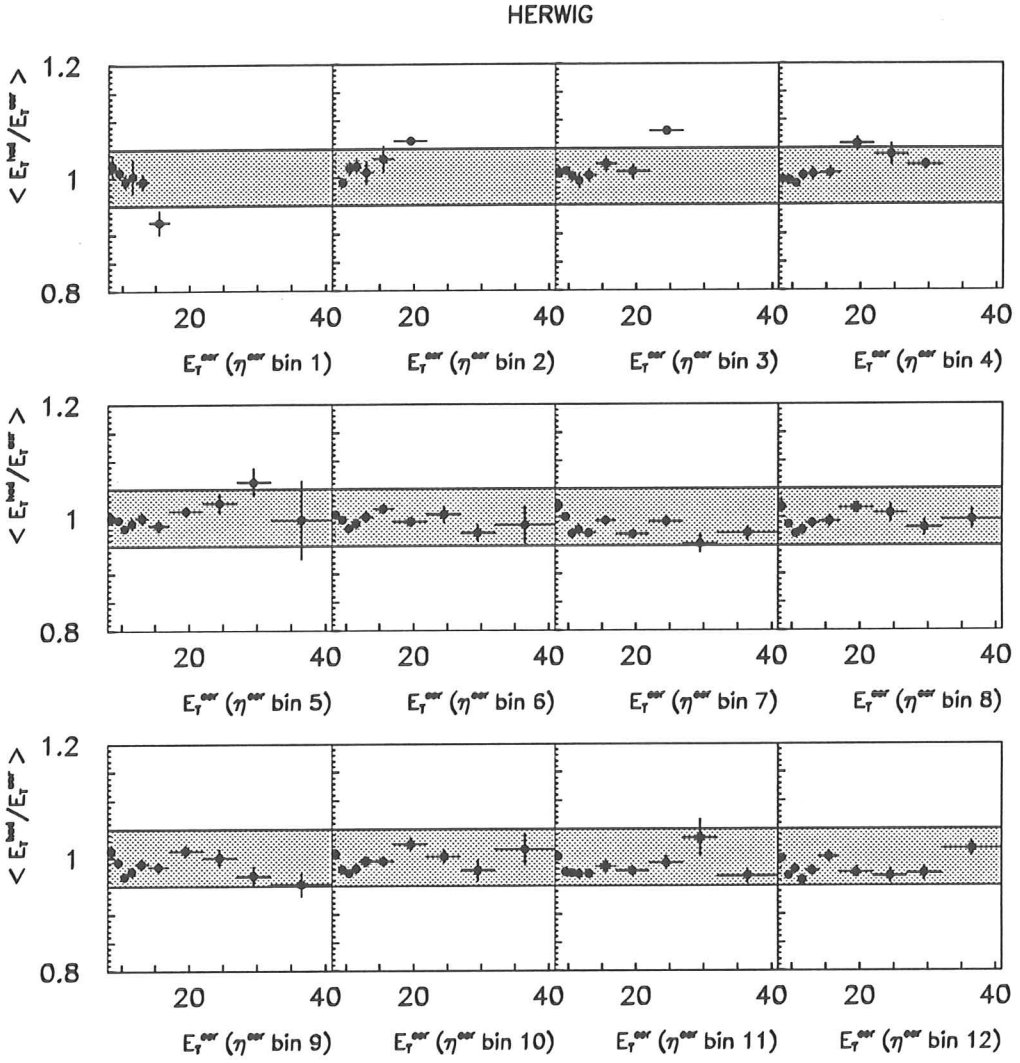

Figure I.5: HERWIG calorimeter jets corrected back to hadron level using the PYTHIA map.

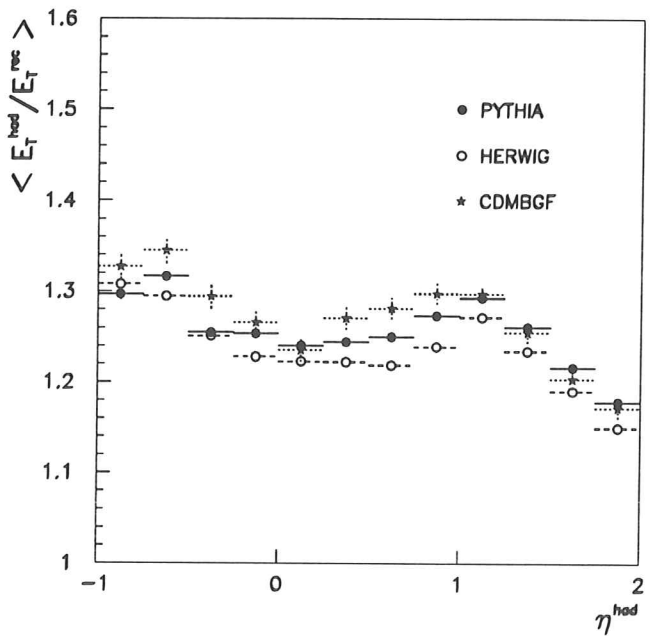

Figure I.6: Threshold functions for: PYTHIA Res+Dir (black dots); HERWIG Res+Dir (white dots) and CDMBGF (black stars) ($E_T^{rec} \equiv E_T^{cal}$).

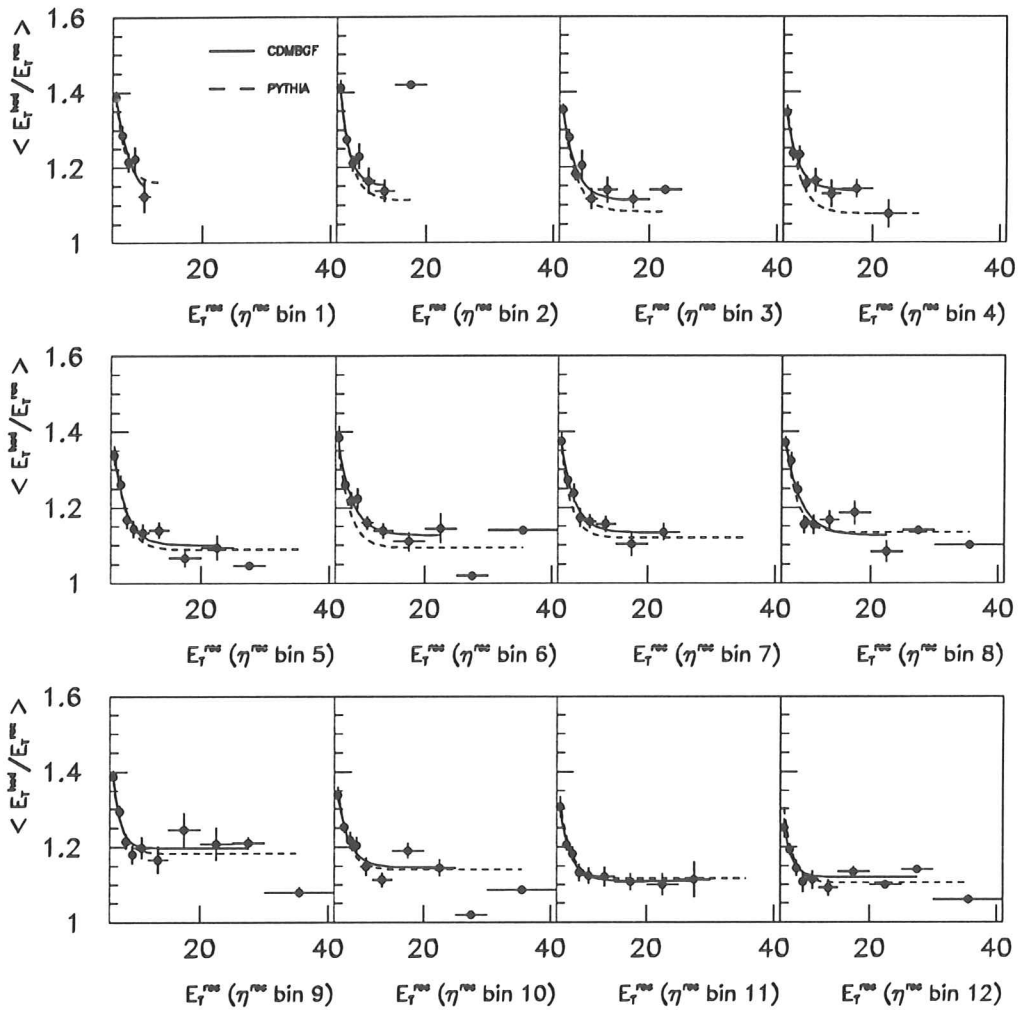

Figure I.7: CDMBGF map ($E_T^{rec} \equiv E_T^{cal}$).

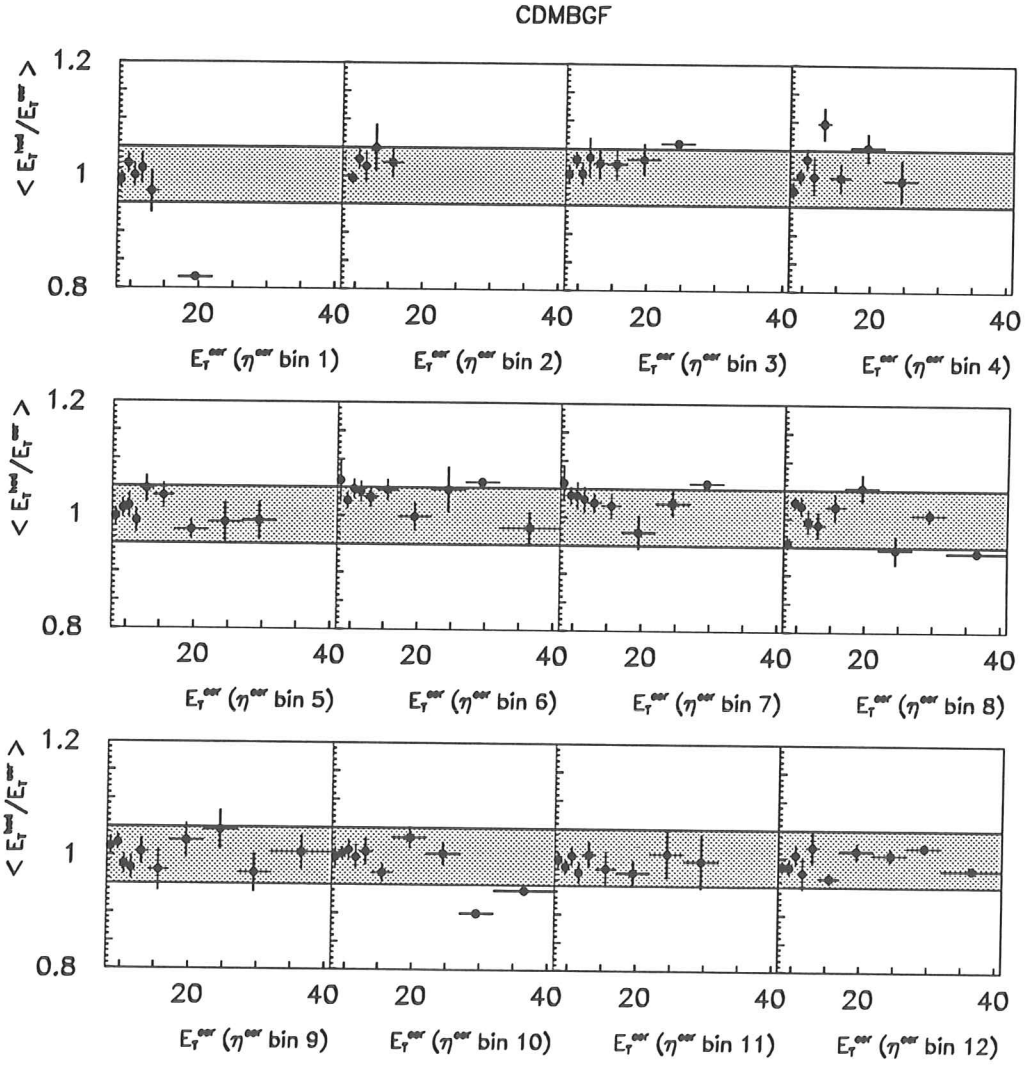

Figure I.8: CDMBGF calorimeter jets corrected back to hadron level using the PYTHIA map.

Appendix J

The observed η^{jet} and E_T^{jet} distributions

We have studied the description of the inclusive jet data distributions by the Monte Carlo generators. The jets are requested to fulfill the condition $E_T^{corr} \geq 8$ GeV, where their transverse energy have been corrected according to the parametrizations obtained with the Monte Carlo samples (see appendix I). As we have two complete set of corrections, one from PYTHIA and one from HERWIG, the results obtained with each of them are shown (figures J.1 and J.2). In these figures, the expectations from the Monte Carlo generators are normalized to the statistics of the data and the resolved and direct contributions were added according to the Monte Carlo cross section when used together. The Monte Carlo expectations have been also corrected with the same set as the data in each case.

As can be seen in the figures, both PYTHIA and HERWIG reproduce roughly the shapes of the η^{corr} and E_T^{corr} distributions of the data. The η-spectrum is best described by PYTHIA when LAC1 is used. The η^{corr} data distribution shows an excess in the very forward region ($\eta^{corr} \sim 2$) which is not accounted for when GRV is used instead: the predictions of PYTHIA and HERWIG with GRV are flatter than the ones with LAC1 in that region. It is also seen that the resolved contributions alone are not able to reproduce the exact shape of the data in the central and backward regions ($\eta^{corr} \leq 0.5$). This is an indication for the presence of the direct contribution in our data.

For the E_T^{corr} distribution, the best description is achieved by resolved PYTHIA GRV. In the case of PYTHIA LAC1, the E_T^{corr} distribution of the data is between the descriptions given by resolved and resolved+direct. The data point to a somewhat reduced contribution of the direct with respect to the resolved at high E_T^{corr} values.

Rather than attempting to fit the data distributions changing the available parameters of the Monte Carlo's in order to achieve the best agreement, it is preferable to account for the discrepancies between the acceptance corrections obtained with different mixtures of the processes involved as systematic uncertainties of our measurements.

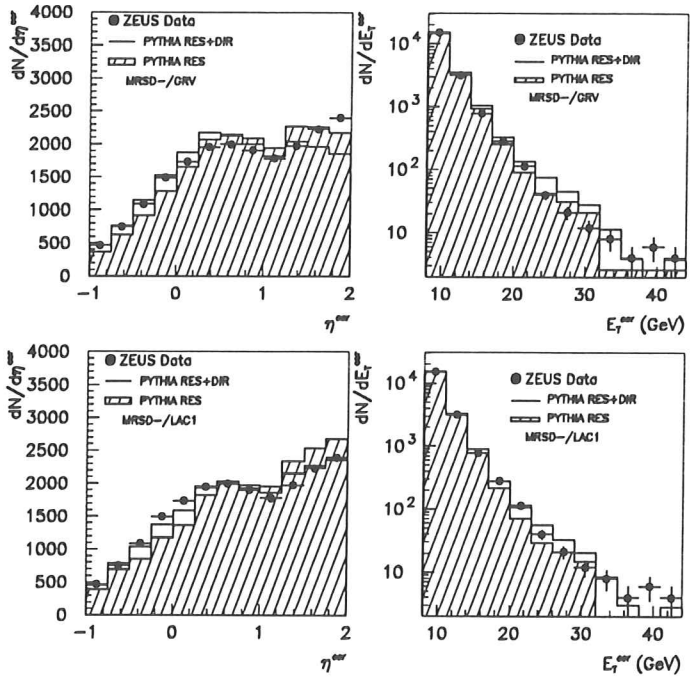

Figure J.1: η^{corr} and E_T^{corr} for data corrected with PYTHIA Monte Carlo (black dots) and PYTHIA Monte Carlo including resolved (shaded histogram) and resolved+direct (white histogram) using GRV (upper row) and LAC1 for the photon parton parametrizations (lower row).

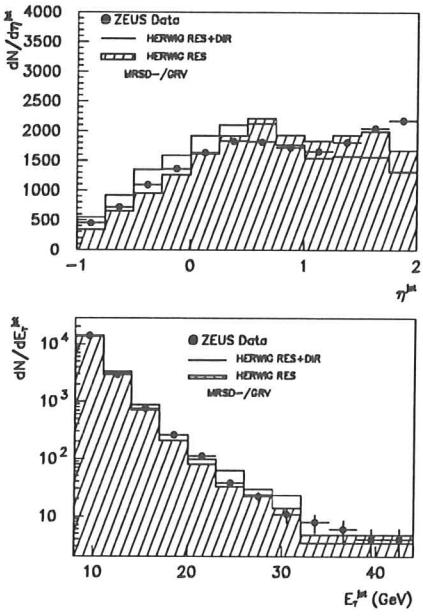

Figure J.2: η^{corr} and E_T^{corr} for data corrected with HERWIG Monte Carlo (black dots) and HERWIG Monte Carlo including resolved (shaded histogram) and resolved+direct (white histogram) using GRV for the photon parton parametrizations.

Appendix K

Acceptance corrections to inclusive jet distributions

In appendix I the procedure to correct the 'raw' jet variables, E_T^{cal} and η^{cal}, back to the 'true' ones and the appropriate bin size for the distributions in these variables were explained. The η^{corr} and E_T^{corr} distributions for the inclusive jet data sample thus obtained do not yet reflect the true distributions for the jets of hadrons due to the acceptance and the purity. Monte Carlo samples have been used to correct these distributions for both effects.

The limited acceptance is due to several sources: a) the efficiency of the jet algorithm in the CAL; b) the efficiency of the trigger; and c) the filter and offline selection criteria. On the other hand, the migrations from outside the selected kinematic region or the (E_T,η) ranges considered are responsible for the limited purity. First, we study the acceptance and purity as functions of η^{jet} and E_T^{jet}, and then the results of the two generators, PYTHIA and HERWIG, are compared. Next we evaluate the total correction factor for the inclusive jet distributions. Finally, the full procedure to calculate the jet differential cross sections (energy corrections to jets and acceptance corrections to the observed inclusive jet distributions) is applied to a Monte Carlo sample to check its reliability, i.e. whether the original cross section is recovered.

K.1 Acceptance and purity

Let V be one of the two variables (η^{jet} or E_T^{jet}), then we define the acceptance for each V^{had}-bin and the purity for each V^{corr}-bin as follows:

– **Acceptance:** $A(V^{had} \in$ bin I) is defined as the ratio of the number of *had* jets with $V^{had} \in$ bin I which have a matched *cal* jet (with $V^{corr} \in$ 'range'[1]) over the total number of *had* jets with $V^{had} \in$ bin I.

– **Purity:** $P(V^{corr} \in$ bin J) is defined as the ratio of the number of *cal* jets with $V^{corr} \in$ bin J which have a matched *had* jet (with $V^{had} \in$ 'range') over the total number of *cal* jets with $V^{corr} \in$ bin J.

Therefore, the acceptance defined in this way measures the percentage of *had* jets in each bin of the variable V^{had} which are actually reconstructed (in any bin of V^{corr}). In such one-dimensional representation, it does not represent the migrations from bin-to-bin but the efficiency to detect *had* jets as a function of the true variable V. In the case of the purity, it measures the percentage of *cal* jets in each bin of the variable V^{corr} which have a corresponding

[1] For $V^{corr} = E_T^{corr}$ 'range' means $E_T^{corr} \geq 8$ GeV and for $V^{corr} = \eta^{corr}$ 'range' means $-1 \leq \eta^{corr} \leq 2$

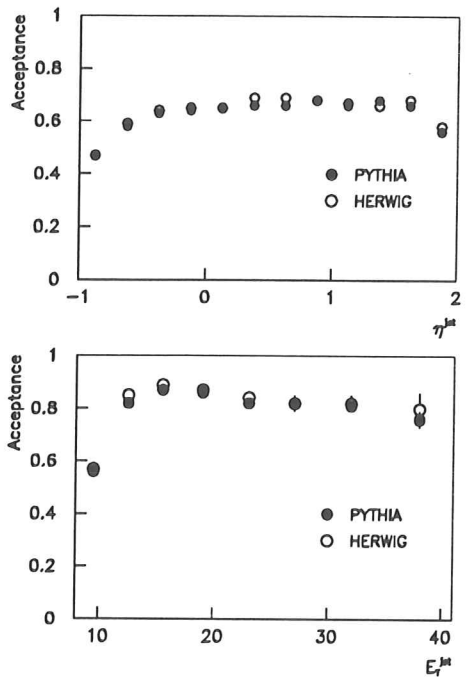

Figure K.1: Acceptance for PYTHIA (black dots) and HERWIG (white dots) as a function of η^{jet} and E_T^{jet}.

had jet (in any bin of V^{had}), i.e. $1 - P$ represents the amount of contamination in each bin V^{corr} (*cal* jets which have no matched *had* jets constitute a source of contamination, in the sense that the corresponding *had* jet variables, η^{had} or/and E_T^{had}, or/and the event variable y, are outside the limits considered in the selection of *had* jets).

The acceptance and purity as computed using the PYTHIA (black dots) and HERWIG (white dots) samples are presented in figures K.1 and K.2. For each generator its own function T and transverse energy corrections have been used.

The results obtained with the two generators are consistent. The $P(\eta^{corr})$ distribution is flat in the range considered and varies between 58% and 71% for PYTHIA and between 60% and 73% for HERWIG. The amount of 'contamination' extends over the whole spectrum of η^{corr} at a constant level. The acceptance as a function of η^{had} is also rather flat and takes values between 47% and 68% for PYTHIA and between 47%-69% for HERWIG, slightly decreasing at both ends of the η-spectrum. As a function of E_T^{corr}, the purity increases from 58% (60%) in the lowest E_T^{corr} bin up to 98% (100%) in the highest E_T^{corr} bin for PYTHIA (HERWIG). A similar trend can be observed for the E_T^{had}-dependence of the acceptance as computed with PYTHIA (HERWIG), starting at 56% (57%) in the lowest bin and reaching values in the range 76-87% (80-89%) for higher E_T^{had}. The largest discrepancies between the acceptances (purities) using PYTHIA and HERWIG are 3% (8%) for η^{had} (η^{corr}) and 4% (4%) for E_T^{had} (E_T^{corr}). This indicates that the systematic effects coming from the different fragmentation schemes and parton shower models used in PYTHIA and HERWIG have relatively small influences on the determination of the acceptances and purities for the inclusive jet η and E_T distributions.

The migration effects from bin-to-bin in E_T^{corr} have been studied using a matrix representation, $M(V^{had} \in bin\ I, V^{corr} \in bin\ J)$. It is defined as the ratio of the number of *had* jets with

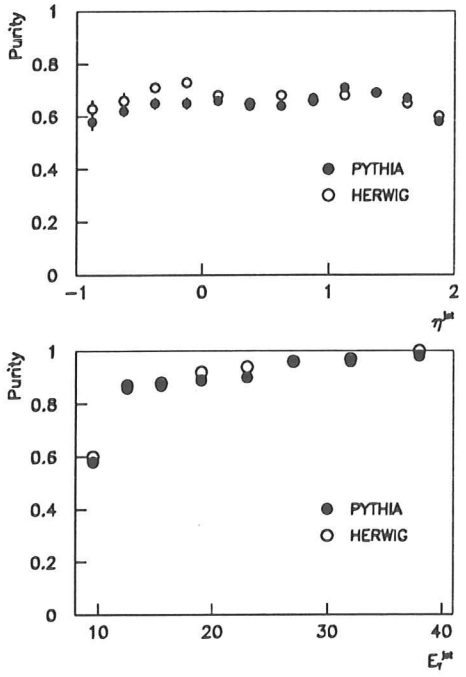

Figure K.2: Purity for PYTHIA (black dots) and HERWIG (white dots) as a function of η^{jet} and E_T^{jet}.

$V^{had} \in bin\ I$ which have a matched *cal* jet with $V^{corr} \in bin\ J$ over the number of *had* jets with $V^{had} \in bin\ I$. The values of the matrix $M(E_T^{had}, E_T^{corr})$ obtained with the PYTHIA samples are presented in table K.1. The elements of the diagonal, which represent the probability for a *had* jet in a given bin of E_T^{had} to be reconstructed as a *cal* jet with an E_T^{corr} in the same bin, take values in the range 38% to 50%. Apart from these elements, only those located at $(I+1, I)$ are significant. The small values taken by the elements above the diagonal confirms the goodness of the choice of binning in E_T^{corr}. As the differential cross section in E_T^{jet} is very steep, the presence of migrations from low-E_T to high-E_T would have strongly distorted the E_T^{corr} distribution and made the determination of $d\sigma/dE_T^{jet}$ difficult. These migrations are quantified by the elements above the diagonal and, as it can be seen in our case, are small: the value of $M(I, I+1)$ is below 9% for all I.

K.2 Correction factor

The differential cross section in V is obtained correcting bin-by-bin the inclusive jet data distribution in the variable V^{corr} for both the acceptance and the purity

$$\frac{d\sigma}{dV}(\text{bin I}) = \frac{\#\text{DATA jets with } V^{corr} \in I}{L \cdot \Delta V} \cdot \frac{\#\text{had jets with } V^{had} \in I}{\#\text{cal jets with } V^{corr} \in I}$$

where L is the integrated luminosity, ΔV is the bin width and the second factor on the right hand side has been computed using the Monte Carlo samples. This factor will be denoted by $D(V^{corr}, V^{had})$ in what follows.

E_T^{corr} bins →	8-11	11-14	14-17	17-21	21-25	25-29	29-35	35-41
E_T^{had} bins ↓								
8-11	.502	.060	.001	.000	.000	.000	.000	.000
11-14	.325	.448	.051	.001	.000	.000	.000	.000
14-17	.054	.345	.405	.060	.001	.000	.000	.000
17-21	.019	.067	.294	.424	.054	.001	.000	.000
21-25	.006	.013	.038	.288	.397	.073	.002	.000
25-29	.004	.007	.010	.044	.266	.384	.083	.011
29-35	.000	.000	.007	.005	.051	.209	.467	.063
35-41	.000	.006	.008	.013	.032	.025	.215	.493

Table K.1: Matrix M for inclusive jet E_T using PYTHIA.

The correction factors D obtained using PYTHIA (black dots) and HERWIG (white dots) samples are presented in figure K.3. The factors D obtained with the two generators are consistent with each other in most of the E_T^{jet} and η^{jet} ranges considered. For the E_T^{jet} distribution it varies between 0.96 and 1.37 using PYTHIA and between 1.01 and 1.48 using HERWIG. Therefore, they deviate from unity less than 37% (48%) in the case of PYTHIA (HERWIG). The values obtained by PYTHIA and HERWIG differ by less than 5% except in the highest E_T^{jet} bin where the difference amounts to 16% (in that bin the statistics of the HERWIG sample is poor and the values of the two generators agree within the errors). In the case of η^{jet}, the correction factor takes values between 0.90 and 1.17 for PYTHIA and between 0.90 and 1.28 for HERWIG. The deviation of this factor from unity is below 17% (28%) in the case of PYTHIA (HERWIG) and the difference between the two generators is below 10%.

K.3 Measurement of inclusive jet $d\sigma/d\eta^{jet}$ and $d\sigma/dE_T^{jet}$ using a Monte Carlo sample: a case study

Before applying the procedure developed for measuring the differential jet cross sections to the data, we have checked its reliability using the Monte Carlo samples of one generator as 'data' and the correction procedure obtained with the other.

We present first the case where PYTHIA is taken as 'data' and HERWIG as the Monte Carlo which provides the corrections. The steps followed are:

– The PYTHIA events are selected according to the same criteria as the real data, i.e. the trigger + filter + offline + jet conditions are required.

– Then the jets are further required to fulfill the HERWIG threshold condition

$$E_T^{cal}(\eta^{cal} \in bin\ I) \geq \frac{8\ GeV}{T_I^{HERWIG}}$$

– Transverse energy corrections are applied to the PYTHIA 'data' jets using the set of parametrizations of HERWIG

$$E_T^{corr} = C_I^{HERWIG}(E_T^{cal}) \cdot E_T^{cal}(\eta^{cal} \in bin\ I)$$

– The inclusive jet distributions in η^{corr} and E_T^{corr} for the PYTHIA 'data' sample are corrected for acceptance and purity using of the factor D as computed with HERWIG:

$$\frac{d\sigma_{PYT}^{meas}}{dV}(\text{bin I}) = \frac{\#\text{PYTHIA DATA jets with } V^{corr} \in I}{L_{PYT} \cdot \Delta V} \cdot D^{HERWIG}(V^{corr} \in I, V^{had} \in I)$$

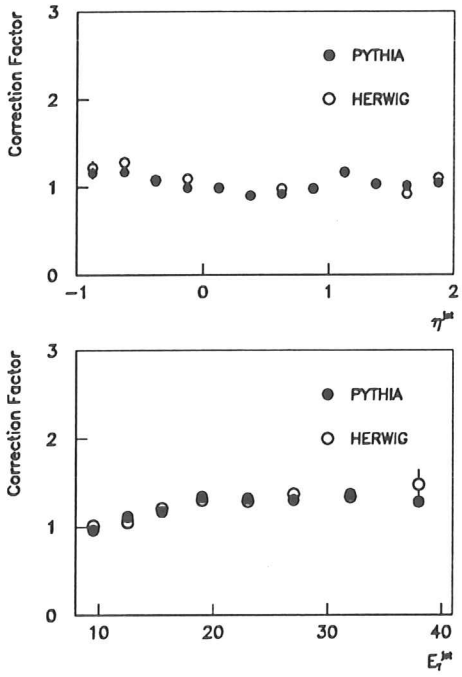

Figure K.3: Correction factor for PYTHIA (black dots) and HERWIG (white dots) as a function of η^{jet} and E_T^{jet}.

where L_{PYT} is the 'integrated luminosity' corresponding to the size of the PYTHIA sample considered. The cross sections thus obtained are referred as the 'measured PYTHIA cross sections'.

– Finally, the 'true' differential cross sections for inclusive jet production in PYTHIA are computed selecting *had* jets and applying the conditions at generator level:

$$\frac{d\sigma^{true}_{PYT}}{dV}(\text{bin I}) = \frac{\#\text{PYTHIA had jets with } V^{had} \in I}{L_{PYT} \cdot \Delta V}$$

The 'measured' and 'true' differential cross sections of inclusive jet production in E_T^{jet} and η^{jet} are compared in figure K.4a and K.4b. The difference between the 'measured' and the 'true' differential cross sections is below 14% for η^{jet} except in the next-to-last bin where the difference increases to 17%. For E_T^{jet}, the difference is below 20% except in the last two bins, where the statistics of the PYTHIA 'data' are very poor.

This check has been repeated exchanging the roles of PYTHIA and HERWIG. The results are compared in figure K.4c and K.4d. The percentual difference between the 'measured' and 'true' differential cross sections in η^{jet} is below 11%. This difference is largest in the next-to-last bin as in the previous case. In the case of E_T^{jet}, the difference is below 14% in most of the range, reaching highest values in the last bin due to the poor statistics of the HERWIG 'data' sample.

In summary, when the full procedure designed to measure the differential cross sections is cross-checked between two completely different Monte Carlo generators, the original cross sections are recovered with an accuracy better than 20%. These checks demonstrate the validity of our approach.

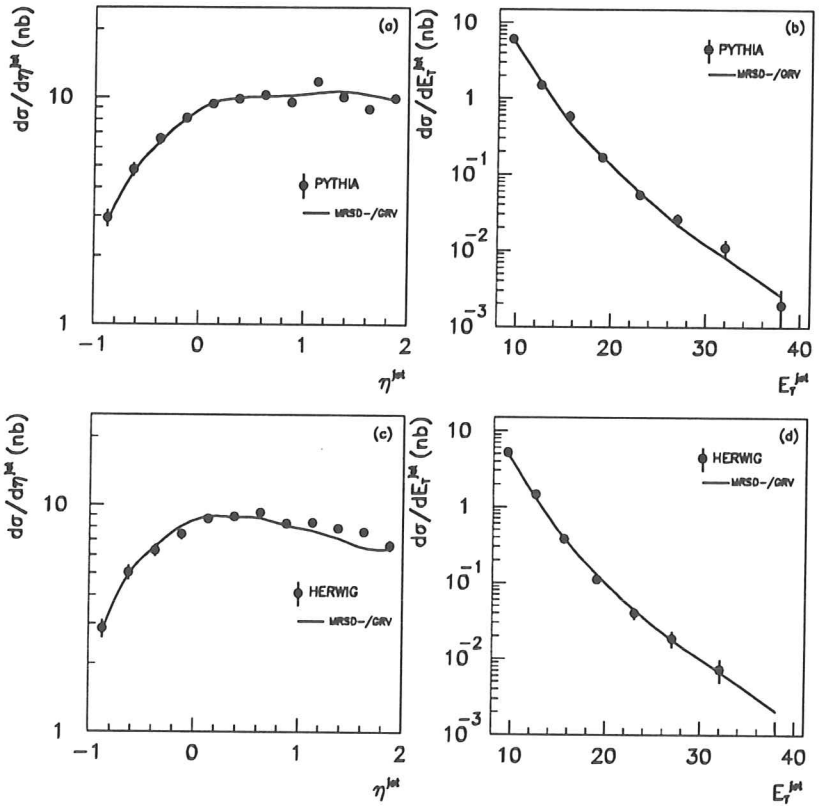

Figure K.4: a) $d\sigma/d\eta^{jet}$ for PYTHIA 'data' and PYTHIA Monte Carlo; b) $d\sigma/dE_T^{jet}$ for PYTHIA 'data' and PYTHIA Monte Carlo; c) $d\sigma/d\eta^{jet}$ for HERWIG 'data' and HERWIG Monte Carlo; d) $d\sigma/dE_T^{jet}$ for HERWIG 'data' and HERWIG Monte Carlo.

Appendix L

Search for hard diffraction contributions to inclusive jet production and its influence on the measurement of $d\sigma/d\eta^{jet}$ and $d\sigma/dE_T^{jet}$

There is experimental evidence for hard scattering processes in diffractive reactions in hadron-hadron collisions [71] and deep inelastic neutral current ep scattering [16]. It is based on the observation of jet production: two high-p_T jets back-to-back in the transverse plane in proton-tagged reactions in $p\bar{p}$ [71] and in large-rapidity-gap DIS ep collisions [16]. This mechanism should be also present in the low-Q^2 regime of ep interactions and it is expected to contribute to jet production. A search for this type of contribution has been performed in the selected data sample to establish its existence and estimate its magnitude, and to evaluate the influence on the measurements of differential cross sections for inclusive jet production. This influence should be understood in the sense that the corrections used for the measurements have been evaluated using Monte Carlo generators that do not contain this type of diffractive processes and, in principle, there could be some effect. We do not attempt to separate the data sample into a large-rapidity-gap and a non-rapidity-gap subsamples to measure the inclusive jet cross sections for each of them. The LO QCD predictions that we aim to compare to the measurements are cross sections for inclusive jet production summed over all possible final states, regardless of the presence of a large rapidity gap [72].

The search for a posssible hard diffraction contribution to the inclusive jet data sample has been carried out using the η_{max} variable [12, 16], which is defined as the pseudorapidity of the most forward cluster of adjacent CAL cells. The η_{max} distribution (one entry per jet) of the inclusive jet data sample is shown in figure L.1a (there are 67 jets with $\eta_{max} \leq 1.8$). The expectation from PYTHIA including resolved and direct (normalized to the data statistics) is also shown: the data shows an excess at η_{max} below 1.8 which cannot be reproduced by the standard final states simulated in that generator. The η_{max} distribution for the resulting inclusive jet diffractive sample using POMPYT is included in figure L.1a (normalized to the data statistics below $\eta_{max} \leq 1.8$). In the framework of this model, there is a contribution of hard diffractive processes to inclusive jet production both with and without a large rapidity gap, the latter being dominant.

In order to estimate the magnitude of the contribution from diffractive processes, the integrated η_{max} distribution normalized to the total sample has been used: $R(\eta^0_{max})$ is defined as

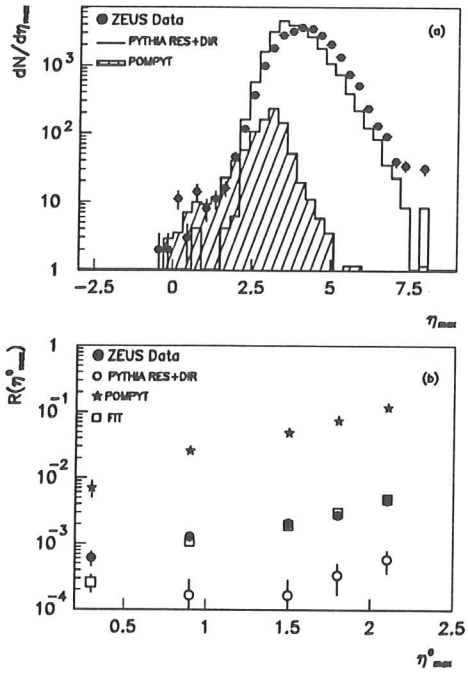

Figure L.1: (a) η_{max} distribution for data (black dots), PYTHIA resolved+direct (white histogram) and POMPYT (shaded histogram); (b) $R(\eta^0_{max})$ for data (black dots), PYTHIA resolved+direct (white dots), POMPYT (black stars) and the fit to the data (white squares).

the ratio of the number of jets with $\eta_{max} \leq \eta^0_{max}$ over the total number of jets in the sample. The distribution of $R(\eta^0_{max})$ in the data and the expectations of PYTHIA and POMPYT are presented in figure L.1b and table L.1. From this, we conclude that the fractions predicted by POMPYT are too large and the ones by PYTHIA are too small compared to the data. Thus, it is not possible to reproduce the distribution of the data neither with PYTHIA or POMPYT alone and a mixture of both type of processes is needed. The predictions for $R(\eta^0_{max})$ adding PYTHIA and POMPYT according to the Monte Carlo cross sections as given by these generators are presented in table L.1 (column denoted by PYT+POM). The resulting values are closer to the data, but still they are systematically above the data. The fraction of POMPYT to the total sample is 6.7%, as predicted by the Monte Carlo, which is larger than what is seen in the data. We have performed a 'fit' to determine the magnitude of the diffractive contribution to the inclusive jet sample which the data require. The first four points in the $R(\eta^0_{max})$ distribution have been used to perform the 'fit' of the expectations of PYTHIA+POMPYT to the distribution of the data. The relative amount of the POMPYT contribution to the total has been chosen as the free parameter of the fitting procedure. The expectations for $R(\eta^0_{max})$ are shown in figure L.1b and in table L.1 (column denoted by PYT+POM(fit)) and are in agreement with the data. The contribution of diffractive processes to the inclusive jet sample as given by the fit is 3.6%, a factor two smaller than the Monte Carlo expectations from POMPYT for the particular choice of a hard gluon content in the pomeron. This indicates that the predictions given by the model implemented in POMPYT are somewhat larger, but not too far from our results (given all the uncertainties in this model).

As it is seen in figure L.1a, a large fraction of diffractively produced jets (POMPYT sample)

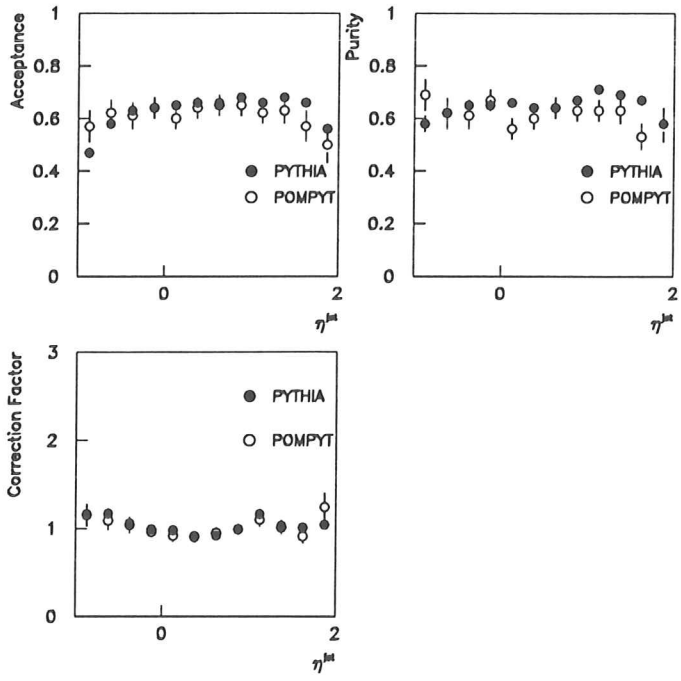

Figure L.2: Acceptance, purity and correction factor for PYTHIA resolved+direct (black dots) and POMPYT (white dots) as a function of η^{jet}.

η^0_{max}	Data	PYTHIA	POMPYT	PYT+POM	PYT+POM(fit)
0.3	0.06%	0.00%	0.70%	0.05%	0.03%
0.9	0.13%	0.02%	2.56%	0.19%	0.11%
1.5	0.21%	0.02%	4.86%	0.34%	0.19%
1.8	0.27%	0.03%	7.35%	0.52%	0.30%
2.1	0.46%	0.06%	11.8%	0.84%	0.48%

Table L.1: $R(\eta^0_{max})$ values for the data, PYTHIA (resolved+direct), POMPYT and two mixtures of PYTHIA+POMPYT.

populates the region where the distinction between diffractive and non-diffractive processes cannot be made in terms of the variable η_{max}. Therefore, the estimated contribution of the diffractive processes to the total inclusive jet sample is model dependent. We do observe that a certain fraction of jets populates the region $\eta_{max} \leq 1.8$, but when we have estimated the magnitude of the contribution, it has been assumed that the η_{max} distribution of the POMPYT model for $\eta_{max} \geq 1.8$ is reliable. We have no experimental evidence for this to be true due to the lack of additional information that could signal the diffractive nature of the collision without relying on the η_{max} variable. Nevertheless, we can compare the predictions of the POMPYT model for the absolute number of jets predicted. A total of 89 jets with $\eta_{max} \leq 1.8$ are expected for the integrated luminosity taken during 1993 and we observe 67 jets of such type in our data sample. Therefore, at least in the 'observable' region $\eta_{max} \leq 1.8$ we find a rough agreement between data and the absolute predictions of POMPYT.

In summary, from this study it is concluded that we observe diffractive processes contribut-

ing to inclusive jet production. The observed number of jets in the region $\eta_{max} \leq 1.8$ is in rough agreement with the absolute predictions of POMPYT and, within the framework of this model, the contribution of this type of process, as required by the data, to the total inclusive jet sample amounts to 3.6%.

Once we have seen evidence for the contribution of hard diffractive processes to inclusive jet production, its influence on the measurements of $d\sigma/d\eta^{jet}$ and $d\sigma/dE_T^{jet}$ have been determined using the POMPYT samples. The environment in which the jets are immersed is quite different in diffractive and non-diffractive reactions. In diffractive processes, initial and final state parton radiation is suppressed due to the reduced centre-of-mass energy available at the hard collision. In addition, the absence of colour flow between the hadronic system steaming from the photon-pomeron or parton-pomeron collision gives rise to a pattern of the forward energy flow which would strongly contrast with the one in non-diffractive reactions. We evaluate the correction factors for the inclusive jet cross sections D (see appendix K) using the POMPYT samples alone. These are compared to the ones obtained with PYTHIA to check the sensitivity of these factors to the different final states simulated by the two generators.

The POMPYT samples were used to evaluate the correction factors D to the inclusive jet η^{corr} and E_T^{corr} distributions. The same procedure as the one explained in appendix K was used. Note that we do not apply any cut on η_{max}: the full sample of *had* and *cal* jets is considered. We have then corrected the transverse energies of the POMPYT *cal* jets according to the set of parametrizations given by PYTHIA (T^{PYTHIA} and C_I^{PYTHIA}). The acceptance and purity factors were then evaluated. The results for η^{jet} are shown and compared to the ones of PYTHIA in figure L.2. We note that the Monte Carlo statistics of POMPYT is not large enough to discuss the acceptance, purity and correction factor as a function of E_T^{jet}. On the other hand, for the η^{jet} distribution it is large enough except at the ends of the spectrum (the shape of the η^{jet} distribution is similar to the one of direct processes in PYTHIA or HERWIG, peaking at central values). The acceptance, purity and correction factor for the POMPYT sample of jets exhibit the same trends as PYTHIA and in most of the η^{jet} range both samples give consistent results. The difference in the correction factor $D(\eta^{corr})$ between POMPYT and PYTHIA is below 10% over the whole range except in the most forward bin, where the difference increases up to 19% (there the uncertainty in the evaluation of $D_{POMPYT}(\eta^{corr})$ is largest due to the poor statistics of the POMPYT sample in that bin). In summary, these studies show that indeed the acceptances, purity and correction factors do not depend on the environment where the jet is embedded, as exemplified by the extreme choice of correcting the data with diffractively produced jets alone.

The data shows evidence for a contribution from diffractive processes and the previous study shows that even the correction factors computed using POMPYT alone do not significantly differ from the ones by PYTHIA. Nevertheless, the properties of the bulk of the data sample cannot be reproduced by diffractive processes alone. A more realistic measure of the uncertainty connected to the influence of the diffractive processes on the correction factors would come from the comparison between the results obtained with PYTHIA and the ones evaluated using a mixture of PYTHIA (resolved+direct) and POMPYT samples (added according to the Monte Carlo cross sections as given by these generators). As expected from the previous study and the small contribution assigned to the diffractive processes, the difference between the measured cross sections obtained correcting the data either with PYTHIA or with PYTHIA+POMPYT is very small ($\sim$ 1%).

Appendix M

Study of the systematic errors in the measurement of inclusive jet cross sections

The systematic errors and the stability of the extracted inclusive jet cross sections have been checked by varying one by one the ingredients used in the analysis. For each change, the differential cross sections were recalculated and compared to the *reference* values in each bin of η^{jet} or E_T^{jet}. The *reference* values were obtained using PYTHIA including resolved+direct processes with MRSD− and GRV for the proton and photon parton densities, respectively, to calculate the energy corrections to jets and the correction factors to the measured distributions.

The changes in $d\sigma/dE_T^{jet}$ and $d\sigma/d\eta^{jet}$ with respect to the *reference* values are taken as the contributions to the systematic uncertainty in each bin; they are added in quadrature to obtain the final systematic uncertainty. The bin-by-bin changes are summarized in table M.1 for $d\sigma/dE_T^{jet}$ and in table M.2 for $d\sigma/d\eta^{jet}$ and are presented graphically in figures M.1 and M.2.

The following items were changed:

– Monte Carlo generator:

We used the HERWIG generator including resolved+direct processes to correct the data. This change involves the use of the 'map' of transverse energy corrections to the jets obtained with HERWIG and the correction factors for the inclusive jet distributions determined with the HERWIG samples. This variation accounts for the uncertainties inherent to the fragmentation scheme used to model the hadronization process. The average variation of the cross section is 5.8% for $d\sigma/d\eta^{jet}$ and 7.3% for $d\sigma/dE_T^{jet}$.

– Parametrizations of the parton densities in the proton and photon:

The inclusive jet cross sections $d\sigma/d\eta^{jet}$ and $d\sigma/dE_T^{jet}$ depend both in shape and magnitude on the parton content of the photon and the proton. We have estimated the possible bias of the extracted results due to the particular choice of the parametrizations used in the Monte Carlo simulations. For this purpose we have chosen in each case (proton and photon) to vary the partonic density between the two most different parametrizations compatible with pre-HERA data. In the case of the photon we have compared GRV and LAC1, the latter having a larger amount of gluons in the photon at low-x_γ. The induced changes in the results are small: in average 3.0% for $d\sigma/d\eta^{jet}$ and 1.9% for $d\sigma/dE_T^{jet}$. The dependence of the results on the choice of the parametrization for the parton densities in the proton was found to be negligible. By varying the proton partonic densities between the two extreme assumptions MRSD0 (flat gluon

bin	1	2	3	4	5	6	7	8
	%	%	%	%	%	%	%	%
γSF(LAC1)	-2.0	-2.7	-2.5	-4.9	-1.1	0.3	-1.3	-0.3
pSF(MRSD0)	-0.2	-0.4	-0.1	0.1	0.3	-0.5	0.1	0.3
HERWIG	-3.1	-13.2	0.6	-6.8	-6.4	-6.0	-7.0	15.3
y_{JB}-scale -5%	-1.4	-2.2	-2.4	-4.1	-4.9	-6.3	-7.0	-4.6
$E^*_{TR} > 13$ GeV	-0.7	0.0	0.0	0.0	0.0	0.0	0.0	0.0
$p_z/E < 0.927$	2.5	4.0	6.6	7.0	7.2	7.5	10.5	12.5
resolved only	-0.6	-2.0	-1.8	-2.4	-2.6	-6.2	-4.2	-5.1
include POMPYT	-0.4	1.4	-0.3	0.8	0.4	1.7	0.1	0.0
total syst. error	4.8	14.4	7.7	11.9	11.2	13.2	15.1	20.9
E-scale +5%	-8.1	-17.3	-18.8	-20.2	-21.1	-22.9	-20.0	-23.7
E-scale -5%	12.2	23.6	25.4	26.0	23.5	32.5	28.9	50.5

Table M.1: Systematic errors on $d\sigma/dE_T$

content at low-x_p) and MRSD− (singular gluon content at low-x_p) the extracted cross sections $d\sigma/d\eta^{jet}$ ($d\sigma/dE_T^{jet}$) change in average by 0.2% (0.2%).

– Relative amount of resolved and direct processes:

For the *reference* values, Monte Carlo samples of resolved and direct processes were mixed according to the ratio given by the Monte Carlo cross sections. As it was noted in appendix J the description of the inclusive jet data distributions is bracketed by the expectations of the Monte Carlo with different physical assumptions. The uncertainty on the extracted results (and its stability) due to the particular choice of the relative amount of resolved and direct processes has been estimated considering alternatively the Monte Carlo simulation with resolved processes alone. The changes in the cross sections are small and, in average, amount to 2.5% (3.1%) for $d\sigma/d\eta^{jet}$ ($d\sigma/dE_T^{jet}$).

– Contribution from diffractive processes:

The generators PYTHIA and HERWIG simulate final states where colour flows between the partons steaming from the hard interaction and the spectator partons are always assumed: no contribution from diffractive processes to inclusive jet production is taken into account. We have searched for this type of contribution into our sample (see appendix L) and estimated the influence of its presence on the correction factors using Monte Carlo samples generated by POMPYT. The inclusion of a contribution from diffractive processes in addition to the non-diffractive ones has been simulated mixing the samples of PYTHIA and POMPYT according to the cross sections of these generators. The variation of the extracted cross sections resulting from this change is negligible: 0.5% for $d\sigma/d\eta^{jet}$ and 0.6% for $d\sigma/dE_T^{jet}$.

– Influence of the selection cuts:

A possible bias arises from the cuts in p_z/E, E^*_{TR} and y_{JB} used in the selection of the data sample. The distributions of the inclusive jet data sample in p_z/E and E^*_{TR} are reproduced by PYTHIA. The cut $p_z/E < 0.94$ was varied to $p_z/E < 0.927$ in the selection of the Monte Carlo sample. The change of the cross section $d\sigma/d\eta^{jet}$ is small (in average 2.7%) while for large E_T^{jet} the influence of this cut increases up to $\sim$ 10% (in average 7.2%). We varied the cut $E^*_{TR} > 12$ GeV to $E^*_{TR} > 13$ GeV in the data leaving the cut in the Monte Carlo unchanged. The change in the cross sections $d\sigma/d\eta^{jet}$ and $d\sigma/dE_T^{jet}$ is negligible: in average 0.6% for η^{jet} and 0.7% in

bin	1	2	3	4	5	6
	%	%	%	%	%	%
γSF(LAC1)	-4.8	-0.5	1.4	-0.6	0.2	-2.0
pSF(MRSD0)	-0.5	0.0	-0.2	0.1	-0.1	-0.2
HERWIG	2.5	4.8	2.6	0.9	-4.3	-6.4
y_{JB}-scale -5%	-12.9	-6.7	-4.4	-3.0	-2.3	-0.9
E^*_{TR} >13 GeV	-0.8	-0.9	-0.8	-1.2	-1.0	-0.4
$p_z/E < 0.927$	0.0	0.2	0.1	1.0	1.4	3.1
resolved only	-5.8	-5.8	-6.5	-2.2	-3.8	-4.3
include POMPYT	0.5	-0.9	-0.2	-0.1	-1.0	-0.2
total syst. error	15.2	10.2	8.5	4.2	6.5	8.6
E-scale +5%	-15.2	-15.3	-11.6	-11.3	-12.3	-10.6
E-scale -5%	27.3	19.3	19.6	14.6	15.3	11.9

bin	7	8	9	10	11	12
	%	%	%	%	%	%
γSF(LAC1)	-3.1	-4.3	-4.5	-5.8	-4.9	-3.5
pSF(MRSD0)	0.2	-0.1	-0.1	0.0	-0.4	-0.4
HERWIG	-4.1	-10.6	-6.3	-7.9	-15.8	-3.4
y_{JB}-scale -5%	-0.2	0.4	-0.5	-0.5	-0.9	0.2
E^*_{TR} >13 GeV	-0.4	-0.8	-0.5	-0.1	-0.4	-0.3
$p_z/E < 0.927$	4.3	4.1	4.4	4.3	4.0	5.5
resolved only	-0.2	0.3	0.1	0.4	0.5	-0.2
include POMPYT	0.1	-0.2	-0.7	-0.3	-0.7	0.6
total syst. error	6.7	12.3	8.9	10.7	17.1	7.4
E-scale +5%	-11.1	-9.3	-9.7	-9.5	-9.9	-10.7
E-scale -5%	14.5	14.7	14.0	14.7	14.8	14.5

Table M.2: Systematic errors on $d\sigma/d\eta$

the first bin for the E_T^{jet} (there is no effect in the remaining bins).

In appendix H we discussed the uncertainty in the simulation of the reconstruction of y with the Jacquet-Blondel method by using the subsample of tagged events. According to this study, we have changed the value of y_{JB} in the Monte Carlo by -5%: from y_{JB} to $y'_{JB} = 0.95 \cdot y_{JB}$. The average change in the cross section $d\sigma/d\eta^{jet}$ ($d\sigma/dE_T^{jet}$) is 2.7% (4.1%).

– Uncertainty in the E_T^{jet} scale:

In appendix H it was shown that the possible defficiencies in the simulation of the calorimeter response can lead to differences in the transverse energy of the jets in the selected kinematic region of at most 5%. We have taken into account this uncertainty repeating the analysis with the transverse energy scale of the *cal* jets in the Monte Carlo varied by $\pm$ 5%. These changes constitute the main uncertainty of the measurements: in average 14% (23%) for $d\sigma/d\eta^{jet}$ ($d\sigma/dE_T^{jet}$).

The dominant source of systematic error is the uncertainty in the absolute energy scale of the *cal* jets. The systematic uncertainties not associated with the energy scale of the jets have been added in quadrature and together with the statistical errors are shown as the thin error bars in figures 7.2 to 7.4. The uncertainty due to the energy scale of the jets is shown as a shaded band. We note that the systematic uncertainties have a large degree of correlation from bin to bin. These systematic uncertainties are to be understood as the maximum possible error associated to each data point. In addition, there is an overall normalization uncertainty of 3.3% from the luminosity determination, which has not been included.

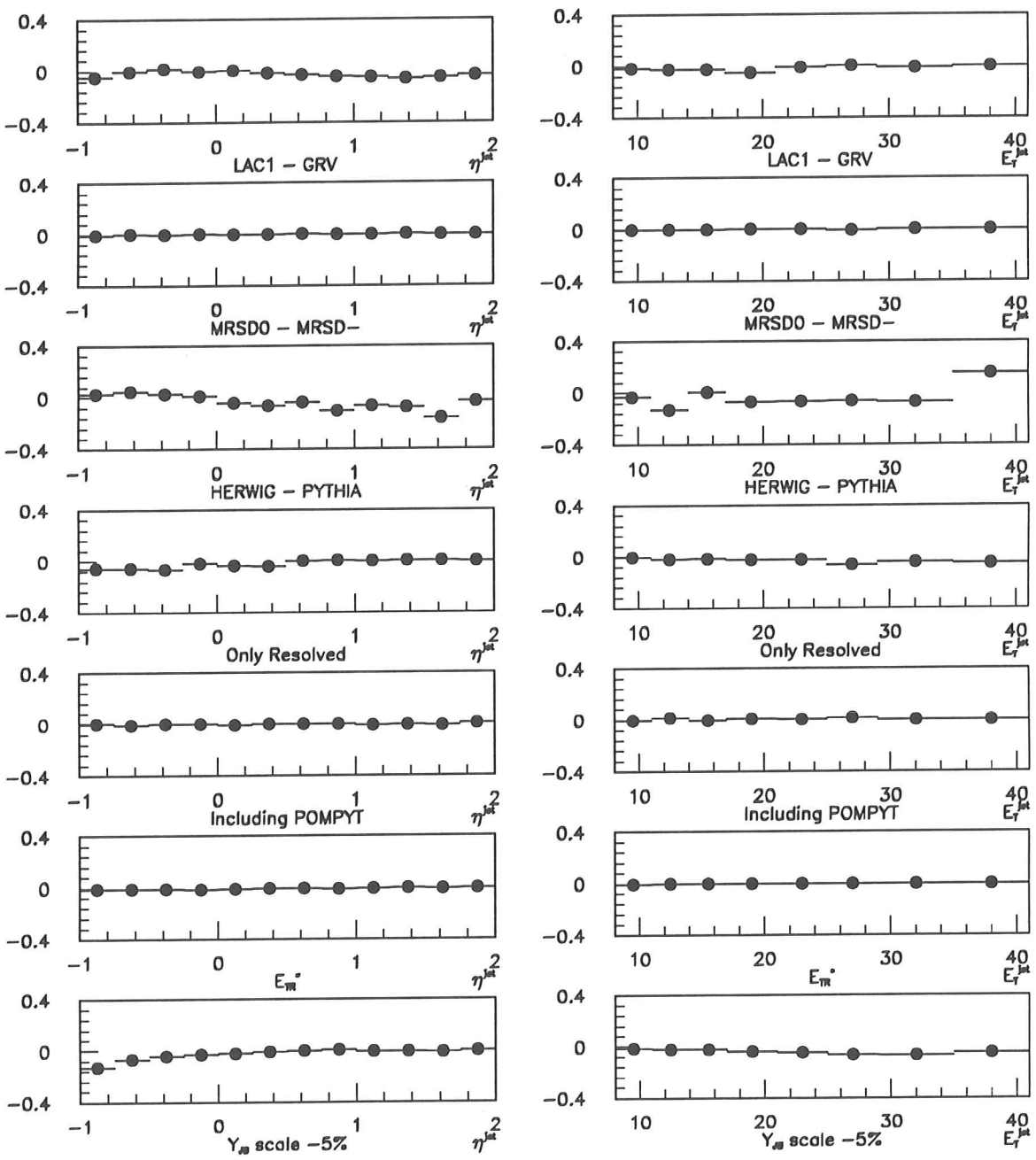

Figure M.1: Systematic errors (part 1)

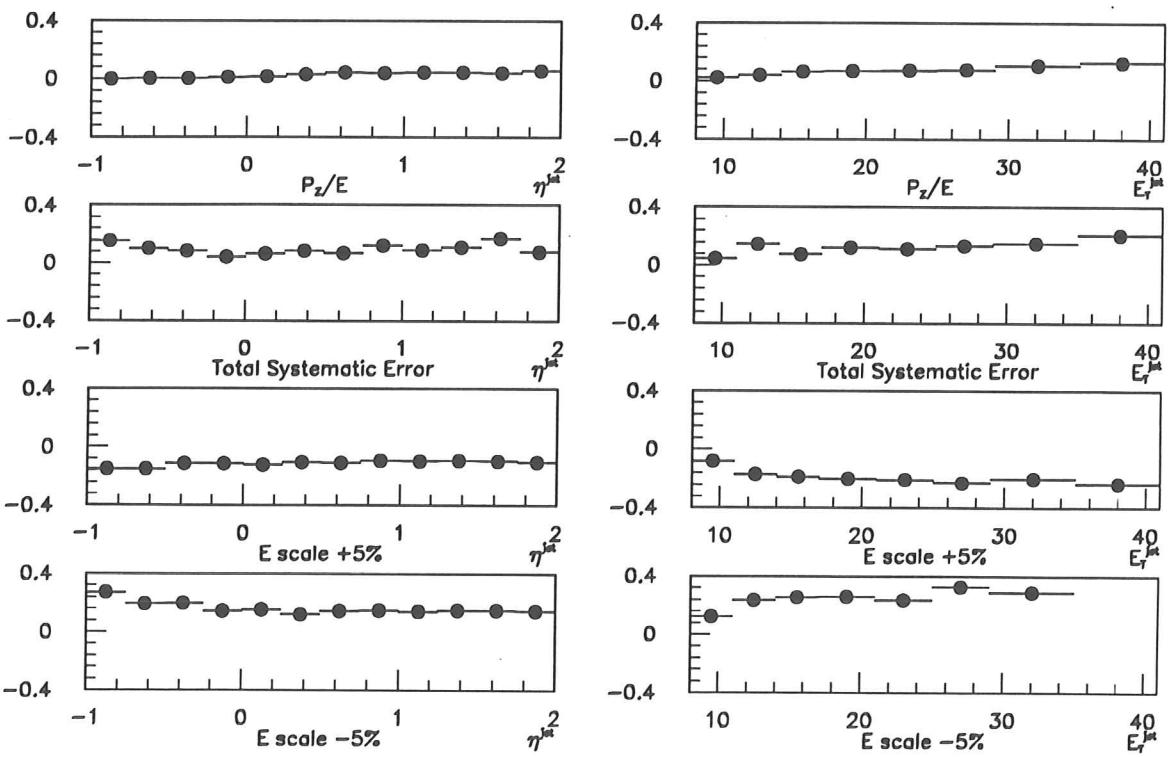

Figure M.2: Systematic errors (part 2)